July 2017

Nanoporous Solid Acid Materials for Biomass Conversion into Value-Added Chemicals: Synthesis, Catalysis, and Chemistry

Hong Je Cho

NANOPOROUS SOLID ACID MATERIALS FOR BIOMASS CONVERSION INTO VALUE-ADDED CHEMICALS: SYNTHESIS, CATALYSIS, AND CHEMISTRY

A Dissertation Presented

by

HONG JE CHO

Submitted to the Graduate School of the
University of Massachusetts Amherst in partial fulfillment
of the requirements for the degree of

DOCTOR OF PHILOSOPHY

May 2017

Chemical Engineering

NANOPOROUS SOLID ACID MATERIALS FOR BIOMASS CONVERSION INTO VALUE-ADDED CHEMICALS: SYNTHESIS, CATALYSIS, AND CHEMISTRY

A Dissertation Presented

by

HONG JE CHO

Approve as to style and content by:

_____
Wei Fan, Chair

_____
Friederike Jentoft, Member

_____
Ashwin Ramasubramaniam, Member

_____
John Klier, Department Head
Department of Chemical Engineering

ACKNOWLEDGEMENTS

This work was supported by Catalysis Center for Energy Innovation (funded by the US Dept. of Energy, DE-SC0001004) and UMass (start-up fund). I would like to acknowledge my advisor, Prof. Wei Fan, who gives me a great opportunity to work on these interesting projects and enthusiastically advises me in research with countless conversations. I am grateful to his exceptional guidance, support and patience throughout my Ph.D. I express my gratitude to Prof. Friederike Jentoft and Ashwin Ramasubramaniam as my committee members. Their questions and suggestions enriched my thesis to a great extent. I would like to thank Prof. Michael Tsapatsis, Prof. Paul Dauenhauer and Dr. Limin Ren at University of Minnesota, Prof. Raul Lobo, Prof. Binjun Xu and Nick Gould at University of Delaware, Prof. Ray Gorte and Yu-Hao Yeo at University of Pennsylvania in the *p*-xylene project.

I am in great debt to Zhuopeng, Chun-Chih and Paul. They helped me a lot with basic experimental skills when I was first year. I am thankful to my current lab members, Vivek, Xiaoduo and Sanket. I always enjoyed great discussions and fun conversations with you. I want to thank Prof. Jessica Schiffman and Katrina for our fruitful collaboration in the zeolite-nanofiber project. I express my appreciation to the chemical engineering staffs, Joe, Gary, Anshalee and Marie, who helped me with safety training and general problems. I am grateful to have great undergrads who worked with me, Nick, Kyle and Tam. I would like to acknowledge Alex and Lou in Microscopy center, Sekar in X-ray labs and Weiguo in NMR center for their instrument training and

management. I want to thank ChEGS community for providing me with social and academic environments including party, recruit weekend, softball and ping-pong game.

Many sincere thanks go to my mother and younger brother for showing me their trust, love and support. I want to express my boundless gratitude to my wife, Surl Hee, who has been a constant source of love and support throughout everything. I also thank my baby, Ahron, for giving me plenty of happiness. I welcome my newborn baby, Einne, into this world. Lastly, but above all, I would like to thank my Lord, Jesus Christ, for always guiding me, strengthening me and loving me behind all my works and accomplishments.

ABSTRACT

NANOPOROUS SOLID ACID MATERIALS FOR BIOMASS CONVERSION INTO VALUE-ADDED CHEMICALS: SYNTHESIS, CATALYSIS, AND CHEMISTRY

MAY 2017

HONG JE CHO, B.E., AJOU UNIVERSITY

M.S., SEOUL NATIONAL UNIVERSITY

Ph.D., UNIVERSITY OF MASSACHUSETTS AMHERST

Directed by: Professor Wei Fan

Growing environmental concerns associated with diminishing reserves of fossil fuels has led to accelerated research efforts towards the discovery of new catalytic processes for converting renewable lignocellulosic biomass into value-added chemicals. For this conversion, nanoporous solid acid materials have been widely used because of their excellent hydrothermal stability and molecular sieving capability.

In the thesis, hierarchical Lewis acid zeolites with ordered mesoporosity and MFI topology (three dimensionally ordered mesoporous imprinted (3DOm-i) Sn-MFI) were successfully synthesized within the confined space of three dimensionally ordered mesoporous (3DOm) carbon by a seeded growth method. The obtained 3DOm-i Sn-MFI showed at least 3 times higher catalytic activities for the biomass-derived sugar isomerization than conventional Sn-MFI zeolites. This is because the mesopores in the hierarchical zeolites greatly enhance molecular transport.

In addition, Lewis acid Sn-MFI combined with Pt metal nanoparticles (Pt/Sn-MFI) could oxidize glycerol to produce lactic acid (LA) under base-free conditions. Glycerol is

a by-product in biodiesel synthesis. 80.5% selectivity of LA was achieved at 89.8% conversion of glycerol using a bifunctional Pt/Sn-MFI catalyst under base-free conditions. In the tandem reaction pathway, selective oxidation of glycerol to glyceraldehyde (GLA) and dihydroxyacetone (DHA) by using Pt catalysts was cascaded with Lewis acid catalyzed isomerization of GLA/DHA into LA.

Moreover, morphology-tunable Lewis acid Sn-BEA with hydrophobicity was successfully synthesized by recrystallization of post-synthesized Sn-BEA (Sn-BEA-PS) using ammonium fluoride (NH_4F) and tetraethylammonium bromide (TEABr). This recrystallization includes simultaneous procedures of dissolution-reassembly: i) the dissolution of Si-O bonds around silanol nests by fluoride ions, and ii) the reassembly of fragmented silica species into defect-free zeolite framework in the presence of TEA ions. The recrystallization also increased open Lewis acid Sn sites. These findings can explain why a 2.5 times higher rate of aqueous glucose isomerization was achieved on recrystallized Sn-BEA (Sn-BEA-RC), compared with Sn-BEA-PS. Moreover, in the isomerization of bulky lactose (C_{12} sugar) dissolved in MeOH, hierarchical Sn-BEA-RC showed a 3.2-fold higher activity than hydrothermally synthesized Sn-BEA (Sn-BEA-HF), due to the mesopores and enhanced organophobic character of the recrystallized catalyst.

In the final part, renewable *p*-xylene synthesis was investigated. *p*-Xylene is a major commodity chemical used for the production of polyethylene terephthalate (PET) with applications in polyester fibers, films and bottles. Diels-Alder cycloaddition of 2,5-dimethylfuran (DMF) and ethylene with subsequent dehydration of the cycloadduct

intermediate to produce *p*-xylene is an attractive reaction pathway for its production from biomass feedstocks. It was shown that phosphorous-containing zeolite BEA (P-BEA) is active, stable and selective for this reaction with an unprecedented *p*-xylene yield of 97%. It can selectively catalyze the dehydration reaction from the furan-ethylene cycloadduct to *p*-xylene, without performing side reactions which include alkylation and oligomerization. This acid catalyst establishes a commercially attractive process for renewable *p*-xylene production.

TABLE OF CONTENTS

Page

ACKNOWLEDGEMENTS iv

ABSTRACT vi

LIST OF TABLES xii

LIST OF FIGURES xiii

LIST OF SCHEMES xvii

CHAPTER

1. INTRODUCTION 1

    1.1 Lignocellulosic Biomass Conversion into Valuable Compounds 1

    1.2 Thesis Scope 4

2. HIERARCHICAL LEWIS ACID SN-MFI FOR CELLULOSIC SUGAR ISOMERIZATIONS 6

    2.1 Introduction 6

    2.2 Experimental 8

        2.2.1 Catalyst Preparation 8

        2.2.2 Catalyst Characterization 10

        2.2.3 Catalytic Reaction 11

        2.2.4 Sample Analysis 12

    2.3 Results and Discussions 13

3. BIFUCTIONAL PT/SN-MFI CATALYSTS FOR ONE-POT CONVERSION OF GLYCEROL TO LACTIC ACID UNDER BASE-FREE ENVIRONMENTS 31

    3.1 Introduction 31

    3.2 Experimental 34

3.2.1 Catalyst Preparation 34

3.2.2 Catalyst Characterization 36

3.2.3 Catalytic Test 37

3.2.4 Sample Analysis 38

3.3 Results and Discussions 39

4. MORPHOLOGY-TUNABLE LEWIS ACID SN-BEA WITH HYDROPHOBICITY FOR CELLULOSIC SUGAR ISOMERIZATIONS 51

4.1 Introduction 51

4.2 Experimental 54

4.2.1 Material Syntheses 54

4.2.2 Material Characterization 56

4.2.3 Catalytic Activity Test 58

4.3 Results and Discussions 59

5. PHOSPHORUS-CONTAINING ZEOLITES FOR RENWABLE P-XYLENE PRODUCTION 77

5.1 Introduction 77

5.2 Experimental 79

5.2.1 Material Synthesis 79

5.2.2 Material Characterization 82

5.2.3 Catalyst Testing for Diels-Alder Cycloaddition and Subsequent Dehydration of 2,5-Dimethylfuran (DMF) with Ethylene 85

5.2.4 Catalyst Removal Test of P-BEA and P-SPP 86

5.2.5 Catalyst Reusability of P-BEA and P-SPP 86

5.3 Results and Discussions 86

6. CONCLUSIONS 105

7. SUGGESTED FUTURE DIRECTIONS 108

BIBLIOGRAPHY 111

LIST OF TABLES

Table Page

2.1. Textural Information of the Sn-MFI samples from N_2 adsorption-desorption isotherms and composition information 18

2.2. Summary of TOF for three Lewis acid catalyzed reactions 26

3.1. Pt metal surface area and crystallite diameter for each catalyst determined by H_2 chemisorption 41

3.2. Oxidation of glycerol and other substrates on the catalysts synthesized in the study 42

3.3. Textural information from N_2 adsorption-desorption isotherms 45

3.4. TOF values for the conversion of PA into LA 46

4.1. Peak ratio on XRD patterns of Com_RC synthesized with different recrystallization times 68

4.2. TEA molecules occluded within as-made Com_RC during the recrystallization 68

5.1. ICP analysis and textural properties of the sample 89

5.2. Comparison of catalytic activites for DMF reaction with ethylene in this study ... 100

LIST OF FIGURES

Figure Page

2.1. SEM images of (a) 3DOm-i Sn-MFI, (b) Sn-MFI_N, and (c) Sn-MFI_L 13

2.2. FT-IR spectra of 3DOm-i Sn-MFI, Sn-MFI_N, and Sn-MFI_L after adsorbing (a) deuterated acetonitrile (CD_3CN) and (b) pyridine 15

2.3. Diffuse reflectance UV-Vis (DR-UV) spectra of the Sn-MFI catalysts 15

2.4. (a) XRD and (b) SAXS patterns of 3DOm-i Sn-MFI, Sn-MFI_N, and Sn-MFI_L samples 16

2.5. (a) Argon adsorption-desorption isotherms and (b) pore size distributions using NLDFT for 3DOm-i Sn-MFI, Sn-MFI_N, and Sn-MFI_L samples 18

2.6. Reaction profiles for (a) the conversion of DHA to ML and (b) ML yield on different Sn-MFI catalysts 20

2.7. Initial catalytic activities of Sn-MFI catalysts for the conversions of DHA and PA in the presence of MeOH 21

2.8. FT-IR spectra in the OH-stretch region (3800 - 3000 cm^{-1}) of the Sn-MFI catalysts 22

2.9. Plots of initial reaction rates against relative number of Brønsted acid sites for the conversion of DHA into ML 22

2.10. Product distributions for the conversion of DHA into ML over Sn-MFI catalysts ... 24

2.11. Initial catalytic activities of Sn-MFI catalysts for isomerizations of xylose and glucose 26

2.12. Reaction profiles for (a) the conversion of PA to ML and (b) ML yield using different Sn-MFI catalysts 28

2.13. Plots of -ln(1-x) against a reaction time where x is the product yield for the conversion of PA into ML over Sn-MFI catalysts 28

2.14. Cumulative pore volumes (a) and pore size distributions (b) using NLDFT of hierarchical Sn-MFI zeolites made with BP2000 and Norit SX Ultra, respectively, derived from N_2 adsorption-desorption isotherms 30

2.15. A SEM image of hierarchical Sn-MFI made with BP2000 30

3.1. XRD patterns of the prepared catalysts: (a) Pt/Sn-MFI, Sn-MFI, Pt/silicalite-1 and silicalite-1, and (b) Pt/Sn-BEA, Sn-BEA, Pt/TiO_2, TiO_2 and Pt/activated carbon (AC)..... 39

3.2. (a) A TEM image and (b) Pt particle size distribution estimated from TEM images for the Pt/Sn-MFI catalyst..... 40

3.3. (a) Concentration profiles and (b) glycerol conversion and LA selectivity over Pt/Sn-MFI 43

3.4. Reaction profiles for (a) the conversion of PA into LA and (b) LA yield over Pt/Sn-MFI, Sn-MFI, Pt/Sn-BEA and Sn-BEA catalysts..... 46

3.5. FT-IR spectra in the OH-stretch region (3800 - 3000 cm^{-1}) of Sn-MFI and Sn-BEA zeolites 46

3.6. (a) Concentration profile and (b) glycerol conversion and LA selectivity over a physical mixture of Pt/AC and Sn-MFI..... 48

3.7. Recycling of Pt/Sn-MFI catalyst after 24 h of reaction 50

4.1. (a) A SEM image of Sn-BEA-HF, and (b) XRD patterns of Sn-BEA-HF and SnO_2 59

4.2. SEM images of (a) Com_Al-BEA, (b) Com_PS, (c) Com_RC, (d) 200nm_Al-BEA, (e) 200nm_PS, (f) 200nm_RC, (g) 3DOm_Al-BEA, (h) 3DOm_PS, and (i) 3DOm_RC 60

4.3. XRD patterns of (a) Com_Al-BEA, Com_PS and Com_RC, (b) 200nm_Al-BEA, 200nm_PS and 200nm_RC, and (c) 3DOm_Al-BEA, 3DOm_PS and 3DOm_RC..... 62

4.4. FT-IR spectra of Sn-BEA-RC, Sn-BEA-PS and Sn-BEA-HF catalysts using (a) deuterated acetonitrile (CD_3CN) and (b) pyridine as a probe molecule 64

4.5. FT-IR spectra in the OH-stretch region (3800 − 3000 cm^{-1}) of the Sn-BEA catalysts 67

4.6. XRD patterns of Com_RC synthesized with different recrystallization times (1 day to 7 days) and Com_RC synthesized without TEABr..... 67

4.7. TGA curves of as-made Com_RC synthesized with different recrystallization times (1 day to 7 days)..... 68

4.8. Initial catalytic activities of Sn-BEA-HF, Sn-BEA-PS and Sn-BEA-RC for isomerization of aqueous glucose 70

4.9. Initial catalytic activities of Com_RC with different recrystallization times (1 day to 7 days) for isomerization of aqueous glucose 70

4.10. (a) Water vapor adsorption isotherms at 25 °C and (b) thermogravimetric analysis (TGA) of water adsorption on Sn-BEA-HF, Com_PS and Com_RC zeolites..... 72

4.11. Initial catalytic activities of Sn-BEA-HF, Sn-BEA-PS and Sn-BEA-RC for glucose isomerization in MeOH 74

4.12. Thermogravimetric analysis (TGA) of MeOH adsorption on Sn-BEA-HF, Com_PS and Com_RC zeolites 74

4.13. Initial catalytic activities of Sn-BEA-HF, Sn-BEA-PS and Sn-BEA-RC for lactose isomerization in (a) water and (b) MeOH solvents, respectively 76

5.1. XRD patterns of Al-BEA (Zeolyst, CP814E, Si/Al = 12.5), P-BEA, P-SPP and P-Celite 87

5.2. SEM images of (a) Al-BEA (Zeolyst, CP814E, Si/Al = 12.5) and (b) P-BEA, and TEM images of (c) P-SPP and (d) P-BEA 88

5.3. Argon adsorption-desorption isotherms for (a) P-BEA, dealuminated BEA and Al-BEA and (b) P-Celite, Celite and P-SPP..... 88

5.4. Catalytic performance of various catalysts for the *p*-xylene production from the reaction of DMF with ethylene: (a) overall product distributions, (b) yield of alkylated by-products, (c) carbon balance versus DMF conversion and (d) yield of *p*-xylene versus reaction time..... 90

5.5. Catalytic activities for the DMF reaction with ethylene over P-SPP made using TBPOH, Si-SPP made using TBAOH, pure siliceous BEA and no catalyst: (a) DMF conversion and (b) *p*-xylene yield..... 92

5.6. Catalytic performances of P-Al-BEA for the production of *p*-xylene: (a) DMF conversion and (b) *p*-xylene yield..... 92

5.7. Catalytic activities for the *p*-xylene production from the reaction of DMF with ethylene: (a) DMF conversion and (b-e) overall product distributions..... 94

5.8. Heterogeneous nature of the DMF reaction with ethylene over P-BEA and P-SPP (a-d) 96

5.9. Catalyst reusability of P-containing catalysts: (a,b) DMF conversion and *p*-xylene yield over P-BEA and P-SPP during catalyst recycling and (c) *p*-xylene selectivity over P-BEA and P-SPP during catalyst recycling 97

5.10. SEM images (a-b) and XRD patterns (c) of fresh P-BEA and spent P-BEA after 3rd recycling test 98

5.11. ^{31}P solid state MAS NMR spectra of P-BEA, P-SPP and P-Celite 99

5.12. TPD-TGA of 2-propanamine on (a) P-BEA, (b) P-SPP and (c) P-Celite..... 102

5.13. Pyridine FT-IR spectra of (a) P-BEA and (b) Al-BEA under dehydrated condition and (c) P-BEA under hydrated condition 103

5.14. TPD-TGA of 2,5-hexanedione on P-BEA 104

LIST OF SCHEMES

Scheme Page

1.1. Representative Lewis acid zeolites: the structures of (a) Sn-MFI and (b) Sn-BEA..... 2

1.2. The conversion of lignocellulosic biomass into value-added chemicals 4

2.1. Synthesis procedure of hierarchical Sn-MFI (3DOm-i Sn-MFI) 9

2.2. Reaction pathway for the conversion of dihydroxyacetone (DHA) or glyceraldehyde (GLA) in Methanol (MeOH) into either methyl lactate (ML) or pyruvaldehyde dimethylacetal (PADA)..... 19

2.3. Reaction pathway for the Lewis acid catalyzed isomerization of (a) xylose or (b) glucose, respectively..... 24

3.1. General reaction pathways of glycerol oxidation..... 32

3.2. Proposed reaction pathways for the selective oxidation of glycerol to LA over the Pt/Sn-MFI catalyst..... 49

4.1. Proposed mechanism of a Sn-BEA recrystallization process..... 66

4.2. Reaction scheme for the Lewis acid catalyzed isomerization of lactose into lactulose 76

5.1. Production of renewable *p*-xylene..... 79

CHAPTER 1

INTRODUCTION

1.1 Lignocellulosic Biomass Conversion into Valuable Compounds

Increasing demand for energy and commodity chemicals has led to accelerated research efforts towards the discovery of new catalytic pathways for converting renewable resource into value-added chemicals and fuels. Lignocellulosic biomass has been considered an ideal alternative to fossil resources, since biomass is the only sustainable source of organic molecules. The processing of lignocellulosic biomass, an inexpensive and abundant source of carbon, provides the promise of sustainable chemicals and carbon-neutral liquid transportation fuels.[1-3] Many efforts have been devoted to the research of the conversion of lignocellulosic biomass into transportation fuels and value-added chemicals using nanoporous materials classified as microporous (< 2 nm), mesoporous (2-50 nm) and macroporous (> 50 nm) materials.[4, 5] In particular, crystalline microporous zeolites have attracted significant attention because of their excellent hydrothermal stability, molecular sieving capability and acidity for various catalytic reactions in petrochemical and biomass processing.[6,7] The acid property of the zeolites is associated with charge compensation with H^+. Typically, zeolites composed of $[SiO_4]$ and $[AlO_4]^-$ tetrahedra are neutralized by cations, in order to maintain electro-neutrality. The use of H^+ renders the zeolite Brønsted-acidic. In other words, the protons (H^+) of bridging Si-OH-Al groups act as Brønsted acid sites on the zeolites. Recently, Lewis acid zeolites play an essential role for selectively activating functional groups of

the organic molecules involved in biomass conversion. By replacing Al atoms in aluminosilicate zeolites by other tetravalent metals (i.e. Sn^{4+}, Zr^{4+}, Ti^{4+}, etc.), zeolites do not require additional cations and can possess Lewis acidity. For instance, transition metals such as Zr and Ti with incomplete *d*-block subshells are Lewis acid sites in zeolite frameworks able to accept an electron pair.[8] In the case of a *p*-block Sn element, Lewis acidity of Sn sites in zeolites can come from the involvement of the unoccupied low-lying *d* orbitals.[8] It should be noted that aluminosilicate zeolites can also have Lewis acidity arising from the tri-coordinated Al sites on the framework and the extraframework Al and the charge-compensating cations except H^+.[9] Scheme 1.1 illustrates the structures of Lewis acid Sn-MFI and Sn-BEA zeolites. Both materials composed of [SiO_4] and [SnO_4] tetrahedra have MFI topology with 10-membered ring (~0.56 nm of pore size) and BEA one with 12-membered ring (~0.74 nm of pore size), respectively.

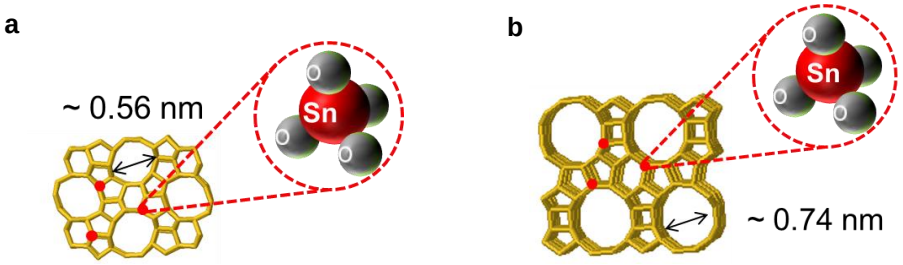

Scheme 1.1 Representative Lewis acid zeolites: the structures of (a) Sn-MFI and (b) Sn-BEA.

Scheme 1.2 illustrates the conversion of lignocellulosic biomass into useful organic compounds to replace the existing chemicals related to crude oils.

Lignocellulosic biomass consists of three major components: 40-50% cellulose and 25-35% hemicellulose formed by polymerization of glucose and that xylose, respectively, and 15-20% lignin formed with phenols and phenolic molecules. Among the three components, hemicellulose and cellulose are depolymerized to xylose (C_5 pentose sugar) and glucose (C_6 hexose sugar), respectively.[4, 10] Xylose is further isomerized over Lewis acid catalysts to xylulose, which further undergoes retro-aldol condensation to form glycoaldehyde and dihydroxyacetone (DHA, C_3 triose sugar).[11] In the same manner, Lewis acid catalysts such as Sn-BEA zeolites perform glucose isomerization to fructose, [12] which is further converted into glyceraldehyde (GLA, C_3 triose sugar) and DHA via retro-aldol condensation.[1] These C_3 sugars can be obtained from oxidation of glycerol using metal catalysts.[13-15] Glycerol, a by-product generated by biodiesel synthesis, can serve as one of the major renewable building blocks.[16, 17] DHA and GLA sugars become lactic acid and methyl lactate in water and methanol (MeOH) solvents, respectively, which is catalyzed by Lewis acid materials. Fructose is dehydrated to form hydroxymethylfurfural (HMF),[18] hydrodeoxygenation of which produces 2,5-dimethylfuran (DMF).[19, 20] These steps have been demonstrated individually at high efficiency with the highest selectivity to HMF of 80% and DMF of 98%.[18-20] Brønsted acid or Lewis acid zeolites are capable of converting DMF into *p*-xylene via Diels-Alder cycloaddition and subsequent dehydration reactions.[21-23]

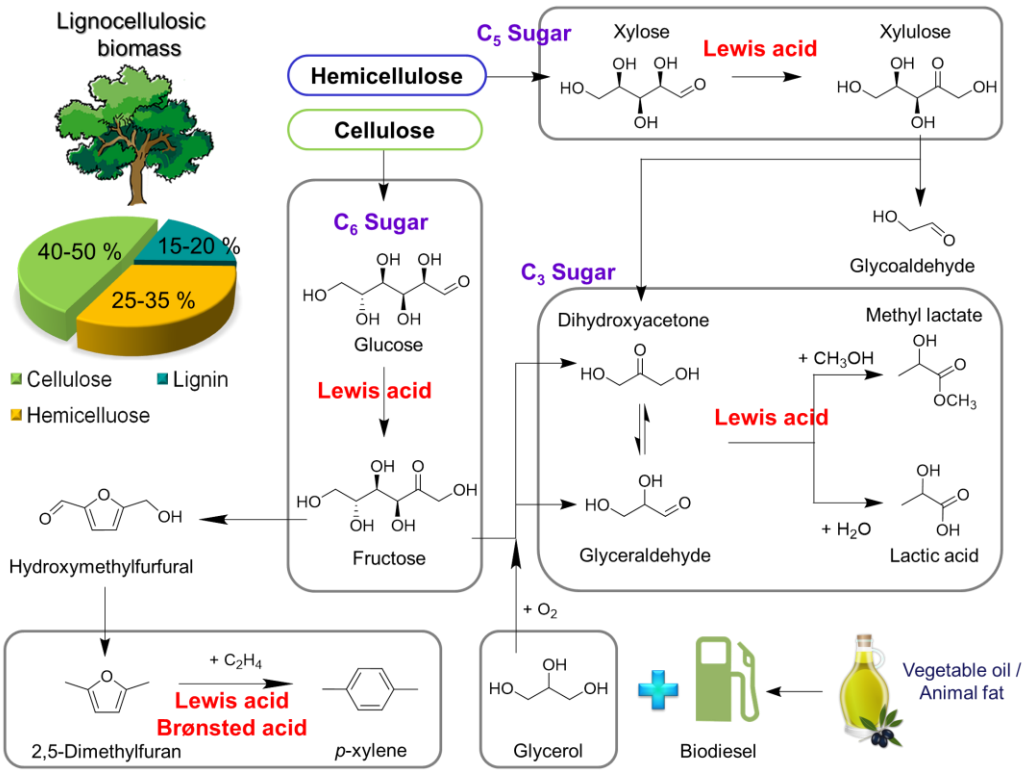

Scheme 1.2 The conversion of lignocellulosic biomass into value-added chemicals.

1.2 Thesis Scope

The thesis is constructed as follows. Hierarchical Lewis acid Sn-MFI zeolites were synthesized and have shown high reactivity for cellulosic sugar isomerizations, which is described in Chapter 2. In Chapter 3, the Lewis acid Sn-MFI combined with Pt nanoparticles exhibited high selectivity to lactic acid from glycerol oxidation under base-free environment. Chapter 4 deals with the synthesis of morphology-tunable Lewis acid Sn-BEA having enhanced hydrophobicity for sugar isomerization reactions. In Chapter 5, Brønsted acidic phosphorous-containing BEA zeolites as a new class of materials, P-BEA, were investigated for *p*-xylene synthesis via the Diels-Alder reaction and dehydration of DMF with ethylene, and showed 97% yields of *p*-xylene. Chapter 6 gives conclusions for

the accomplished works, and suggested future directions for the researches are included in Chapter 7.

CHAPTER 2

HIERARCHICAL LEWIS ACID SN-MFI FOR CELLULOSIC SUGAR ISOMERIZATIONS

2.1 Introduction

The catalytic performance of zeolite catalysts can be hampered by slow diffusion of reactants and products in their microporous structures, in particular, when bulky molecules are involved. Hierarchical zeolites with mesoscale porosity superimposed on crystalline microporous structures offer a new class of porous materials allowing molecular sieving capability as well as fast mass transport.[24-27] Fast transport of molecules in hierarchical zeolites could facilitate molecules to access the active sites located within micropores and reduce the residence time of molecules in catalysts, providing enhanced reaction rates and slower catalyst deactivation.[26-28] Several strategies have been developed so far for the synthesis of hierarchical zeolites with mesopores, including dealumination and desilication of aluminosilicate zeolites, exfoliation and pillaring of layered zeolites, a supramolecular templating method, and a hard templating method.[29-33] Despite a number of hierarchical zeolites synthesized by these methods, it is still a grand challenge to precisely control framework compositions and the size and shape of the formed mesopores. Recently, we reported that hierarchical zeolites with highly ordered mesoporous structures can be obtained by confining zeolite growth within three dimensionally ordered mesoporous (3DOm) carbon under hydrothermal conditions.[34] With the combination of seeded growth and a confined synthesis, hierarchical aluminosilicate zeolites with tunable mesopores and

compositions were synthesized using the recipes for conventional hydrothermal synthesis of zeolites.[35] The prepared hierarchical zeolites displayed three dimensionally ordered mesoporous imprinted (3DOm-i) structure. The precisely controllable mesoporosity in 3DOm-i zeolites allows for the fundamental understanding of the effects of mesopores on the catalytic performance of this new class of porous materials.[36, 37]

Recently, Lewis acid catalysts have emerged and play an essential role for selectively activating functional groups of the organic molecules including biomass-derived carbohydrates, as represented in Scheme 1.2. Sn-containing molecular sieves and mesoporous silica materials have shown promising Lewis activity for catalyzing the isomerization of cellulosic sugars (C_3, C_5 and C_6 sugars),[1, 38-40] the Meerwein−Ponndorf−Verley (MPV) reduction,[41-43] several oxidation reactions such as the Baeyer−Villiger oxidation and Meerwein−Ponndorf−Verley−Oppenauer oxidation,[43-46] and Diels-Alder reaction of 2,5-dimethylfuran (DMF) with ethylene to produce *p*-xylene which is used as a precursor of polyethylene terephthalate (PET).[22, 47] Specifically, a molecular sieve with MFI framework containing tetrahedrally coordinated Sn atoms (Scheme 1.1a), Sn-MFI, has been used for carbohydrate-related reactions, revealing a promising catalytic result for the conversion of DHA into lactic acid and alkyl lactates.[48-51] In contrast, Sn-containing mesoporous silica catalysts, such as Sn-SBA-15 and Sn-MCM-41, exhibited a low reactivity for these reactions, probably due to the different local environment of Sn and the amorphous nature of the silica wall.[51, 52] Thus, hierarchical Sn-containing zeolites consisting of active Lewis acid sites and tunable

mesoporosity have promising implications for activating bulky substrates involved in the conversion of lignocellulosic biomass and fine chemical synthesis because the mesoporosity can lead to faster molecular access to the catalytic active sites spread over the external and internal surface of the catalysts. However, hierarchical Sn-containing zeolites are more challenging to synthesize than their aluminosilicate analogues, mainly because of the discrepancy in the reactivity of Sn and Si sources and the larger atomic size of Sn (Sn−O, ~1.9 Å; Si−O, ~1.7 Å).

Herein, we demonstrated that hierarchical stannosilicate molecular sieves with MFI topology and three dimensionally ordered mesoporous imprinted (3DOm-i) structures were successfully synthesized. The obtained 3DOm-i Sn-MFI exhibited superior catalytic performances for cellulosic sugar isomerizations including DHA, xylose, and glucose in methanol. The combination of a seeded growth method with confined synthesis is a versatile and reliable approach for tailoring hierarchical Sn-MFI catalysts.

2.2 Experimental

2.2.1 Catalyst Preparation

A seeded growth method was applied for the confined synthesis of 3DOm-i Sn-MFI within a 3DOm carbon template. 3DOm carbon with a cage size of 35 nm was prepared according to a method reported in our previous literature.[53, 54] The particle size of 3DOm carbon was 2−5 μm. A clear synthesis solution with a composition of 1 SiO_2 : 0.008 SnO_2 : 0.43 TPAOH : 22.20 H_2O was prepared using a published recipe.[55] The synthesis procedure is displayed in Scheme 2.1. In a typical synthesis, 0.07 g of tin (IV)

chloride pentahydrate ($SnCl_4 \cdot 5H_2O$, Alfa Aesar) was first mixed with 5.50 g of tetrapropylammonium hydroxide (40% TPAOH, Alfa Aesar) under stirring. Thereafter, 5.20 g of tetraethylorthosilicate (TEOS, 98%, Alfa Aesar) was added into this mixture, followed by stirring for 30 min at room temperature. An additional 6.33 g of deionized water was added into the solution to reach the final composition. A transparent homogeneous solution was achieved after stirring for 24 h at room temperature. For the confined synthesis of Sn-MFI in the 3DOm carbon, 0.20 g of 3DOm carbon and 15 mL of the synthesis solution were mixed in a Teflon-lined autoclave and heated in an oven at 170 °C for 24 h to form Sn-MFI seeds. The solid product was recovered by filtration, followed by extensively washing with deionized water before mixing into a freshly prepared synthesis solution for the second cycle of the seeded growth. The seeded growth process was repeated three times. Finally, the as-made product was washed thoroughly by filtration with about 2 L of deionized water and dried in a convection oven at 100 °C overnight. The 3DOm carbon and the structure-directing agent (TPAOH) were removed from the product by calcination at 600 °C for 24 h in air.

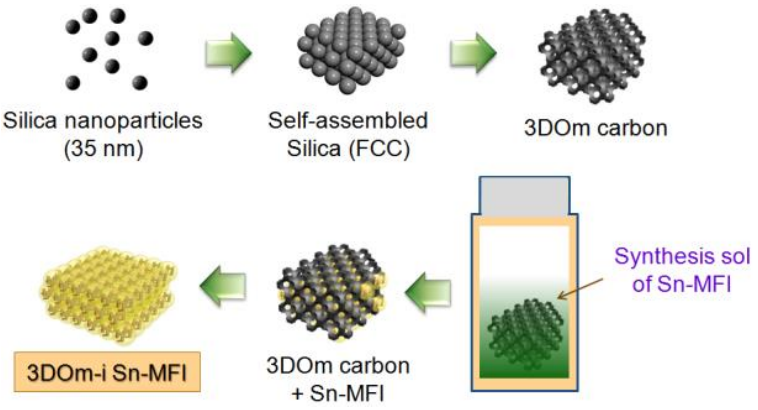

Scheme 2.1 Synthesis procedure of hierarchical Sn-MFI (3DOm-i Sn-MFI).

For comparison, two more conventional Sn-MFI zeolites were prepared. Sn-MFI with a particle size of 300 nm, Sn-MFI_N, was prepared using the same synthesis solution as 3DOm-i Sn-MFI. Crystallization was performed at 170 °C for 2 days. Large Sn-MFI with a particle size of 10 μm, Sn-MFI_L, was synthesized by following published methods.[51, 55] A 0.125 g portion of $SnCl_4 \cdot 5H_2O$ was premixed with 5.00 g of deionized water and slowly added to an ammonium fluoride (NH_4F, Alfa Aesar) aqueous solution made by dissolving 2.68 g of NH_4F in 12.50 g of deionized water. Subsequently, 4.90 g of tetrapropylammonium bromide (TPABr, Sigma-Aldrich) dissolved in 28.0 g of deionized water was added to this mixture. Finally, 4.3 g of fumed silica (Sigma-Aldrich) was added into this solution, and the mixture was stirred for 3 h at room temperature. The molar composition of the gel was 1 SiO_2 : 0.005 SnO_2 : 0.26 TPABr : 1 NH_4F : 35 H_2O. The crystallization was carried out at 200 °C for 7 days. The obtained Sn-MFI_L and Sn-MFI_N were washed with an excess amount of deionized water and dried at 100 °C overnight. Finally, the samples were calcined at 550 °C for 12 h in air.

2.2.2 Catalyst Characterization

Powder X-ray diffraction (XRD) patterns of the catalysts were recorded on an XRD diffractometer (X'Pert Pro, PANalytical) operated at an acceleration voltage of 45 kV and a current of 40 mA using Cu Kα radiation. The data were collected over a 2θ range of 4−40°. XRD patterns at low angle were collected on a pinhole small-angle X-ray scattering system (S-ax3000, Rigaku) using monochromatic Cu Kα radiation with a diameter of ~0.4 mm. The SAXS intensity was measured by a two-dimensional gas-filled

wire array detector at a distance of ~1.5 m from the sample. The morphology of the products was examined by a scanning electron microscope (SEM, Magellan 400, FEI). Prior to the SEM measurement, the samples were coated with platinum. Both nitrogen (at 77 K) and argon (at 87 K) adsorption−desorption isotherms were measured by using an automated gas sorption analyzer (Autosorb iQ2, Quantachrome) after the samples were degassed at 300 °C under vacuum. Elemental analysis was conducted by inductively coupled plasma optical emission spectroscopy (ICP-OES, iCap 6500 Dual view, Thermo Scientific). DRIFT-IR study was performed on EQUINOX 55 (Bruker) equipped with a MCT detector. The samples were degassed at 550 °C for 1 h under He in a high-temperature reaction chamber containing a Praying Mantis diffuse reflection attachment (Harrick). Small aliquots of deuterated acetonitrile (CD_3CN) were carried by He and sample was exposed to CD_3CN at room temperature for 15 min. Prior to the characterization, the physically adsorbed acetonitrile was removed by flowing He at room temperature for 1 h. For FT-IR spectroscopic study on the samples with adsorbed pyridine, the spectra were collected at 120 °C after removing the weakly adsorbed pyridine at 250 °C under He for 1 h.

2.2.3 Catalytic Reaction

All chemicals used in the reactions were purchased from Sigma-Aldrich and used without further purification. In a typical experiment for converting DHA into methyl lactate (ML), 0.3125 mmol of DHA and 1.00 g of methanol were mixed within a 4 mL glass vial (Fisher Scientific). A corresponding amount of Sn-MFI catalysts with a DHA-to-Sn molar ratio of 127 was added to this mixture. The reactions were carried out at 70 °C.

The same reaction conditions were also applied for pyruvaldehyde (PA, a 40 wt % aqueous solution). Xylose isomerization to xylulose and lyxose was performed in MeOH in a 4 mL glass vial. Typically, 1 g of xylose solution (1 wt % xylose) and 20 mg of catalyst were mixed in the reactor (xylose/Sn = 27). The glucose isomerization reaction was carried out under the same conditions over the Sn-MFI catalysts (glucose/Sn = 23). All reactions were performed for regular intervals on a temperature-controlled aluminum heating block with 1000 rpm stirring. After each reaction, the reactor was cooled in an ice bath for 20 min. The reactors were weighed before and after the reactions to ensure no leaking occurred. Naphthalene was used as an internal standard for all reactions.

2.2.4 Sample Analysis

DHA, ML, PA, and glyceraldehyde (GLA) were analyzed on an Agilent 6890 instrument equipped with an FID detector and a Restek RTX-VMS capillary column (30.0 m length, 0.25 mm id and 0.25 µm film thickness). Analyses of isomerization reactions of pentose (C_5) and hexose (C_6) sugars were carried out using liquid chromatography (LC, Shimadzu LC-20AT) with a BIO-RAD HPX-87H HPLC column operated at 30 °C. The mobile phase is 0.005 M sulfuric acid with a flow rate of 0.6 mL min^{-1}. The pentose and hexose sugars were quantified with a refractive index detector (RID-10A). In addition, a turnover frequency (TOF) value was calculated, which is defined as moles of product divided by moles of Sn per reaction time (h) when the product yield lies between 5 and 20%. On the basis of the ICP analysis (wt % of Sn in the catalyst), moles of Sn were calculated according to the reaction conditions.

2.3 Results and Discussions

Hierarchical stannosilicate molecular sieves with ordered mesoporosity and MFI topology (three dimensionally ordered mesoporous imprinted (3DOm-i) Sn-MFI) were successfully synthesized. This result was published in *ACS Catalysis*.[56]

The morphology of synthesized samples was characterized by SEM (Figure 2.1). As shown in Figure 2.1c, Sn-MFI_L synthesized in fluoride media shows a large particle size, approximately 60 μm × 15 μm × 3 μm, and a typical coffin shape of the MFI crystal. Sn-MFI_N sample was synthesized in the presence of hydroxide ions (OH^-) and has a particle size from 250 to 350 nm (Figure 2.1b). Different from conventional zeolites with MFI topology, 3DOm-i Sn-MFI with a particle size of around 1 μm is composed of spherical primary particles having a close packing arrangement. The primary particle size is around 30 nm, consistent with the value calculated from the low-angle X-ray diffraction measurement shown below (Figure 2.4b), revealing that a confined growth in the 3DOm carbon has been achieved in this synthesis.

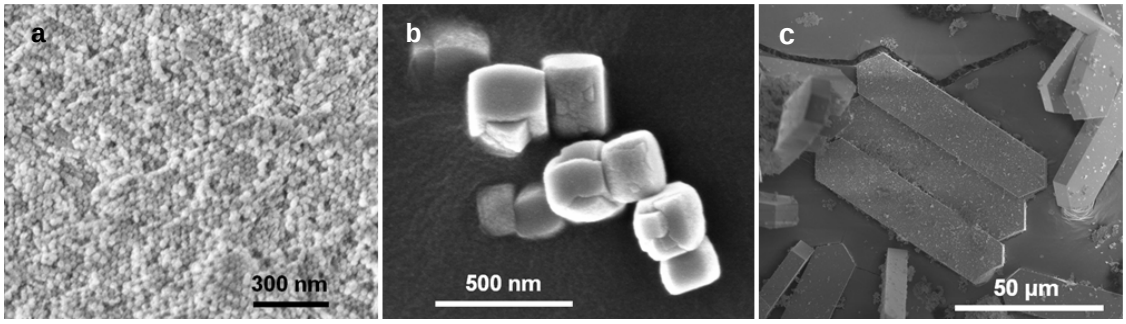

Figure 2.1 SEM images of (a) 3DOm-i Sn-MFI, (b) Sn-MFI_N, and (c) Sn-MFI_L.

The sole presence of the framework Sn, the Lewis acid site, in the three Sn-MFI

samples was evident by CD_3CN FT-IR characterization. After the Sn-MFI samples were exposed to CD_3CN vapors, the weakly adsorbed CD_3CN was removed from the solid samples by flowing He at room temperature for 1 h. As displayed in Figure 2.2a, the FT-IR spectra of all three Sn-MFI samples showed bands at around 2275 cm^{-1}, consistent with the ν (C≡N) stretching mode of acetonitrile adsorbed on silanol groups.[45, 46] The bands near 2308 cm^{-1} are associated with CD_3CN bound to isomorphously substituted Sn Lewis acid sites, in good agreement with previous reports.[46, 51, 57] The bands at both 2275 and 2308 cm^{-1} show a shift for the Sn-MFI_L synthesized in the presence of F^-, which might be related to changes in the packing structure of CD_3CN within the pores of the sample with different morphology and hydrophobicity, as suggested in the previous literature.[57] In addition, the Lewis acidity of the catalysts is confirmed by FT-IR spectroscopic analysis of the pyridine saturated samples after a heat treatment at 250 °C for removing the weakly adsorbed pyridine. As shown in Figure 2.2b, Sn-MFI samples gave a strong absorption band at 1455 cm^{-1}, corresponding to pyridine molecules bound with Lewis acidic Sn sites.[52, 58] Owing to its Lewis acidity, the Sn site is able to adsorb pyridine at 250 °C, similar to other Sn-containing molecular sieves. [59] A very weak absorption band at 1546 cm^{-1} associated with Brønsted acid was also observed in the spectra.[52, 58] Diffuse reflectance UV-Vis (DR-UV) spectroscopy was also used to show framework Sn Lewis acidity of the catalysts in Figure 2.3. The UV-Vis signal at around 200 - 205 nm is in good agreement with tetrahedrally coordinated Sn, as suggested in the previous literature.[60-64] An absorption at ~220 nm can be assigned to charge transitions from O^{2-} to Sn^{4+} in tetrahedral coordination.[60] All samples exhibited

no band at 280 nm which arises from Sn-O-Sn type of species. All the three characterizations performed on the Sn-MFI samples clearly indicate that the prepared samples possess mainly framework coordinated Sn atoms, which are responsible for the Lewis acid sites. A small number of Brønsted acid sites might also be present in the samples as a result of silanol defects.

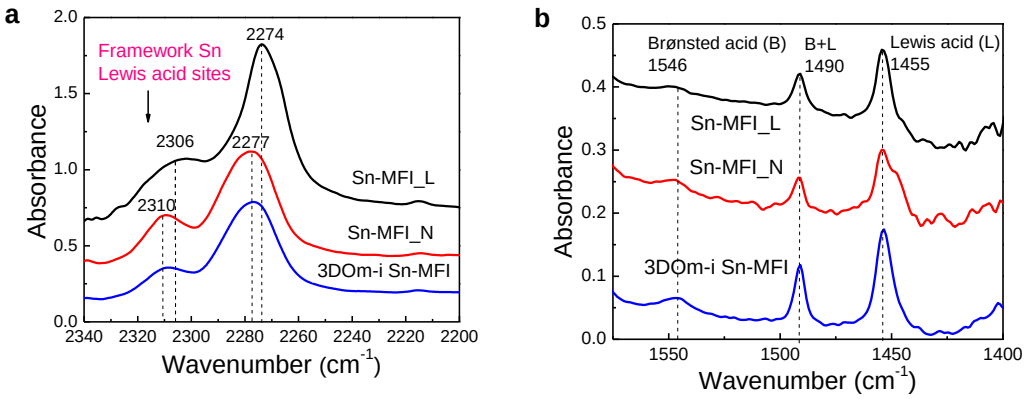

Figure 2.2 FT-IR spectra of 3DOm-i Sn-MFI, Sn-MFI_N, and Sn-MFI_L after adsorbing (a) deuterated acetonitrile (CD_3CN) and (b) pyridine.

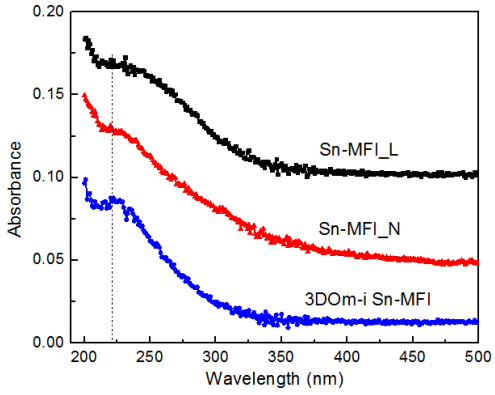

Figure 2.3 Diffuse reflectance UV-Vis (DR-UV) spectra of the Sn-MFI catalysts.

Figure 2.4 shows the XRD patterns of 3DOm-i Sn-MFI, Sn-MFI_N, and Sn-MFI_L synthesized in the study. Characteristic peaks corresponding to the MFI topology are observed for all three samples, indicating highly crystalline MFI zeolites have been synthesized without forming other impurity phases. The diffraction pattern of 3DOm-i Sn-MFI made from the seeded growth method exhibits broader peaks than the ones of Sn-MFI_N and Sn-MFI_L because of a small primary particle size. In the low-angle region of 2θ (0.2°−1.4°), four clear diffraction peaks were observed for the 3DOm-i Sn-MFI, revealing that the hierarchical Sn-MFI possesses a highly ordered mesoporous structure formed by a close-packing of primary particles.[29, 54] These diffraction peaks can be indexed to the (111), (220), (311), and (420) planes according to a face-centered-cubic structure.[29] The size of the unit cell calculated from the diffraction peaks is 41 nm, corresponding to a primary particle size of 29 nm, consistent with SEM images shown in Figure 2.1. On the contrary, the conventional Sn-MFI zeolites did not show diffraction peaks.

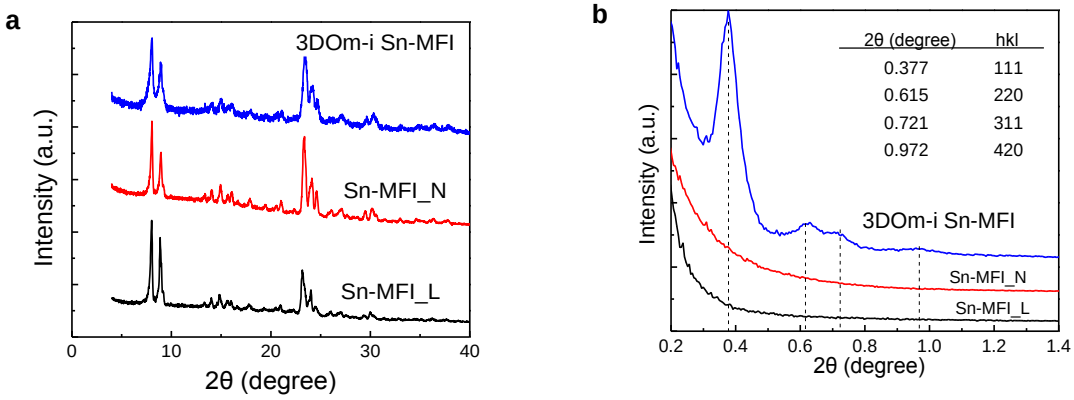

Figure 2.4 (a) XRD and (b) SAXS patterns of 3DOm-i Sn-MFI, Sn-MFI_N, and Sn-MFI_L samples.

Ar adsorption−desorption isotherms and pore size analyses of the three Sn-MFI samples are shown in Figure 2.5. The sharp adsorption uptake in the low relative pressure range, $P/P_0 < 0.1$, indicates the presence of microporosity in the samples. For 3DOm-i Sn-MFI, a gradual increase is observed in the relative pressure range from 0.5 to 0.8, corresponding to the imprinted mesoporous structure. Furthermore, pore size distributions of the three Sn-MFI samples were estimated from nonlocal density functional theory (NLDFT) (in Figure 2.5b). This result further confirms the presence of dual micro- and mesoporosity in the 3DOm-i Sn-MFI sample with micropores around 0.6 nm and a relatively narrow mesopore distribution from 4 to 11 nm. The BET surface area, micropore volume, external surface area and total pore volume estimated by N_2 adsorption-desorption isotherms are summarized in Table 2.1. The micropore volumes for Sn-MFI_L, Sn-MFI_N and 3DOm-i Sn-MFI were 0.116, 0.117 and 0.119 $cm^3\ g^{-1}$, respectively, clearly demonstrating that the MFI type crystal structure is well retained in the Sn-MFI samples. The BET surface area, external surface area and total pore volume also increased with reducing the particle size of the Sn-MFI samples. The molar ratio of Si to Sn in each sample was quantified by ICP analysis (Table 2.1).

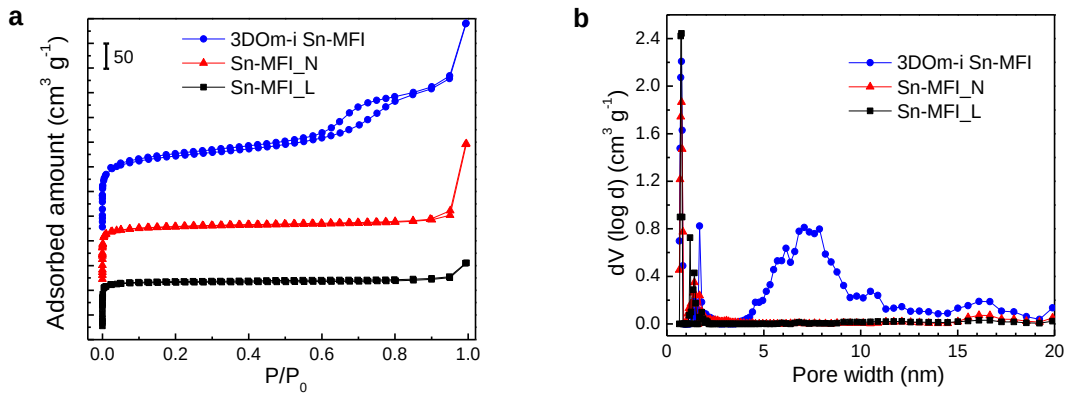

Figure 2.5 (a) Argon adsorption–desorption isotherms and (b) pore size distributions using NLDFT for 3DOm-i Sn-MFI, Sn-MFI_N, and Sn-MFI_L samples. Pore size distributions were calculated by using a NLDFT (nonlocal density functional theory) adsorption model, which describes Ar adsorbed in cylindrical pores (AsiQwin 1.02, Quantachrome).

Table 2.1 Textural Information of the Sn-MFI samples from N_2 adsorption-desorption isotherms and composition information

	BET surface area[a] ($m^2\ g^{-1}$)	Micropore volume[b] ($cm^3\ g^{-1}$)	External surface area[b] ($m^2\ g^{-1}$)	Total pore volume[c] ($cm^3\ g^{-1}$)	Si/Sn (initial gel)	Si/Sn (final product)[d]
Sn-MFI_L	330	0.116	62	0.185	200	256
Sn-MFI_N	386	0.117	149	0.293	125	135
3DOm-i Sn-MFI	459	0.119	191	0.402	125	133

[a] Calculated from P/P_0 range of 0.05-0.25 using BET equation. [b] Calculated by t-plot method.
[c] Calculated from the amount adsorbed at $P/P_0 = 0.975$. [d] Determined by ICP-OES.

The catalytic activity of the synthesized Sn-MFI samples was systemically evaluated using the isomerizations of C_3, C_5 and C_6 sugars in MeOH. Scheme 2.2 illustrates the proposed reaction pathway for the conversion of triose sugars, DHA and GLA, in the presence of MeOH. PA, an initial intermediate formed by the dehydration of DHA or GLA, can be converted to either ML by Lewis acids or pyruvaldehyde

dimethylacetal (PADA) by Brønsted acids.[1, 58] It has been shown that Sn-containing materials as highly active Lewis acid catalysts can activate the carbonyl and hydroxyl groups in PA, facilitating an intramolecular hydride shift similar to the MPV reactions catalyzed by Lewis acids.[65] On the other hand, weak Brønsted acid sites can promote the initial dehydration step for producing PA from DHA or GLA, whereas strong Brønsted acids should be avoided because they can further catalyze the formed PA to produce PADA instead of ML in the second step of the reaction pathway.[52, 66]

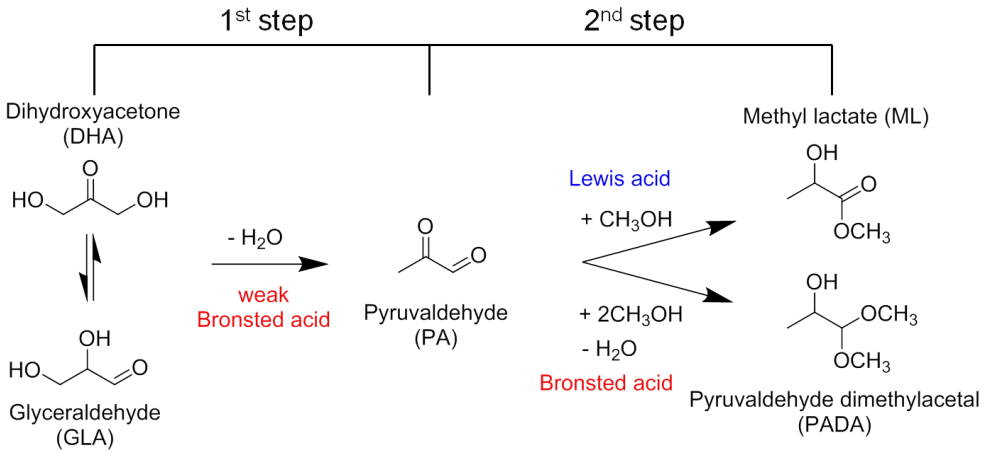

Scheme 2.2 Reaction pathway for the conversion of dihydroxyacetone (DHA) or glyceraldehyde (GLA) in Methanol (MeOH) into either methyl lactate (ML) or pyruvaldehyde dimethylacetal (PADA).

For all three Sn-MFI samples, no PADA was detected during the reaction starting from DHA in MeOH at 70 °C, indicating that the Sn-MFI catalysts do not have strong Brønsted acidity. Figure 2.6 reveals that the 3DOm-i Sn-MFI catalyst produces the highest yield of ML. After 24 h, 93.8% yield of ML was achieved for the 3DOm-i Sn-MFI catalyst while the yields of ML for Sn-MFI_N and Sn-MFI_L were 86.3% and 47.5%,

respectively. As shown in Figure 2.7, 3DOm-i Sn-MFI and Sn- MFI_N gave a higher initial reactivity (TOF = 15.1 for 3DOm-i Sn-MFI and TOF = 13.9 for Sn-MFI_N) than Sn-MFI_L (TOF = 4.3) under the reaction conditions. Since it has been known that weak Brønsted acidity from silanol groups associated with the surface terminal groups and defects in zeolites can catalyze the dehydration reaction from DHA to PA,[67-69] it is anticipated that different activities of the Sn-MFI catalysts might be due to the number of weak Brønsted acid sites located in these catalysts.

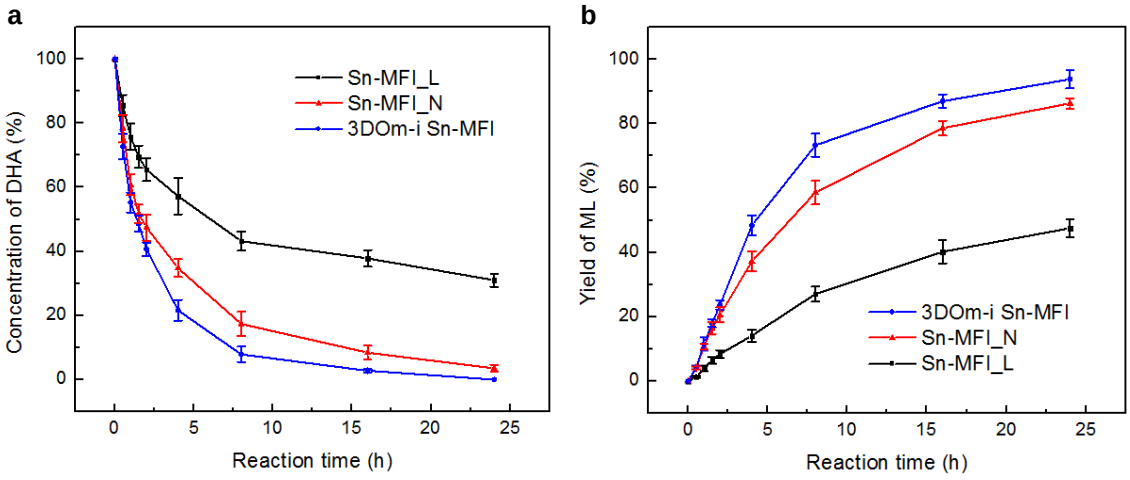

Figure 2.6 Reaction profiles for (a) the conversion of DHA to ML and (b) ML yield on different Sn-MFI catalysts. The error bars in the figures are from three repeated reactions.

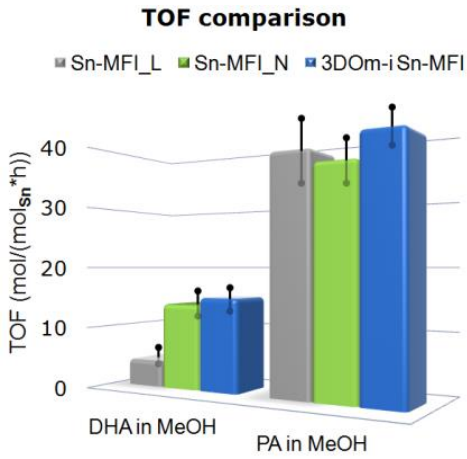

Figure 2.7 Initial catalytic activities of Sn-MFI catalysts for the conversions of DHA and PA in the presence of MeOH. The error bars in the figures are from three repeated reactions.

Figure 2.8 shows FT-IR spectra collected from the samples after removing the adsorbed water by degassing at 550 °C. In this figure, the band at 3745 cm^{-1} comes from the silanol groups on the external surface of the samples. The features at 3726 and 3700 cm^{-1} can be assigned to the silanol groups located inside the micropores of zeolites.[70, 71] The band around 3500 cm^{-1} is ascribed to silanol nests that occur at extended defects.[70] Sn-MFI_L shows weaker absorption for all three types of Si−OH groups and defects than Sn-MFI_N and 3DOm-i Sn-MFI, clearly indicating the use of F^- in the synthesis led to fewer defects and lower external surface area. Notably, the 3DOm-i Sn-MFI exhibits the highest concentration of Si-OH groups among the measured samples. It is very likely the high concentration of weak Brønsted acids associated with silanol groups resulted in the superior catalytic performance of the 3DOm-i Sn-MFI catalyst for the conversion of DHA into ML (Figure 2.9).

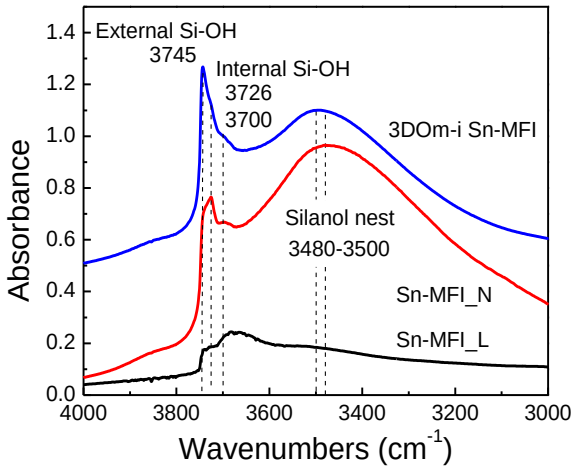

Figure 2.8 FT-IR spectra in the OH-stretch region (3800 – 3000 cm^{-1}) of the Sn-MFI catalysts.

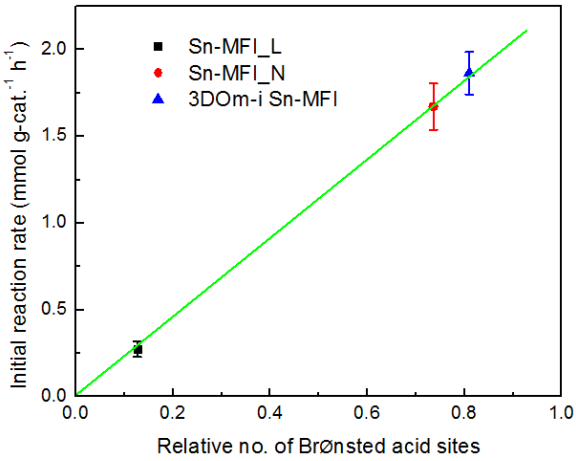

Figure 2.9 Plots of initial reaction rates against relative number of Brønsted acid sites for the conversion of DHA into ML. Due to the different types of silanol groups in these materials, it is difficult to directly quantify the concentration of silanol groups. Using pyridine FT-IR spectra in Figure 2.2b and Sn concentration measured by ICP, thus, relative number of Brønsted acid sites for each catalyst was obtained. At first, peak areas at 1455 cm^{-1} (Lewis acid sites) and 1546 cm^{-1} (Brønsted acid sites) in Figure 2.2b were calculated. The peak area at 1455 cm^{-1} is proportional to Sn content. Based on the peak area for Sn-MFI_L at 1455 cm^{-1}, relative number of Brønsted acid sites was calculated by normalization. Initial reaction rates were plotted in terms of relative number of Brønsted acid sites. The result clearly indicates that dehydration of DHA to PA is linearly correlated to the number of Brønsted acid sites.

In addition, product distributions with reaction time for the conversion of DHA into ML (Figure 2.10) reveal that the concentration of intermediate PA remains lower than the one of DHA or GLA during the whole reaction, implying that the dehydration reaction from DHA to PA is a rate-limiting step for the conversion of DHA into ML. Because the rate-limiting step for the reaction from DHA to ML is the first step, dehydration reaction, the catalytic performance of the Sn-MFI catalysts is determined by the number of weak Brønsted acids in the catalysts. To further understand the effects of mass transport on the catalytic performance of the Sn-MFI catalysts, PA, the product from the dehydration of DHA, was used as a reactant to produce ML over the catalysts. In the reaction, PA is directly converted into ML over the Lewis acid sites of the Sn-MFI catalysts through an intramolecular 1,2 hydride shift. For the reaction, all three Sn-MFI catalysts possess similar initial activities, as shown in Figure 2.7, regardless of the crystal size or mesoporosity of the catalysts. The result strongly suggests that there is no diffusion limitation in the isomerization of PA for the tested Sn-MFI catalysts. Moreover, because the dehydration is the rate-limiting step in the two-step reaction from DHA to ML, the catalytic performance of Sn-MFI catalysts for the conversion of DHA to ML can be optimized by further enhancing the dehydration reaction through tailoring the number of defects and silanol groups on the catalysts.

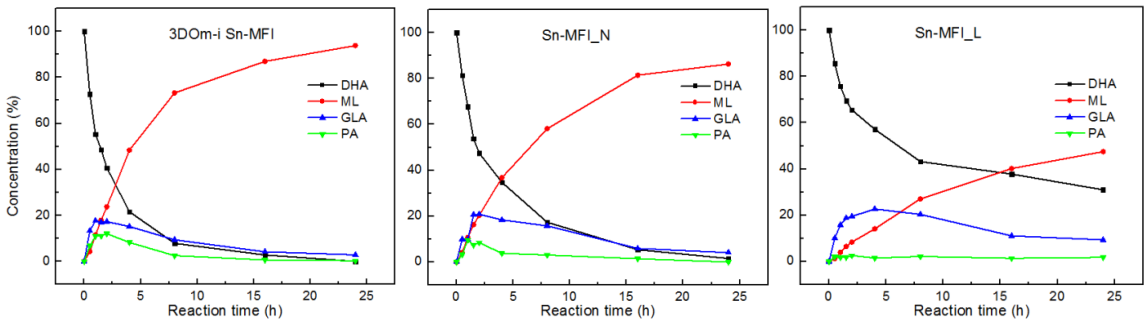

Figure 2.10 Product distributions for the conversion of DHA into ML over Sn-MFI catalysts. Reaction conditions are as follows: 0.3125 mmol DHA; 1 g methanol (MeOH); a DHA to Sn molar ratio of 127; 70 °C.

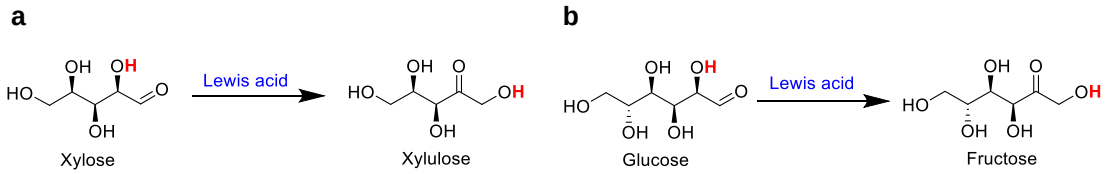

Scheme 2.3 Reaction pathway for the Lewis acid catalyzed isomerization of (a) xylose or (b) glucose, respectively.

The isomerizations of pentose (C_5) and hexose (C_6) sugars in MeOH have also been evaluated over the three Sn-MFI catalysts (Scheme 2.3). Xylose, which is the most abundantly available pentose sugar in hemicellulose, undergoes isomerization to generate xylulose and lyxose via an intramolecular 1,2 hydride shift.[38] On the other hand, when glucose is chosen as a starting substrate, the resulting products are fructose and mannose.[39] Xylose isomerization to xylulose and lyxose was performed in MeOH in a 4 mL glass vial. The test results are expressed in terms of TOF, as depicted in Figure 2.11. In both reactions, Sn-MFI_L was nearly inactive because of the large crystal size and small external surface area. 3DOm-i Sn-MFI results in a remarkable catalytic performance for the reactions, showing at least 3-fold higher activity than Sn-MFI_N. In

the case of xylose isomerization, the enhanced reaction rate on 3DOm-i Sn-MFI can be explained by the reduced diffusion limitation of xylose within the hierarchically structured catalyst. The ten-membered ring of MFI structure is composed of straight and sinusoidal channels, depending on the crystal orientation.[72, 73] As a matter of fact, it has been suggested that molecules smaller than 0.63 nm should be able to sufficiently fit into the micropores of an MFI crystal.[72, 74] Because of the slightly larger molecular size of xylose (0.65 nm, Stokes diameter; 0.68 nm, equivalent molar diameter) compared with the pore size of the MFI crystal,[75] diffusion limitation might become critical for the reaction, giving rise to more pronounced differences in the performances between the hierarchical, 300 nm, and bulky Sn-MFI catalysts.

For glucose (C_6 sugar) isomerization, all TOF values appear to be very low, although better activity was observed for 3DOm-i Sn-MFI zeolite. Taking into account the Stokes diameter of glucose (0.73 nm),[76] it is quite challenging for glucose to diffuse into the micropores of the MFI catalyst. This isomerization reaction for glucose is very likely to occur only on the exterior surface of the Sn-MFI catalysts. These results are in good agreement with earlier studies,[39, 50] showing that Ti- or Sn-MFI zeolites are not active for glucose isomerization because glucose is too large to enter the micropores of the MFI crystal. The TOF values for the three Lewis acid catalyzed reactions are summarized in Table 2.2. When the substrate changes from C_3 to C_5, the Sn-MFI catalysts begin to show different catalytic activities because of the diffusion limitation of xylose compared to C_3 sugars. For the reaction of an even larger sugar, glucose, it seems that the reaction happens only on exterior surfaces of the catalysts because glucose is

much larger than the MFI pore dimensions. The results clearly suggest that 3DOm-i Sn-MFI provides a superior catalytic performance for cellulosic sugar isomerizations, compared to conventional Sn-MFI. The enhanced catalytic activity is very likely because the mesopores imposed in the zeolites can considerably enhance the molecular diffusion of the bulky molecules.

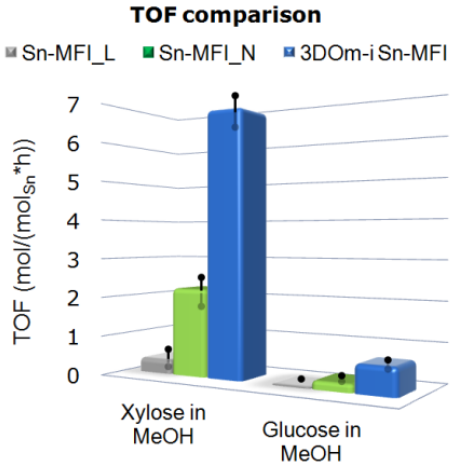

Figure 2.11 Initial catalytic activities of Sn-MFI catalysts for isomerizations of xylose and glucose. The error bars in the figures are from three repeated reactions.

Table 2.2 Summary of TOF for three Lewis acid catalyzed reactions

Catalyst	TOF[a] (h^{-1})		
	PA in MeOH	Xylose in MeOH	Glucose in MeOH
Sn-MFI_L	37.8 (± 5.8)	0.37 (± 0.05)	0.05 (± 0.01)
Sn-MFI_N	35.7 (± 4.1)	2.23 (± 0.42)	0.21 (± 0.07)
3DOm-i Sn-MFI	39.8 (± 3.6)	6.76 (± 0.43)	0.69 (± 0.15)

[a] 95% confidence interval in parentheses.

In addition to enhanced reaction rates, hierarchical zeolites with mesopores can also improve catalyst life time and reduce catalyst deactivation in various reactions.[28, 77, 78] During the course of triose isomerization, recent studies have reported that heterogeneous catalysts are deactivated due to coke accumulation on the catalyst surface.[48, 58, 79] To gain insights into the effect of mesoporosity on catalyst deactivation, high conversion results from PA to ML were collected over the prepared Sn-MFI catalysts and are presented in Figure 2.12. At the beginning of the reaction, the reaction rate for all Sn-MFI catalysts was the same as shown earlier. With the further progress of the reaction, the catalytic activities of the catalysts exhibited distinct differences. Specifically, 3DOm-i Sn-MFI gave 94.1% of ML yield after 10 h, whereas 83.4% and 74.8% yields of ML were obtained for Sn-MFI_N and Sn-MFI_L, respectively. Because an excess amount of methanol was used, the isomerization reaction can be approximated as pseudo-first order in the limiting reactant PA. Plots of $-ln(1-x)$ against reaction time (x is the product yield for this reaction) suggest that the reaction over 3DOm-i Sn-MFI is in a good agreement with the pseudo-first order approximation. However, the reactions over Sn-MFI_N and Sn-MFI_L show evident discrepancy from the approximation at high conversion (Figure 2.13). This is a strong indication that catalyst deactivation occurred slowly on the 3DOm-i Sn-MFI catalyst because the highly interconnected mesoporous structures allow facile molecular diffusion into and out of the micropores of the catalyst. Consequently, it was inferred that the Sn-MFI catalyst with hierarchical porosity shows slower deactivation, leading to better catalytic performances.

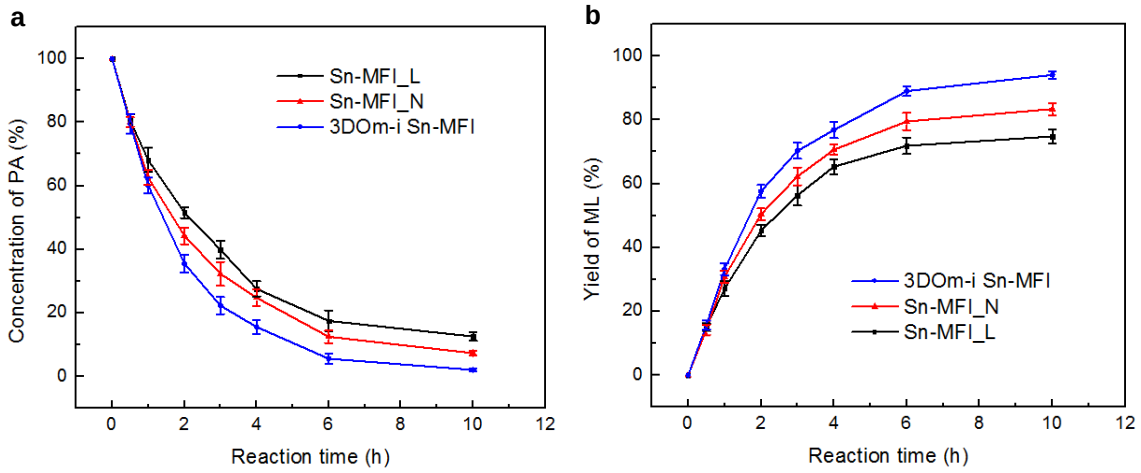

Figure 2.12 Reaction profiles for (a) the conversion of PA to ML and (b) ML yield using different Sn-MFI catalysts. The error bars in the figures are from three repeated reactions.

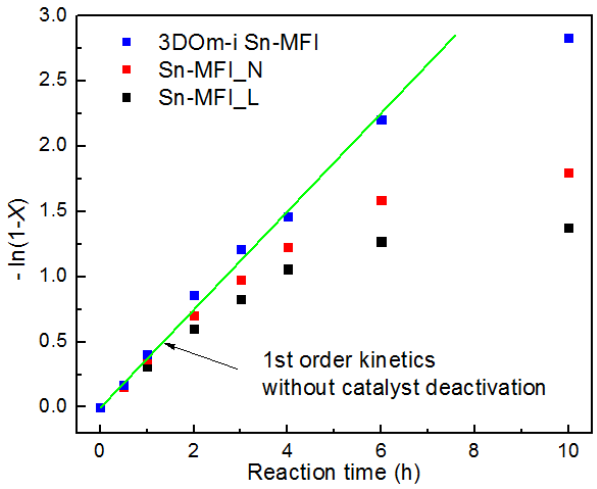

Figure 2.13 Plots of $-ln(1-x)$ against reaction time where *x* is the product yield for the conversion of PA into ML over Sn-MFI catalysts. In a constant-volume batch reactor, this reaction can be approximated as pseudo-first order in the limiting reactant PA, giving a straight line (green) in the figure. Among the catalysts, the reaction over 3DOm-i Sn-MFI agrees well with pseudo-first order reaction kinetics. The discrepancy shown in the Sn-MFI_N and Sn-MFI_L samples clearly implies the catalyst deactivation.

The feasibility of the seeded growth method for the synthesis of hierarchical Sn-MFI catalysts has been further explored using other commercially available carbon

materials. With the same approach used in the 3DOm-i Sn-MFI synthesis, hierarchical Sn-MFI was fabricated with carbon black BP2000 and activated carbon Norit SX Ultra, respectively. Cumulative pore volumes and pore size distributions estimated from NLDFT for the samples are presented in Figure 2.14. In these plots, hierarchical Sn-MFI materials synthesized within commercial carbon templates exhibit mesopores with a broad range from 3 to 20 nm. This is probably caused by disorderly interconnected carbon nanoparticles in the commercial carbons. Figure 2.15 displays a SEM image of Sn-MFI synthesized within carbon black BP2000. The Sn-MFI crystals seem to nucleate within the pores of the carbon template and grow up to outside of the carbon template during the repeated seeded growth process, leading to encapsulation of the carbon nanoparticles within the formed crystals. The results clearly indicate that the characteristics of hierarchical zeolite catalysts synthesized by the seeded growth method can be easily tailored by controlling the porous structures (e.g., pore size and interconnectivity) of the carbon templates.

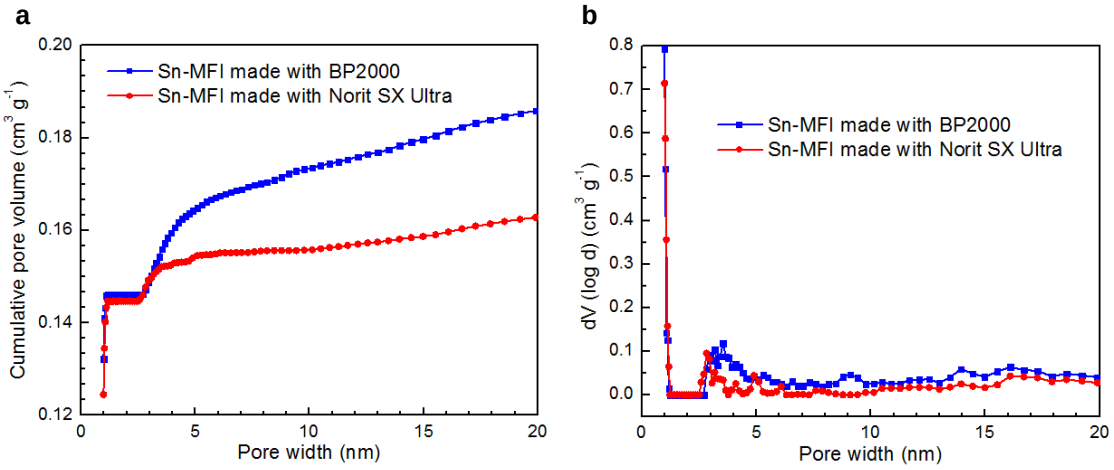

Figure 2.14 Cumulative pore volumes (a) and pore size distributions (b) using NLDFT of hierarchical Sn-MFI zeolites made with BP2000 and Norit SX Ultra, respectively, derived from N_2 adsorption-desorption isotherms. Pore size distribution and cumulative pore volumes were calculated by using NLDFT (nonlocal density functional theory) adsorption model which describes N_2 adsorbed in cylindrical pores (AsiQwin 1.02, Quantachrome).

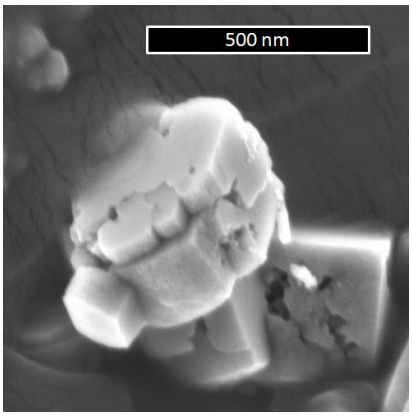

Figure 2.15 A SEM image of hierarchical Sn-MFI made with BP2000.

CHAPTER 3

BIFUNCTIONAL PT/SN-MFI CATALYSTS FOR ONE-POT CONVERSION OF GLYCEROL TO LACTIC ACID UNDER BASE-FREE ENVIRONMENTS

3.1 Introduction

Glycerol is an inevitable by-product from biodiesel production by the trans-esterification of vegetable oils and animal fats.[17] The rapid development of oleochemistry has lead to a dramatic increase in glycerol production from about 600 000 tons in 1992 to 1.1–1.5 million tons in 2010 with an average increase of 3.75% per year.[80] Glycerol can also be potentially obtained from non-edible biomass, such as microalgae, cellulose and its derivatives, in the near future.[81, 82] For these reasons, the conversion of glycerol to high-value chemicals has attracted much attention from both academia and industry.[83] Compared with hydrocarbons, glycerol is a highly functionalized molecule containing three hydroxyl groups. Selective hydrogenolysis, oxidation and dehydration of the hydroxyl group of glycerol have been extensively studied to synthesize numerous value-added compounds or intermediates.[14, 83-85] Particularly, the oxidation of glycerol produces a series of reaction pathways capable of generating various valuable oxygenated derivatives. However, due to the complex nature of these reaction pathways as shown in Scheme 3.1, controlling the selectivity to desired products is a grand challenge.

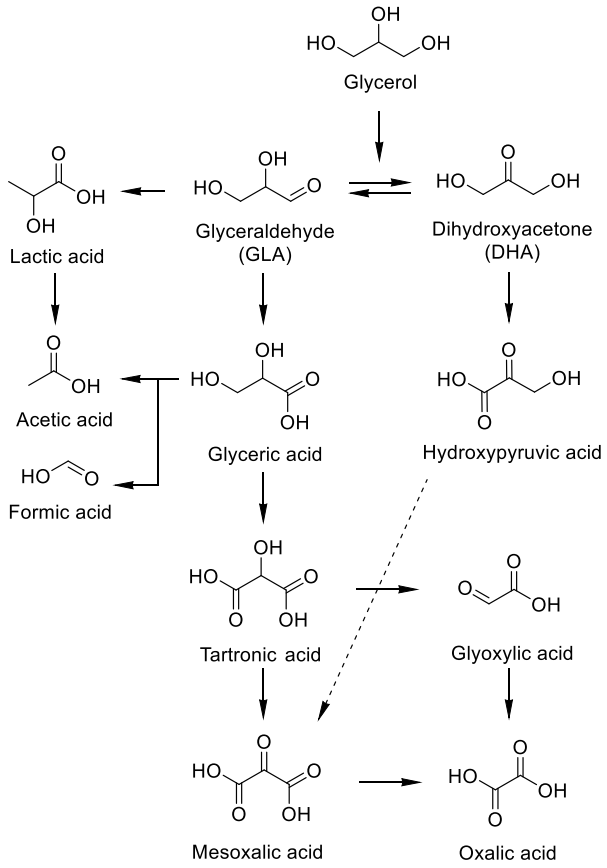

Scheme 3.1 General reaction pathways of glycerol oxidation.

Lactic acid (LA) and alkyl lactates have been widely used in food, pharmaceutical and chemical industries as platform chemicals and green solvents.[1, 5, 85] In particular, LA has been used as a precursor to synthesize polylactate or polylactic acid (PLA), the second most manufactured bioplastic in the world.[86] LA can be produced from petroleum feedstocks in high yields using mineral acid catalysts. But, the use of toxic chemicals (e.g. hydrogen cyanide) and the high cost for product separation gave rise to significant environmental concerns. Therefore, currently LA is mainly manufactured by the fermentation of carbohydrates. However, the efficiency and productivity of the fermentation processes are still low and need substantial improvements because of the

high cost of enzyme catalysts and the need for precise control of operating conditions.[58, 87] There is thus a persistent demand to develop efficient thermochemical pathways for the production of LA from new starting materials.[88, 89]

Although much research has been devoted to tailor the selectivity in glycerol oxidation, only a few reaction pathways can selectively convert glycerol into LA. Kishida et al. reported that LA is directly produced from the hydrothermal reaction of glycerol in the presence of NaOH at 300 °C.[90] During the hydrogenolysis of glycerol in alkaline solutions at 200 °C and 4.0 MPa H_2, LA has also been detected.[91, 92] These studies highlighted the potential of the production of LA from glycerol although the efficiencies or harsh reaction conditions of the reaction pathways may cause significant hurdles to their commercialization. Recently, a tandem reaction pathway has been developed to selectively transform glycerol into LA. In this route, glycerol is first selectively oxidized to DHA and GLA on metal catalysts, and then undergoes base-catalyzed dehydration and benzilic acid rearrangement to produce LA. Shen et al. first reported that 85.6% of LA selectivity was achieved from this reaction pathway using the Au–Pt/TiO_2 catalyst in the presence of NaOH, and confirmed that DHA and GLA were formed as intermediates during the reaction.[93] Similar performances have also been achieved on Au/CeO_2 and Au–Pt/nanocrystalline CeO_2 catalysts under basic conditions.[94, 95] The use of a base in the tandem reaction pathway is crucial because hydroxide ions not only facilitate H-abstraction in the initial dehydrogenation of the hydroxyl group of glycerol but also catalyze the reaction of DHA/GLA to LA.[84, 93, 96, 97] Although a high yield of LA can be obtained from this reaction pathway, the use of base catalysts causes the formation of

acid salts (i.e. lactate). Additional reaction and separation steps are required to isolate LA, which not only increase the cost of production but also produce a stoichiometric amount of salt wastes. Development of a base free reaction pathway for the production of LA from glycerol using heterogeneous catalysts is thus highly desirable. In this scenario, Xu and coworkers succeeded in attaining 66.6% of LA selectivity at 13.6% of glycerol conversion by employing Au-Pd/TiO_2 in the presence of $AlCl_3$, and proposed that the second step reaction of DHA/GLA to LA was catalyzed by $AlCl_3$.[98] Although no base catalyst was used in the reaction, separation of the $AlCl_3$ catalyst and catalyst poisoning by chlorine were still issues for the catalytic process.

In order to overcome the challenges, herein we developed an efficient base-free reaction pathway to selectively convert glycerol into LA in the aqueous phase using a bifunctional Pt/Sn-containing zeolite catalyst. In the reaction pathway, glycerol is first oxidized to DHA/GLA with O_2 on Pt nanoparticles under mild oxidation conditions. The water tolerant Lewis acid catalyst, Sn-MFI, then catalyzes the isomerization of DHA/GLA to LA with high selectivity. In this study, Sn-containing zeolites were selected due to their outstanding Lewis acidity in the aqueous phase. Under optimized reaction conditions the bifunctional catalyst achieved over 80% selectivity to LA.

3.2 Experimental

3.2.1 Catalyst Preparation

Sn-MFI with a Si/Sn molar ratio of 135 (confirmed by ICP) was prepared using the method reported previously,[99] and this material is 300 nm sized Sn-MFI_N as shown in

Chapter 2. Silicalite-1, pure siliceous zeolite with MFI topology, was synthesized following the protocol reported by Watanabe et al.[100] Typically, 2.44 g of tetrapropylammonium hydroxide (TPAOH, 40% Alfa Aesar) was mixed with 4 g of TEOS (98%, Alfa Aesar) and then 11.67 g of deionized water was added to this solution. The mixture was stirred at 80 ^{o}C for 24 h to obtain the final molar composition of 1 SiO_2 : 0.25 TPAOH : 38 H_2O. The resulting gel was transferred to an autoclave for crystallization at 170 ^{o}C for 24 h. The solid product was washed with deionized water, dried at 100 ^{o}C overnight and calcined at 550 ^{o}C for 12 h. The detailed preparation procedures of Sn-BEA were described in previous literature.[101] Briefly, tetraethylorthosilicate (TEOS, 98%, Alfa Aesar) was mixed with tetraethylammonium hydroxide (TEAOH, 35 wt%, Alfa Aesar) solution and stirred for 1 h until a homogeneous solution was formed. Tin (IV) chloride pentahydrate ($SnCl_4 \cdot 5H_2O$, Alfa Aesar) dissolved in water was added into the above solution and the resulting solution kept stirring in a fume hood until ethanol (generated from hydrolysis of TEOS) and some water were evaporated. After required weight was achieved, a suspension of dealuminated zeolite beta crystal seeds were added into the gel and well mixed. Lastly, hydrofluoric acid (48%, Alfa Aesar) was added into the mixture by mixing with a plastic spatula. The final molar composition of the gel was SiO_2 : 0.008 SnO_2 : 0.54 TEAOH : 0.54 HF : 7.5 H_2O. The solid-like white gel was moved into an autoclave and heated at 140 ^{o}C for 4 days under rotation. The as-made product was washed thoroughly by filtration with 2 L of deionized water, dried in an oven at 100 ^{o}C overnight, and calcined at 550 ^{o}C for 12 h to obtain Sn-BEA with a Si/Sn molar ratio of 126.

Bifunctional catalysts were prepared by impregnating Sn-MFI, silicalite-1, Sn-BEA and TiO_2 (P25, Degussa), respectively, using an aqueous solution of $H_2PtCl_6 \cdot 6H_2O$ (99.9%, Alfa Aesar). After the impregnation, the samples were dried at 100 ^oC overnight. For reduction, the impregnated sample was placed on a small beaker in the middle of a plastic bottle. Ethanol used as a reducing agent was placed at the bottom of the bottle without directly contacting with the sample. The reduction was performed in an oven at 70 ^oC for 4 h. Obtained products were washed with deionized water by centrifugation and dried at 100 ^oC overnight. The Pt loading was fixed at 1.5 wt%, on the basis of the final product.

3.2.2 Catalyst Characterization

FT-IR spectroscopy was carried out on EQUINOX 55 (Bruker) with an MCT detector. The sample was degassed at 550 °C for 1 h under He in order to remove adsorbed water. After that, FT-IR spectra were collected on the sample at 120 °C. For pyridine adsorption, small aliquots of pyridine were subsequently exposed to the sample at 120 °C for 15 min. Prior to the characterization, the weakly adsorbed pyridine was removed by flowing He at 250 °C for 1 h and the spectra were then collected at 120 ^oC. Powder X-ray diffraction (XRD) patterns of the catalysts were collected on a X-ray diffractometer (X'pert Pro, PANalytical) operated at an acceleration voltage of 45 kV and a current of 40 mA using CuK_α radiation. The XRD data for the prepared samples were recorded in a 2θ range of 4-60^o. The nitrogen adsorption-desorption isotherms were measured using an automated gas sorption analyzer (Autosorb iQ_2, Quantachrome) after the samples were degassed at 300 ^oC for 10 h under vacuum. Elemental analysis

for the samples was carried out using inductively coupled plasma-optical emission spectroscopy (ICP-OES, iCap 6500 Dual view, Thermo Scientific). The morphology of each catalyst was examined by transmission electron microscopy (TEM, JEOL 2000FX) with an accelerating voltage of 200 kV. The particle size distribution was calculated by counting over 60 particles. The average Pt particle size in this distribution was determined using the equation $\sum d^3 / \sum d^2$ where d (nm) is a size for each particle. Pt metal surface area was measured by H_2 chemisorption using a chemisorption analyzer (ChemBET pulsar TPR/TPD, Quantachrome). In this experiment, the catalysts were reduced at 300 ^oC for 10 h under the flow of 5% H_2/95%N_2 gas and H_2 chemisorption was then carried out at room temperature with a gas flow rate of 12 mL min^{-1}. From this result, the average Pt crystallite diameter for each catalyst was estimated with the assumption of spherical geometry.

3.2.3 Catalytic Test

In a typical experiment for converting glycerol (99.5%, Alfa Aesar) to lactic acid (LA), Pt/Sn-MFI or Pt/AC catalyst and 80 mL of 0.2 M aqueous solution of glycerol (glycerol/Pt molar ratio = 350, glycerol/Sn molar ratio = 226) were put into a 160 mL Parr reactor. Initially, the reactor was pressurized with nitrogen at 0.62 MPa. After heating the reactor from room temperature to 100 ^oC, the oxidation was allowed to proceed under stirring at 1000 rpm by switching from inert gas to oxygen (0.62 MPa). Time course of glycerol oxidation was monitored by taking samples (0.5 mL) for analysis at specified time intervals. Under the same reaction conditions, Pt/Sn-BEA catalyst was tested with the glycerol to Sn molar ratio of 211. For Pt/silicalite-1 and Pt/TiO_2 samples,

the same reaction conditions were also applied, except the Sn to glycerol molar ratio of 0. In addition, a conversion of PA into LA has been performed over Pt/Sn-MFI, Sn-MFI, Pt/Sn-BEA and Sn-BEA catalysts. The catalyst, corresponding to 226 of PA to Sn molar ratio, was added into a 1.3 g of 0.2 M PA dissolved in water. The reaction occurred in a 4 mL glass vial reactor which was placed in a temperature-controlled aluminum heating block set to 100 °C under 1000 rpm stirring. After the specified times of the reaction, the glass reactors were quenched in ice for 20 min, dried and weighed before opening to ensure no leaking occurred during the reaction.

3.2.4 Sample Analysis

After the reaction, glycerol, glyceric acid (20 wt% in water, TCI), PA (40 wt% in water, Aldrich), pyruvic acid (98%, Aldrich), LA (98%, Sigma Aldrich), glyceraldehyde (90%, Sigma Aldrich), acetic acid (99.9%, Fisher Scientific), DHA (dimer, 97%, Sigma Aldrich), oxalic acid (97%, Fluka), tartronic acid (98%, Alfa Aesar) and glycolic acid (99%, Sigma Aldrich) were quantified in the reaction vials. The quantitative analysis of these samples was conducted by Agilent 6890 gas chromatography equipped with an FID-detector and a Restek RTX-VMS capillary column (30.0 m length, 0.25 mm id, 1.4 µm film thickness). Besides, the products were also cross-checked on HPLC (Shimadzu, LC-20AT) using an HPX-87H column operated at 30 ^{o}C. In HPLC experiments, ultraviolet (UV) and refractive index (RI) detectors were utilized to determine the chemicals using 0.005 M H_2SO_4 aqueous solution as a mobile phase. The flow rate of the mobile phase was fixed at 0.6 mL min^{-1}.

3.3 Results and Discussions

In this study, Sn-containing zeolites were selected due to their outstanding Lewis acidity in the aqueous phase. Under base free and mild reaction conditions, 80.5% selectivity of lactic acid (LA) was achieved at 89.8% conversion of glycerol using a bifunctional Pt/Sn-MFI catalyst. This work has been published in *Green Chemistry*.[102]

Bifunctional Pt/Sn-containing zeolite catalysts were prepared by the reduction of Pt precursors deposited on Sn-containing zeolites with the MFI and BEA structures, respectively (Sn-MFI and Sn-BEA). Sn-containing zeolites were chosen in this study because of their outstanding Lewis acidity for catalyzing the isomerization of sugar molecules in the aqueous phase, in particular for C_3 sugar derivatives, such as DHA, GLA and pyruvaldehyde (PA), as described in Chapter 2 of this thesis.

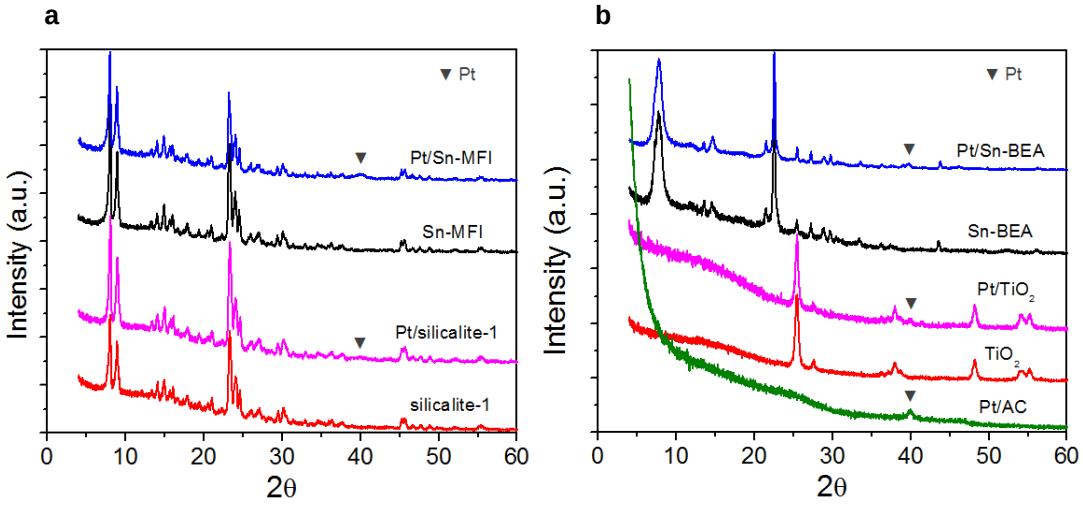

Figure 3.1 XRD patterns of the prepared catalysts: (a) Pt/Sn-MFI, Sn-MFI, Pt/silicalite-1 and silicalite-1, and (b) Pt/Sn-BEA, Sn-BEA, Pt/TiO_2, TiO_2 and Pt/activated carbon (AC).

Figure 3.1 shows that the Pt on the Sn-MFI sample possesses a diffraction peak at 2θ = 39.8°, corresponding to the (111) plane of Pt crystals with a cubic close-packed

structure.[103] It is evident that the formation of crystalline Pt nanoparticles on Sn-MFI does not influence the original crystalline structure of the MFI. The TEM image confirms that the Pt nanoparticles were well dispersed on the Sn-MFI catalyst surface (Figure 3.2a). The particle size distribution of Pt calculated from TEM images is shown in Figure 3.2b. The size of the Pt nanoparticles mainly lies between 4 and 7 nm with an average of 6.7 nm, in good agreement with the size of 7.9 nm determined by H_2 chemisorption (Table 3.1). Pt on silicalite-1, Sn-BEA (which is the same as Sn-BEA-HF in Chapter 4), and TiO_2 were also synthesized using the method applied for Pt/Sn-MFI. The particle size of Pt on the samples is in the range of 6.4 nm to 9.5 nm, similar to the Pt/Sn-MFI sample (Table 3.1). The crystalline structure of these supports is also well retained during the loading of Pt (Figure 3.1).

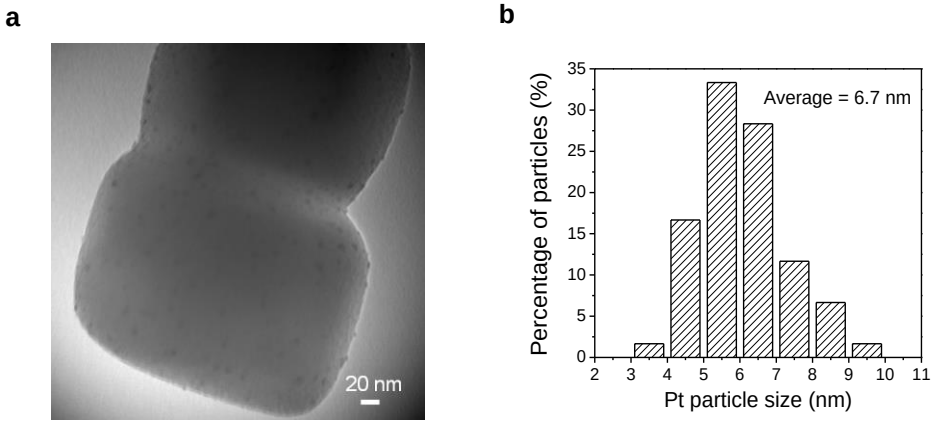

Figure 3.2 (a) A TEM image and (b) Pt particle size distribution estimated from TEM images for the Pt/Sn-MFI catalyst. The average Pt particle size was estimated using the equation $\Sigma d^3/\Sigma d^2$ where d is the size of each Pt particle.

Table 3.1 Pt metal surface area and crystallite diameter for each catalyst determined by H_2 chemisorption

	Pt metal surface area (m^2 g^{-1})	Crystallite diameter [a] (nm)
Pt/Sn-MFI	0.18	7.9
Pt/silicalite-1	0.15	9.5
Pt/Sn-BEA	0.21	6.6
Pt/TiO_2	0.22	6.4
Pt/AC [b]	6.01	0.8

[a] Assumption of spherical crystallites. [b] Supplied from Sigma Aldrich.

Table 3.2 shows the activities and selectivities of aerobic glycerol oxidation at 0.62 MPa of O_2 and 100 °C on the bifunctional catalysts prepared in this work. Pt/Sn-MFI catalyzed glycerol oxidation to LA with an activity of 1.95 h^{-1} and 80.5% selectivity to LA at 89.8% conversion of glycerol. To the best of our knowledge, it is the highest yield of LA achieved using heterogeneous catalysts in the absence of a base. Concentration profiles of reactants and various products as well as the selectivity to LA are shown in Figure 3.3. At the beginning of the reaction, the main product is DHA formed by the oxidation of the secondary hydroxyl group of glycerol and the isomerization of GLA. GLA was also detected in the reaction with a low selectivity. With increasing glycerol conversion, the DHA concentration decreased concurrently with an increase in the selectivity to LA, suggesting that DHA is an intermediate in the formation of LA. When the glycerol conversion is higher than 90%, the LA selectivity began to decrease with the formation of pyruvic acid (PyA) and acetic acid (AA) which is due to further oxidation of the produced LA.[104] The reaction pathways were studied by starting the reactions from LA and PyA on the Pt/Sn-MFI catalyst, respectively (Table 3.2). It was found that PyA is

selectively converted into AA. LA oxidation produced PyA and AA at a reaction rate slower than PyA oxidation under the same reaction conditions. Moreover, as shown in Table 3.2, the TOF value for the oxidation of LA is 39 times lower than that for the oxidation of glycerol, which allows us to optimize the reaction conditions to achieve a high selectivity to LA. Other by-products formed during the course of the reaction were glyceric acid (GlyA) and tartronic acid (TarA), which are formed by the sequential oxidation of GLA.[104, 105] The overall carbon balance obtained from the analyses is above 94%.

Table 3.2 Oxidation of glycerol and other substrates on the catalysts synthesized in the study[a]

Catalyst	Substrate	TOF[b] (s^{-1})	Conv.[c] (%)	Selectivity (%)							
				DHA	GLA	PA	LA	PyA	AA	GlyA	TarA
Pt/Sn-MFI	Glycerol	1.95	89.8	0.9	0.6	4.4	80.5	1.6	2.1	8.7	0.8
Pt/Sn-MFI[d]	LA	0.05[d]	4.7					40.4	46.8		
Pt/Sn-MFI[d]	PyA	0.23[d]	22.5						94.7		
Pt/Sn-BEA[e]	Glycerol	2.33	93.4	6.2	4.9	29.8	28.1	1.0	3.7	18.4	3.0
Pt/silicalite-1	Glycerol	1.11	83.8	9.7	42.0	0.0	0.0	0.0	5.4	32.7	4.2
Pt/AC + Sn-MFI	Glycerol	0.07	53.6	0.0	0.0	0.0	80.8	0.0	0.9	7.8	0.9
Pt/TiO_2	Glycerol	2.21	92.3	3.6	18.6	0.0	0.0	0.0	5.9	55.4	7.8

[a] Reaction conditions: 0.2 M substrate in H_2O; substrate/Pt (mol mol^{-1}) = 350; substrate/Sn (mol mol^{-1}) = 226; pO_2 = 0.62 MPa; 100 °C; 24 h. [b] TOF = moles of a converted substrate divided by moles of $Pt_{surface}$ per reaction time; 0.5 h. [c] Substrate conversion. [d] Reaction time: 4 h. [e] Substrate/Sn (mol mol^{-1}) = 211.

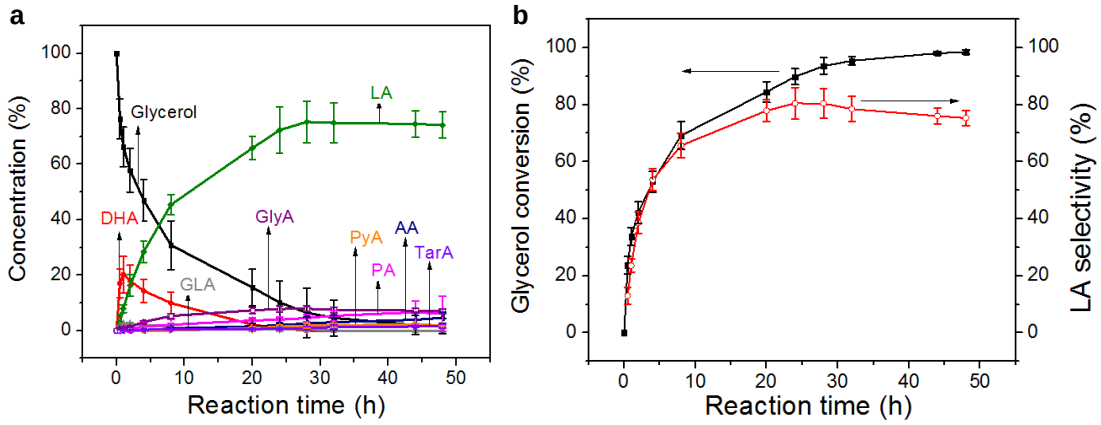

Figure 3.3 (a) Concentration profiles and (b) glycerol conversion and LA selectivity over Pt/Sn-MFI. Reaction conditions are as follows: 0.2 M glycerol in H_2O; glycerol/Pt (mol mol^{-1}) = 350; glycerol/Sn (mol mol^{-1}) = 226; pO_2 = 0.62 MPa; 100 °C. The error bars in the figures are from three repeated reactions.

Although previous studies have suggested that Sn-BEA is a highly active Lewis acid catalyst for the isomerization of triose sugars in the aqueous phase,[1, 50, 51, 59] the Pt/Sn-BEA catalyst provided much lower selectivity to LA (28.1%) compared with Pt/Sn-MFI (Table 3.2). 29.8% selectivity to PA was observed at 93.4% conversion of glycerol, implying that the catalytic activity of the Pt/Sn-BEA catalyst is substantially lower than Pt/Sn-MFI for converting triose sugars into LA. Moreover, a large amount of GlyA was detected at the end of the reaction, indicating that the sequential oxidation of GLA significantly proceeded. To further understand the difference between the Pt/Sn-BEA and Pt/Sn-MFI catalysts, we studied the performance of these catalysts in the conversion of PA to LA. The reactions were first carried out over the Sn-BEA and Sn-MFI catalysts without Pt. Although the BEA zeolite with 12-membered-ring has larger pore sizes than MFI with 10-membered-ring (Table 3.3), Sn-MFI displays a 45% higher yield of

LA than Sn-BEA (Figure 3.4). The higher catalytic activity of Sn-MFI for PA conversion in water might be due to its relative hydrophilic surface compared with the Sn-BEA catalyst. It has been known that zeolites synthesized in fluoride medium contain fewer structural defects and silanol groups than the ones synthesized in caustic medium.[68, 106] In this study, the Sn-MFI catalyst was synthesized using a conventional approach without using fluoride ions. In contrast, hydrofluoric acid (HF) had to be used in the synthesis of the Sn-BEA catalyst. The smaller amounts of defects and silanol groups in the Sn-BEA provide a more hydrophobic environment for the catalyst as shown in the previous literature.[106, 107] This observation is also evidenced by FT-IR spectra of the samples in the OH stretch range of 3800 – 3000 cm^{-1} (Figure 3.5). It is believed that different hydrophobic/hydrophilic properties of the two catalysts may affect their adsorption and catalytic performances. Higher catalytic activity of Sn-MFI in the reaction of PA to LA should be due to the synergism between the structure of Lewis acid Sn sites and adsorption properties. After Pt nanoparticles were loaded, the catalytic activity of both catalysts decreased as listed in Table 3.4. In the case of loading Pt onto Sn-MFI, the reaction rate decreased by around 5.5%. The effect of loading Pt on the catalytic activity of Sn-BEA was more obvious and 41.5% decrease was observed. Overall, Pt/Sn-MFI provided a 2.3 times higher initial reaction rate than Pt/Sn-BEA for the conversion of PA to LA. This indicates that the loading of Pt might partially block the Lewis acid Sn sites in these two catalysts. Corma et al. reported that the Sn framework in the Sn-BEA sample can stabilize the nucleation of Pt nanoparticles inside the zeolite channels and form Pt^0–Sn^{4+} sites.[108] We believe that a part of Pt precursors ($H_2PtCl_6 \cdot 6H_2O$) used in our synthesis

can diffuse into the zeolite BEA channels because of the large pore size of the BEA structure. The Pt^0–Sn^{4+} sites might not be able to catalyze the reaction of PA to LA. In addition, the Pt nanoparticles within the zeolite channels could also block diffusion pathways of the chemicals involved in the reactions. In contrast, it is more difficult for the Pt precursors to diffuse into the MFI structure due to a smaller pore size. The activity of the Sn sites in Sn-MFI was affected by the loading of Pt to a lesser extent. As a result, the remarkable catalytic performance of Pt/Sn-MFI in the studied reactions can be attributed to the accessible Sn site, open framework structure and hydrophilic surface.

Table 3.3 Textural information from N_2 adsorption-desorption isotherms

	BET surface area [a] ($m^2\ g^{-1}$)	Micropore volume [b] ($cm^3\ g^{-1}$)	Total pore volume [c] ($cm^3\ g^{-1}$)
Sn-MFI	386	0.12	0.29
Pt/Sn-MFI	347	0.12	0.23
Sn-BEA	511	0.19	0.38
Pt/Sn-BEA	454	0.19	0.27
Pt/silicalite-1	353	0.11	0.34
Pt/TiO_2	38	0	0.31
Pt/AC	1375	0.10	1.20

[a] Calculated from P/P_o range of 0.05 - 0.25 using BET equation. [b] Calculated by the t-plot method. [c] Calculated from the amount adsorbed at P/P_o = 0.975.

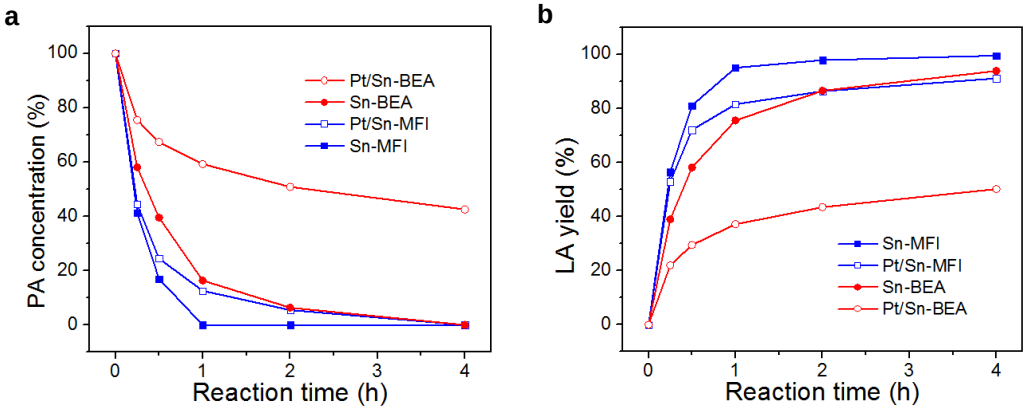

Figure 3.4 Reaction profiles for (a) the conversion of PA into LA and (b) LA yield over Pt/Sn-MFI, Sn-MFI, Pt/Sn-BEA and Sn-BEA catalysts. Reaction conditions are as follows: 0.2 M PA in H_2O, PA/Sn (mol mol^{-1}) = 226; 100 °C; batch reactor.

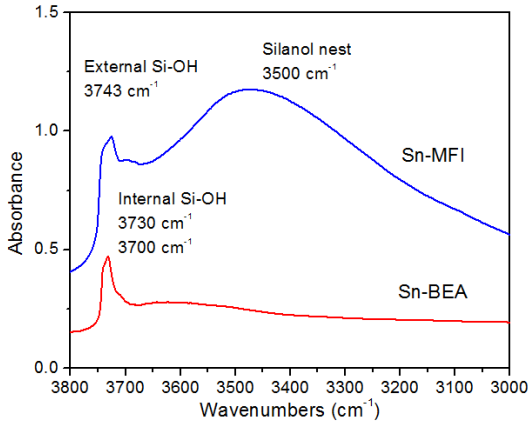

Figure 3.5 FT-IR spectra in the OH-stretch region (3800 - 3000 cm^{-1}) of Sn-MFI and Sn-BEA zeolites.

Table 3.4 TOF values for the conversion of PA into LA[a]

	Sn-MFI	Pt/Sn-MFI	Sn-BEA	Pt/Sn-BEA
TOF (h^{-1})[b]	522	493	372	218

[a] Reaction conditions: 0.2 M PA in H_2O; PA/Sn (mol/mol) = 226; 100 °C; batch reactor. [b] TOF = moles of converted PA divided by moles of Sn per reaction time (h); 15 min.

To understand the reaction pathway and mechanism for the conversion of glycerol into LA over the bifunctional catalysts, additional control experiments were

performed. It was found that glycerol reaction does not occur at all on Sn-MFI and Sn-BEA catalysts in the absence of Pt. On the other hand, Pt on siliceous MFI, Pt/silicalite-1, catalyzed the oxidation of glycerol predominantly to GLA (42.0%) and GlyA (32.7%, Table 3.2). The fact that PA and LA were not formed in the absence of either a Lewis acid or Pt suggests that the combination of a selective oxidation catalyst and an isomerization catalyst is indispensable for the tandem reaction pathway. Interestingly, oxidation of glycerol over Pt/silicalite-1 mainly produced GLA and GlyA, not DHA. This result clearly indicates that Pt prefers to catalyze the oxidation of the primary hydroxyl group of glycerol to produce GLA. DHA, a thermodynamically stable isomer of GLA, is formed over the Lewis acid sites of the Pt/Sn-MFI catalyst. This finding is consistent with previous reports.[58, 109, 110] The subsequent reaction of DHA to LA also occurs over the Lewis acid catalyst. A physical mixture of Pt catalysts supported on activated carbon (Pt/AC, 5 wt% Pt, Sigma Aldrich) and Sn-MFI was also examined for this reaction (Figure 3.6). The catalytic activity of the mixture (TOF = 0.07 s^{-1}) is much lower than the Pt/Sn-MFI catalyst (TOF = 1.95 s^{-1}) even though the surface area of Pt on AC is much larger than that of Pt on Sn-MFI (Table 3.1). After 20 h, the LA selectivity from the physically mixed catalysts exceeded 80%, which is similar to that from Pt/Sn-MFI. However, the Pt/AC catalyst was deactivated obviously faster than the Pt/Sn-MFI and was only able to convert 54% of glycerol over 24 h. It has been known that TiO_2 is also an active Lewis acid catalyst.[111] Au/TiO_2, Pt/TiO_2 and $Au–Pt/TiO_2$ have been used for glycerol oxidation in the presence of NaOH.[93] Under the reaction conditions in this study, the Pt/TiO_2 catalyst could not produce any LA due to the weak Lewis acidity, and the main products

were GLA, GlyA and TarA (Table 3.2). The catalytic performance of Pt/TiO_2 is similar to Pt/silicalite-1, indicating that the Lewis acidity of TiO_2 is not capable of activating the functional groups of the intermediates, GLA and DHA, under the reaction conditions. On the basis of the results, it can be concluded that Sn-MFI acts not only as a Lewis acid catalyst but also as a superior support for the Pt catalyst as compared with the activated carbon and TiO_2.

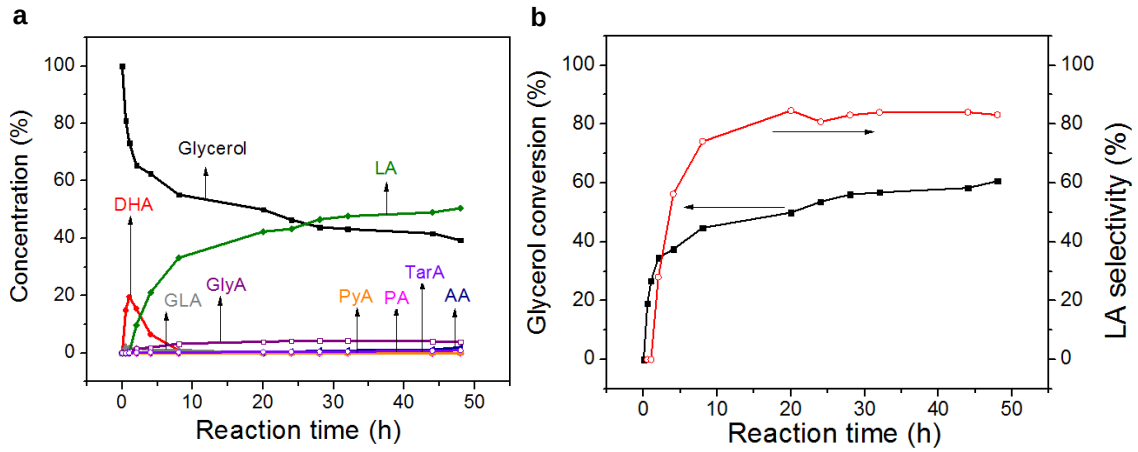

Figure 3.6 (a) Concentration profile and (b) glycerol conversion and LA selectivity over a physical mixture of Pt/AC and Sn-MFI. Reaction conditions: 0.2 M glycerol in H_2O; glycerol/Pt (mol/mol) =350; glycerol/Sn (mol/mol) = 226; *p*O2 = 0.62 MPa; 100 °C.

Based on these reaction results, a tandem reaction pathway for selective oxidation of glycerol to LA is proposed in Scheme 3.2. In a base-free environment, Pt nanoparticles predominantly activate the primary hydroxyl group over the secondary one in glycerol, leading to the formation of GLA. The formed GLA can undergo sequential oxidations to GlyA and TarA. In the presence of the Lewis acid Sn-MFI catalyst, GLA is quickly converted into a thermodynamically more stable isomer, DHA, via intramolecular 1,2 hydride shift reaction.[58, 109, 110] Previous studies have reported that

weak Brønsted acid catalyzed dehydration of DHA produces PA.[58, 112] The formed PA undergoes another intramolecular 1,2 hydride shift after hydration of PA, to generate LA. The superior catalytic activity of Sn-MFI can facilitate the reaction of GLA to LA even if the competitive sequential oxidations of GLA can also occur. Moreover, further oxidation of LA on the catalyst is 39 times slower than oxidation of glycerol, which favors a cascade reaction stopping at LA.

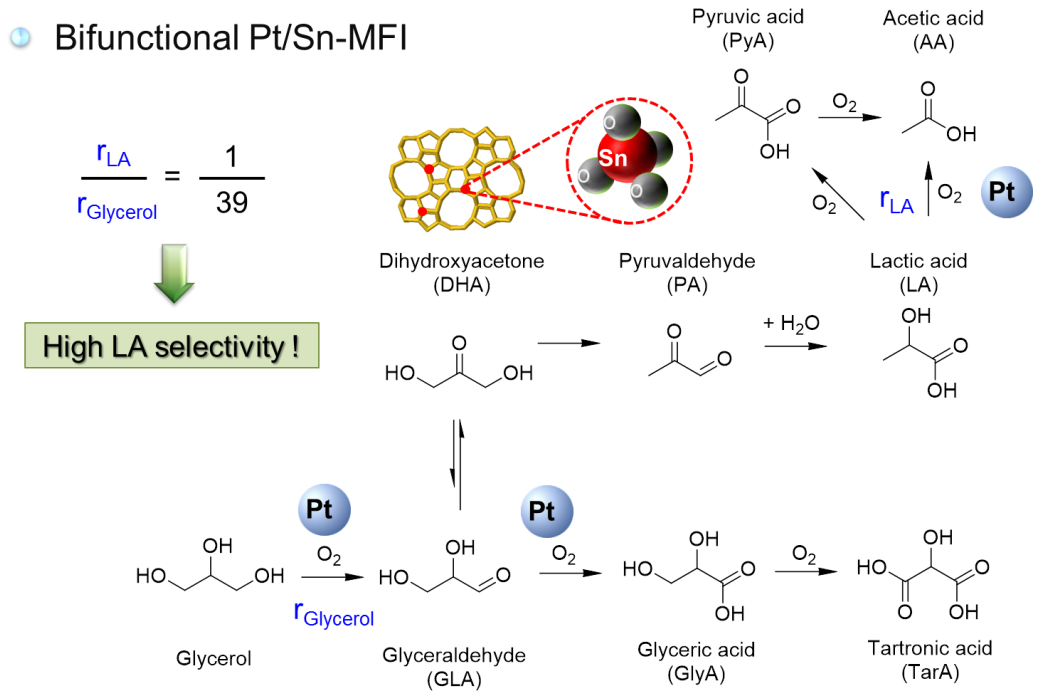

Scheme 3.2 Proposed reaction pathways for the selective oxidation of glycerol to LA over the Pt/Sn-MFI catalyst.

The spent catalysts were regenerated by washing with deionized water, ethanol and acetone at room temperature. Unfortunately, a gradual decrease in catalyst activity was observed for the recycled catalysts (Figure 3.7). This trend has also been shown

over Pt/TiO_2 catalyst for conversion of glycerol into lactate in the presence of base.[113] Further improvement on the reusability of the catalysts will be able to be achieved by using bimetallic Au–Pt on Sn-MFI catalyst, which is an on-going project in our group.

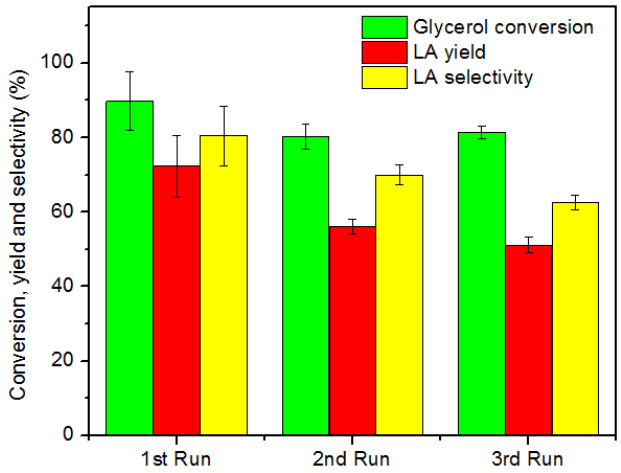

Figure 3.7 Recycling of Pt/Sn-MFI catalyst after 24 h of reaction. Reaction conditions are as follows: 0.2 M glycerol in H_2O; glycerol/Pt (mol mol^{-1}) = 350; glycerol/Sn (mol mol^{-1}) = 226; pO_2 = 0.62 MPa; 100 °C.

CHAPTER 4

MORPHOLOGY-TUNABLE LEWIS ACID SN-BEA WITH HYDROPHOBICITY FOR CELLULOSIC SUGAR ISOMERIZATIONS

4.1 Introduction

Lewis acid Sn-BEA, a molecular sieve with BEA topology containing tetrahedrally coordinated Sn, has been demonstrated to be a promising heterogeneous solid catalyst for the Baeyer-Villiger (BV) reaction,[43-45] reduction of carbonyl compounds with secondary alcohols through the Meerwein-Ponndorf-Verley (MPV) reaction,[41-43] ring-opening hydration of epoxides,[114] Diels-Alder and dehydration reaction pathway for producing *p*-xylene from 2,5-dimethylfuran and ethylene,[21, 22, 115-119] and the isomerization of cellulosic sugars.[38-40, 50, 106, 120, 121]

The outstanding catalytic activity and selectivity of Sn-BEA are attributable to the Lewis acidity coming from isolated Sn atoms in zeolite framework and hydrophobic nature associated with a defect-free siliceous surface.[1, 40, 48, 50, 51] This hydrophobic property arises from the use of hydrofluoric acid (HF) in the synthesis of Sn-BEA. Fluoride ions not only act as a mineralizing agent for silica sources, but also pair with the positive charges of organic structure-directing agents (OSDA), i.e., tetraethylammonium (TEA^+). Therefore, the fluoride-assisted synthesis can produce highly crystalline zeolites with low density of structural defects (silanol groups, Si-OH) compared with the zeolites synthesized using hydroxide ions (OH^-) in caustic media. The application of HF-mediated Sn-BEA, however, encounters several obstacles. For example, Sn-BEA synthesized under

HF media usually possesses large micrometer sized crystals due to slow crystallization.[122-124] It is difficult to control crystal morphology using this method (e.g., nanocrystalline Sn-BEA and mesoporous Sn-BEA). The mass transfer limitation imposed by the large crystal size of Sn-BEA can hinder its catalytic applications, in particular, when bulky reactants or products are involved. Furthermore, the use of HF in a material manufacturing process is strictly limited by safety regulation that can prevent the potential commercialization of this catalyst.

Recently, alternative synthesis approaches such as dry gel conversion (DGC) and post-synthetic methods have been developed for Sn-BEA.[125-131] In particular, the post-synthetic methods have been extensively studied, due to the simplicity of the method. Li and coworkers revealed that Sn can be grafted onto dealuminated zeolite BEA via chemical vapor deposition with tin chloride ($SnCl_4$) vapor.[129] According to Hammond et al., a solid state ion-exchange (SSIE) route was proposed by mixing tin acetate with dealuminated BEA.[127, 128] Dijkmans et al. employed a solution-based approach to incorporate Sn into dealuminated BEA.[130, 131] These post-synthetic methods include an acid treatment to remove framework Al from the parent Al-containing zeolites, creating silanol (Si-OH) nests at the removed Al sites. Reacting various Sn sources with silanol nests generated by the dealumination leads to the formation of tetrahedrally coordinated Sn sites. This protocol makes it possible to tailor the Sn content of Sn-BEA by changing the amount of Sn source and allows Sn-BEA to possess various morphologies. Nevertheless, the defect density in the post-synthesized Sn-BEA samples is high, likely because of the low mobility of Sn sources in the treatment and the little

control over the type and amount of silanol groups in dealuminated BEA. Therefore, the post-synthesized Sn-BEA showed much lower catalytic performances in a hydrophilic solvent than the conventional hydrophobic Sn-BEA made in the presence of HF.[106, 126, 132] It is a challenge to synthesize low defective Lewis acid Sn-BEA of varying crystal morphologies. Herein, we demonstrate that morphology-tunable Sn-BEA crystals with low defects can be readily achieved by a crystallization method.

Recrystallization techniques have been used to prepare hollow structured zeolites through a concerted process including dissolution of crystalline zeolites and reassembly for recrystallization.[133-138] The dissolution of parent zeolites was achieved using a basic solution. Meanwhile, the recrystallization of dissolved species was assisted with the use of an OSDA. Hollow MFI zeolites such as silicalite-1, ZSM-5 and TS-1 have been synthesized from conventional MFI crystals using tetrapropylammonium hydroxide (TPAOH) as an OSDA.[134-138] In a similar recrystallization treatment, a hollow morphology of SAPO-34 with CHA topology was obtained using tetraethylammonium hydroxide (TEAOH).[133] By tailoring the recrystallization parameters, hierarchical zeolites have also been fabricated by the method.[139-143]

In this study, we modified the recrystallization approach to reduce the defects without changing the morphologies of the parent Sn-BEA samples. Sn atoms were incorporated into the dealuminated BEA via a post-synthetic route, followed by recrystallization of the resultant material with tetraethylammonium bromide (TEABr) as an OSDA and ammonium fluoride (NH_4F). Bulky, 200 nm sized and hierarchical Sn-BEA zeolites with reduced defects were fabricated by this method, respectively. The catalytic

activity of the synthesized Sn-BEA samples was systematically evaluated using the isomerizations of glucose (C_6 sugar) and lactose (C_6 sugar dimer) dissolved in both water and MeOH solvents, respectively.

4.2 Experimental

4.2.1 Material Syntheses

Sn-BEA-HF was synthesized according to the method reported by Chang and coworkers.[101] Typically, 10.47 g of tetraethylorthosilicate (TEOS, 98%, Alfa Aesar) was mixed into 11.51 g of tetraethylammonium hydroxide solution (TEAOH, 35 wt%. Alfa Aesar or SACHEM), and stirred at room temperature until it became homogeneous. To this solution, 0.15 g of tin chloride hydrate ($SnCl_4 \cdot xH_2O$, 34.4 wt% Sn, Alfa Aesar) dissolved in 0.96 g of deionized water was added. The mixture was then stirred in a hood until ethanol generated from the hydrolysis of TEOS was completely evaporated. Then, 0.560 mL of dealuminated zeolite beta seed solution (0.224 g mL^{-1}) was added into the solution (4.1 wt% with respect to the silica content) and mixed by a plastic spatula. Finally, 0.971 mL of hydrofluoric acid (HF, 48 wt%, Alfa Aesar) was added and homogenized by using a plastic spatula. The obtained gel with a molar composition of 1 SiO_2 : 0.008 SnO_2 : 0.27 TEA_2O : 0.54 HF : 7.5 H_2O was then transferred into a Teflon-lined stainless steel autoclave. For crystallization, the autoclave was heated at 140 °C with a rotation of 3 rpm for 4 days. The as-made product was collected by extensive washing with deionized water and then drying in a 100 °C oven overnight. The resulting solid was calcined in tube furnace by flowing air with a ramping rate of 1 °C min^{-1} to

550 °C for 12 h, with the aim to remove the organic structure-directing agent and fluoride ions. The Si/Sn molar ratio of the final product was 126, as determined by inductively coupled plasma (ICP) analysis.

In order to synthesize Sn-BEA-PS, three parent Al-BEA zeolites were prepared: (1) commercial Al-BEA (CP814E, Si/Al=12.5, denoted as Com_Al-BEA) from Zeolyst, (2) Al-BEA with 200 nm of a particle size (denoted as 200nm_Al-BEA) synthesized from earlier literature,[144] and (3) three-dimensionally ordered mesoporous imprinted Al-BEA (denoted as 3DOm_Al-BEA) synthesized by a previously reported method.[34] The prepared Al-BEA zeolites were dealuminated by treatment with nitric acid (HNO_3, 70 wt%, Fisher Scientific). Typically, 0.5 g of the Al-BEA was mixed with 25 mL of HNO_3 in a Teflon-lined stainless steel autoclave which was then put into 80 °C oven for 24 h under static conditions. The dealuminated zeolite BEA (DeAl-BEA) was washed extensively with deionized water, and subsequently dried overnight at 100 °C. To prepare post-synthesized Sn-BEA (Sn-BEA-PS), solid-state incorporation was performed by grinding tin chloride hydrate ($SnCl_4 \cdot xH_2O$, 34.4 wt% Sn, Alfa Aesar) with DeAl-BEA for 10 min in a pestle and mortar, followed by calcination in tube furnace by flowing air with a ramping rate of 1 °C min^{-1} to 550 °C for 12 h.[127] Each Sn-BEA-PS sample *via* post-synthesis was named Com_PS, 200nm_PS and 3DOm_PS, depending on the parent Al-BEA used. All Sn-BEA-PS zeolites possessed a Si/Sn molar ratio of 125, confirmed by ICP analysis.

Sn-BEA-RC was achieved by recrystallizing Sn-BEA-PS in the presence of tetraethylammonium bromide (TEABr, 98%, Alfa Aesar) and ammonium fluoride (NH_4F, 96%, Alfa Aesar). Typically, 0.1 g of Sn-BEA-PS powder was mixed with 0.189 g of TEABr

and 0.034 g of NH_4F for 5 min using a pestle and mortar. The resulting solid with a molar composition of 1 SiO_2 : 0.008 SnO_2 : 0.54 TEABr : 0.54 NH_4F was recrystallized via steam-assisted crystallization (SAC). 0.1 mL of deionized water was dropped into a 50 mL Teflon-lined stainless steel autoclave, and a small glass vial containing the resulting powder was loaded in the autoclave, to avoid direct contact between the solid and water. Subsequently, the autoclave was placed in an oven set at 170 °C, and then heated for 1 day. After recrystallization, the as-made sample was washed by centrifugation with deionized water and dried at 90 °C overnight. The dried sample was calcined in a tube furnace by flowing air with a ramping rate of 1 °C min^{-1} to 550 °C for 12 h, to remove the organic structure-directing agent and the ammonium and fluoride ions. Each Sn-BEA-RC sample prepared by recrystallization was denoted as Com_RC, 200nm_RC and 3DOm_RC, depending on the parent Al-BEA used. All Sn-BEA-RC zeolites possessed a Si/Sn molar ratio of 125, confirmed by ICP analysis.

4.2.2 Material Characterization

Powder X-ray diffraction (XRD) patterns of the samples were measured on an XRD diffractometer (X'Pert Pro, PANalytical) using Cu Kα radiation generated at 45 kV and 40 mA in a 2θ range of 4−40°. A scanning electron microscope (SEM, Magellan 400, FEI) was used to investigate the morphology of the zeolites, and the samples were coated with platinum/palladium alloy prior to observation. Elemental analysis was performed on inductively coupled plasma optical emission spectroscopy (ICP-OES, iCap 6500 Dual view, Thermo Scientific).

Lewis acidity of Sn-BEA zeolites were confirmed by Fourier transform infrared spectroscopy (FT-IR) on an Agilent Cary 660 FT-IR Spectrometer equipped with a MCT detector (128 scans at a spectral resolution of 2 cm^{-1}). Typically, zeolite sample was loaded into a sample cell, followed by annealing at 450 °C for 1 h under vacuum of 0.01 mTorr to completely remove adsorbed water from the sample. After cooling down to 30 °C, the dehydrated solid was saturated with pyridine (99.8%, Sigma-Aldrich) or deuterated acetonitrile (CD_3CN, 99.8%, Sigma-Aldrich). Then, FT-IR spectra were recorded every 10 °C while increasing the cell temperature at a ramp rate of 2.5 °C min^{-1}.

Water adsorption property of Sn-BEA was characterized by thermal gravimetric analysis (TGA) in a thermal analyzer (SDT600, TA instrument). 20 mg of zeolite was mixed with 0.4 mL of water and stirred at 90 °C for 1 h under 1000 rpm, followed by drying at 60 °C in an oven for 16 h. Around 10 mg of the sample was put into the TGA instrument, and the sample temperature was then increased with a ramping rate of 10 °C min^{-1} to 700 °C while flowing helium at 100 mL min^{-1}. Methanol (MeOH) adsorption property of the sample was also determined by the same TGA technique, except sample pretreatment. 20 mg of zeolite was mixed with 0.4 mL of MeOH and stirred at 50 °C for 1 h under 1000 rpm, followed by drying at room temperature for 16 h.

Water vapor adsorption isotherms were obtained using a VSTAR water vapor sorption analyzer (Quantachrome Instruments) at 25 °C. Before measurement, zeolite samples were degassed at 300 °C for 12 h.

4.2.3 Catalytic Activity Test

The catalytic activity of the Sn-BEA zeolites was studied for sugar isomerizations including the conversion of glucose to fructose and conversion of lactose and lactulose in two different solvents i.e., water and MeOH (99.9%, Fischer Scientific). For glucose isomerization in water, 1 g of 1 wt% glucose in water was mixed with Sn-BEA in a closed glass vial. The molar ratio of glucose to Sn was 20. The reaction proceeded at 100 °C for 15 min on an aluminum heating block. For glucose isomerization in MeOH, the reaction occurred at 70 °C for 15 min after 1 g of 1 wt% glucose in MeOH was mixed with Sn-BEA (glucose/Sn molar ratio = 20). After the reaction, the reaction mixture was cooled down in ice water and filtered by a 200 nm syringe filter. The filtrate was then analyzed on HPLC (LC029C Shimadzu) equipped with a refractive index (RI) detector and an HPX-87H column (BioRad) at 30 °C under 0.6 mL min^{-1} of 0.005 M sulfuric acid (Fisher Scientific). In addition, conversion of lactose was performed in both water and MeOH, respectively. The Sn-BEA catalyst was mixed with either 1 g of 1 wt% lactose in water or 1 g of 0.5 wt% lactose in MeOH. The molar ratio of lactose to Sn in the initial reaction mixture was 20 for lactose isomerization in both solvents. The lactose reaction was carried out in water at 110 °C for 2 h, while the reaction occurred in MeOH at 90 °C for 16 h. HPLC (LC029C Shimadzu) was employed to quantify the sugar mixture using a refractive index (RI) detector and an HPX-87C column (BioRad) at 80 °C under 0.6 mL min^{-1} of water (for HPLC, Fisher Scientific).

4.3 Results and Discussions

Sn-BEA-RC samples were synthesized by the recrystallization method, starting from three parent Al-BEA zeolites: bulky Al-BEA (denoted as Com_Al-BEA, Zeolyst, CP814E, Si/Al=12.5), 200 nm sized Al-BEA (denoted as 200nm_Al-BEA) and three-dimensionally ordered mesoporous imprinted Al-BEA (denoted as 3DOm_Al-BEA). For comparison, conventional Sn-BEA was also hydrothermally synthesized using HF, denoted as Sn-BEA-HF (Figure 4.1a). As displayed in Figure 4.2, three Sn-BEA-PS zeolites showed similar morphology to their corresponding parent Al-BEA, indicating no significant change in morphology during the dealumination of Al-BEA and subsequent Sn incorporation into the framework. Moreover, the morphology of Sn-BEA-RC resembles that of their corresponding Sn-BEA-PS although Sn-BEA-RC samples likely have more rough external surfaces than the counterparts**.** This strongly suggests that the recrystallization treatment successfully retained the morphology of the sample.

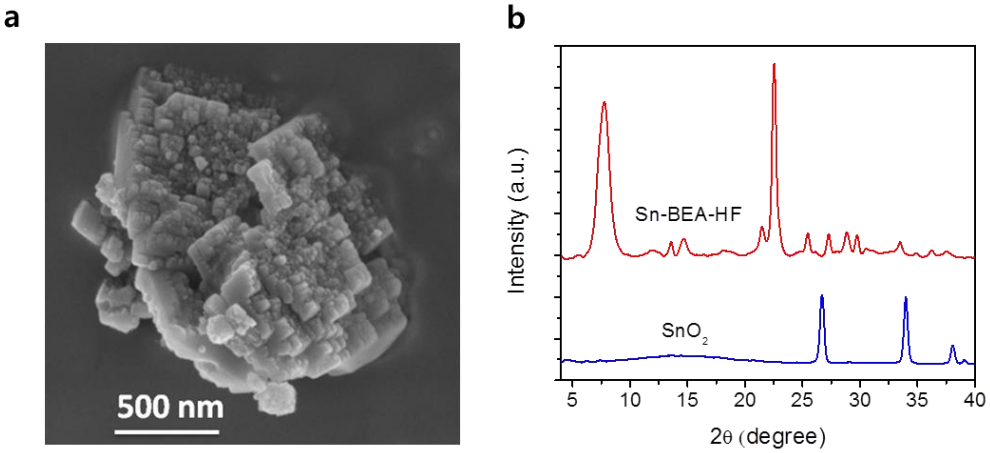

Figure 4.1 (a) A SEM image of Sn-BEA-HF, and (b) XRD patterns of Sn-BEA-HF and SnO_2.

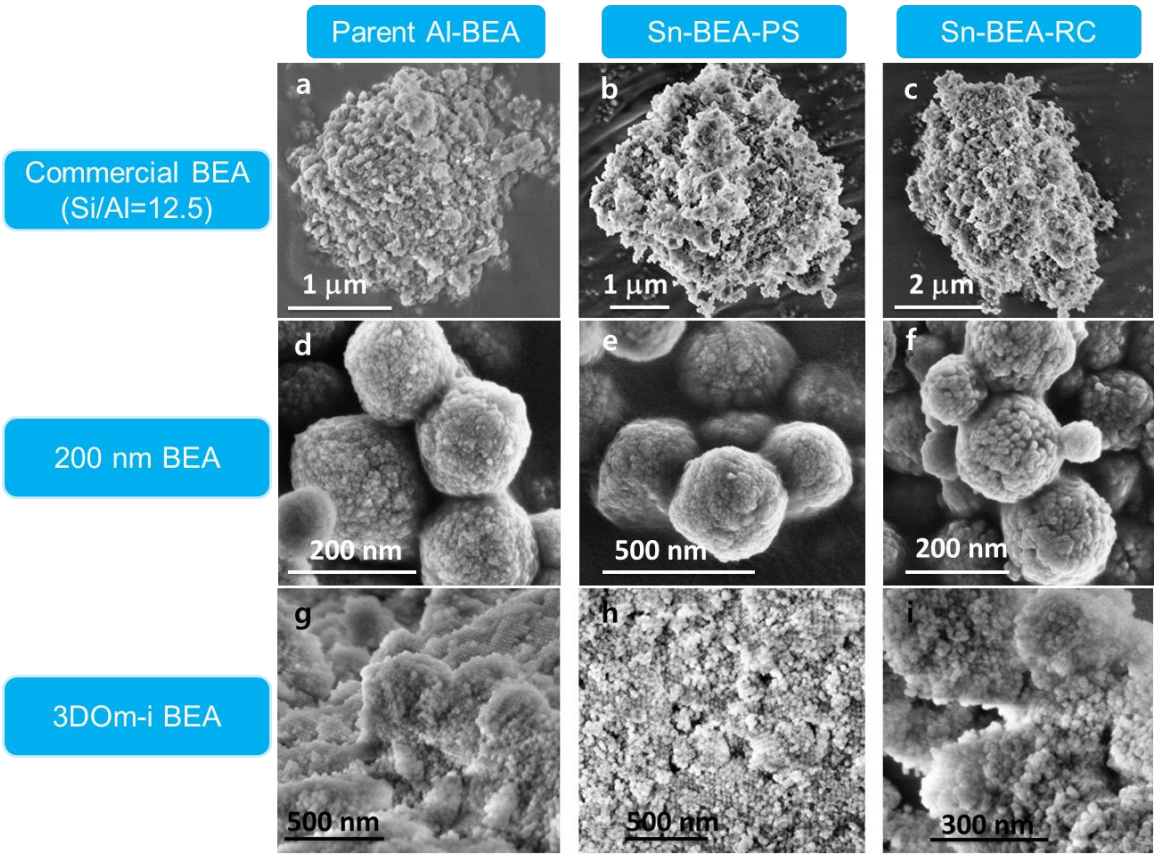

Figure 4.2 SEM images of (a) Com_Al-BEA, (b) Com_PS, (c) Com_RC, (d) 200nm_Al-BEA, (e) 200nm_PS, (f) 200nm_RC, (g) 3DOm_Al-BEA, (h) 3DOm_PS, and (i) 3DOm_RC. The samples were named X_Y. X means the morphologies: Com is for commercial bulky sized, 200nm for 200 nm sized, and 3DOm for three-dimensionally ordered mesoporous imprinted. Y stands for either Al-BEA or Sn-BEA prepared by post-synthesis method (PS) and recrystallization method (RC), respectively.

The crystalline structure of the BEA zeolites was well-preserved during the dealumination and recrystallization processes. The XRD patterns of different parent BEA zeolites, dealuminated and recrystallized samples are displayed in Figure 4.3. All the samples clearly represent two main features at 2θ = 7.5° and 2θ = 22.4°, which are characteristics of typical BEA zeolites with mixed polymorphs.[101, 124, 127] No substantial decrease in intensity was observed for the samples after delaumination and Sn

incorporation, indicating the processes extracted the Al out from the framework structures and did not cause measureable crystal structure change. In addition, no other impurity phase was observed in the samples after the recrystallization. Moreover, Sn-BEA-RC as well as Sn-BEA-PS did not have SnO_2 clusters that show the diffraction peaks at $2\theta = 26.7°$ and $2\theta = 34°$ (Figure 4.1b), pointing to the formation of tetrahedrally coordinated Sn sites into BEA framework.

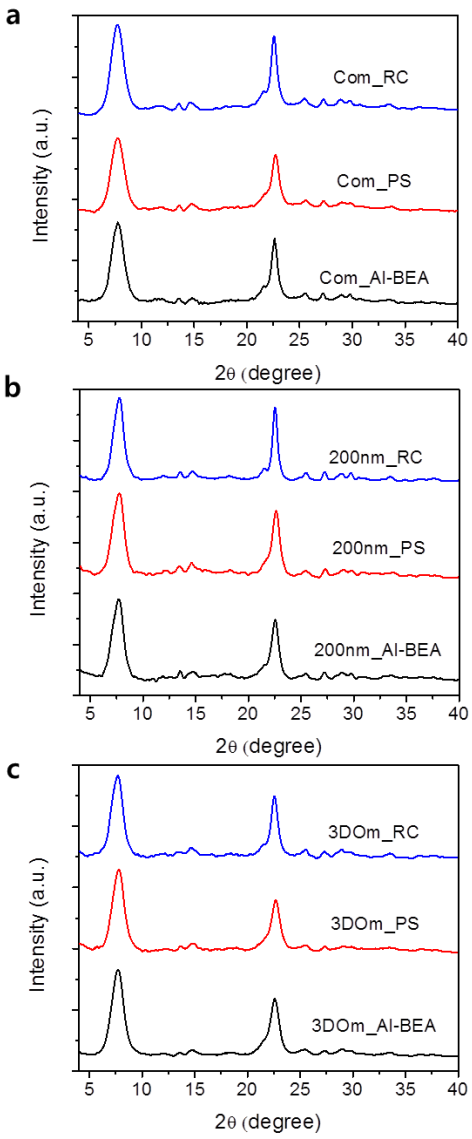

Figure 4.3 XRD patterns of (a) Com_Al-BEA, Com_PS and Com_RC, (b) 200nm_Al-BEA, 200nm_PS and 200nm_RC, and (c) 3DOm_Al-BEA, 3DOm_PS and 3DOm_RC.

The presence of the framework Sn sites in the Sn-BEA samples was confirmed by deuterated acetonitrile (CD_3CN) FT-IR spectroscopy, since this probe molecule exclusively adsorbs on the isolated, tetrahedral Lewis acidic center and distinguishes between framework Sn sites and bulk SnO_2. As highlighted in Figure 4.4a, three main bands were visible in the spectra. The feature at 2276 cm^{-1} is assigned to the ν (C≡N)

stretching mode of acetonitrile adsorbed on the silanol groups (Si-OH).[45, 46] In contrast, two bands at 2310 cm^{-1} and 2316 cm^{-1} could originate from the closed Sn (four-fold coordinated to the siliceous framework) and the open Sn (three-fold coordinated to the zeolite framework with one Sn-OH group) sites, respectively.[51, 56, 125, 128, 145] Sn-BEA-HF possessed more open Sn sites than closed ones, whereas closed Sn sites were more pronounced on Sn-BEA-PS (Figure 4.4a), in good agreement with previous reports.[46, 51, 126, 146] We emphasize that Sn-BEA-RC zeolites likely have more open Sn sites than Sn-BEA-PS samples, indicating that fluoride ions during the recrystallization enhance open Sn environment, a similar role of these anions in a hydrothermal Sn-BEA synthesis. Several efforts have been made so far to investigate the nature of active Lewis acid sites on Sn-BEA materials. Boronat et al. suggested that catalytically active site of Sn-BEA is open Sn species for BV and MPV reactions.[42, 147] In addition, open Sn sites were proposed as the dominant active sites for glucose isomerization.[145, 148, 149] On the other hand, closed Sn sites of Sn-BEA can be catalytically active sites in MPV transfer hydrogenation of 5-hydroxymethylfurfural and various ketones.[146, 150] Therefore, synthesis of Sn-BEA with different ratios of the open and closed sites is critical for controlling their catalytic activities.

The Lewis acidity of the zeolites is further confirmed by FT-IR spectra using pyridine as a probe molecule. Unlike CD_3CN, pyridine used as a base titrant of Lewis acid sites does not distinguish open and closed Lewis acid sites.[114, 118, 145] As shown in Figure 4.4b, Sn-BEA-RC samples exhibited a strong absorption at 1452 cm^{-1}, associated with the pyridine molecules bound with Lewis acidic Sn sites.[52, 58] No significant absorption

signal at 1554 cm^{-1} associated with Brønsted acid was observed in the spectra.[52, 58] Furthermore, inductively coupled plasma (ICP) analysis gave the same Si to Sn molar ratio of 125 for all Sn-BEA-PS and Sn-BEA-RC samples, demonstrating no leaching of Sn atoms was detected in the recrystallization. All the above characterizations clearly indicate that the three Sn-BEA-RC zeolites provide mainly framework coordinated Sn atoms, which are responsible for the Lewis acid sites.

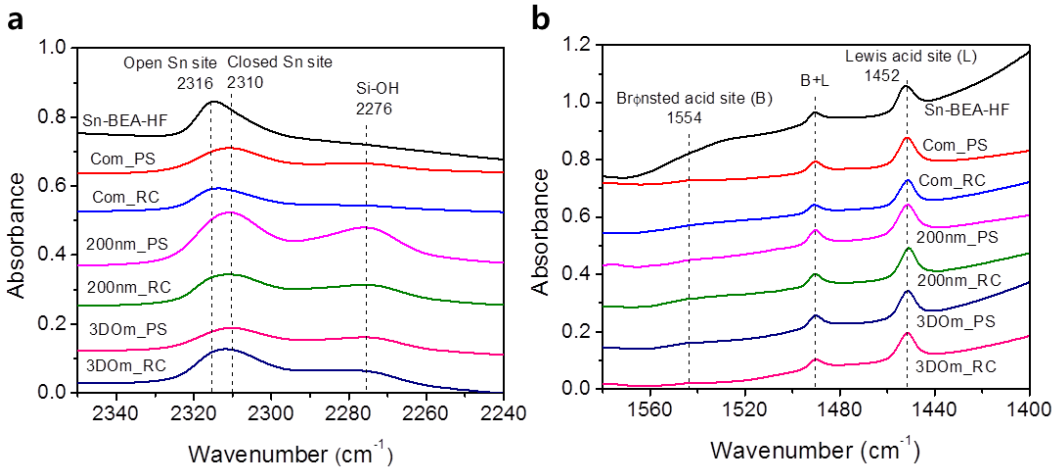

Figure 4.4 FT-IR spectra of Sn-BEA-RC, Sn-BEA-PS and Sn-BEA-HF catalysts using (a) deuterated acetonitrile (CD_3CN) and (b) pyridine as a probe molecule. The spectra were collected after desorbing CD_3CN at 50 °C and pyridine at 200 °C, respectively.

The proposed mechanism of Sn-BEA recrystallization is illustrated in Scheme 4.1. After grinding Sn-BEA-PS with NH_4F and TEABr in a pestle and mortar, the mixture was put into a Teflon-lined stainless steel autoclave, followed by steam-assisted recrystallization at 170 °C for 1 day. Fluoride ions can destroy Si-O-Si bonds on the surface of Sn-BEA-PS to give fragmented silica species. It is very likely that this dissolution occurs on mainly silanol nests on the Sn-BEA-PS. To verify this hypothesis,

we performed FT-IR spectroscopy after removing the adsorbed water from the samples by degassing at 550 °C. In Figure 4.5, the band at 3745 cm^{-1} comes from the isolated silanol groups on the external surface of the samples, whereas the feature at 3735 cm^{-1} is ascribed to the silanol groups located inside the micropores of zeolites.[70, 71] The band around 3500 cm^{-1} corresponds to silanol nests that occur at extended defects.[70] The results of the spectra strongly indicate that the recrystallization route causes significant reduction in mostly silanol nests of all three types of Si-OH groups. In the course of recrystallization process, the presence of TEA ions as an OSDA enables the leached silica fragments to be recrystallized. In this step, TEA cations can pair with fluoride anions, producing fewer silanol defects located in zeolites.[56, 106, 130, 151] For a control experiment, the sole use of NH_4F in the recrystallization resulted in complete collapse of the BEA framework, revealing that TEA ions play an essential role of preserving the crystalline BEA structure (Figure 4.6). In addition, the effect of recrystallization times on the Sn-BEA-RC samples was investigated. From the XRD patterns of Com_RC synthesized with different recrystallization times (Figure 4.6 and Table 4.1), a relative loss in the intensity of the XRD peak at 2θ = 7.5°, compared with the peak at 2θ = 22.4°, was observed on the recrystallized samples with longer recrystallization times such as 4 days and 7 days. This is indicative of the partial collapse of BEA structures, which might be attributed to the decomposition of TEA molecules for long recrystallization times (Figure 4.7 and Table 4.2).

It is believed that the partial dissolution of Sn-BEA-PS and the reassembly of etched silica species occur simultaneously, supported by no pronounced morphological

change during the entire process as shown Figure 4.2. If the dissolution rate by fluoride ions is much faster than the reassembly rate of the etched silica fragments into the zeolite framework, the morphology of Sn-BEA-RC would be quite different from that of Sn-BEA-PS. In this respect, this recrystallization method offers an advantage of tailoring crystal morphology of Sn-BEA that follows that of parent Al-BEA.

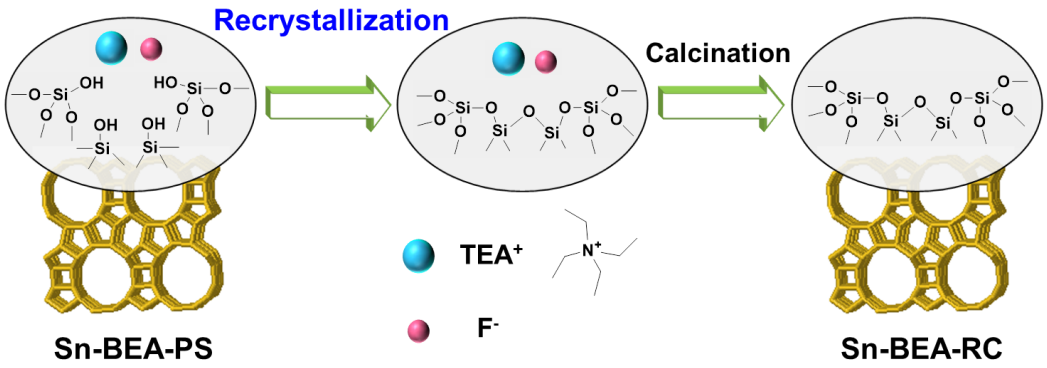

Scheme 4.1 Proposed mechanism of a Sn-BEA recrystallization process.

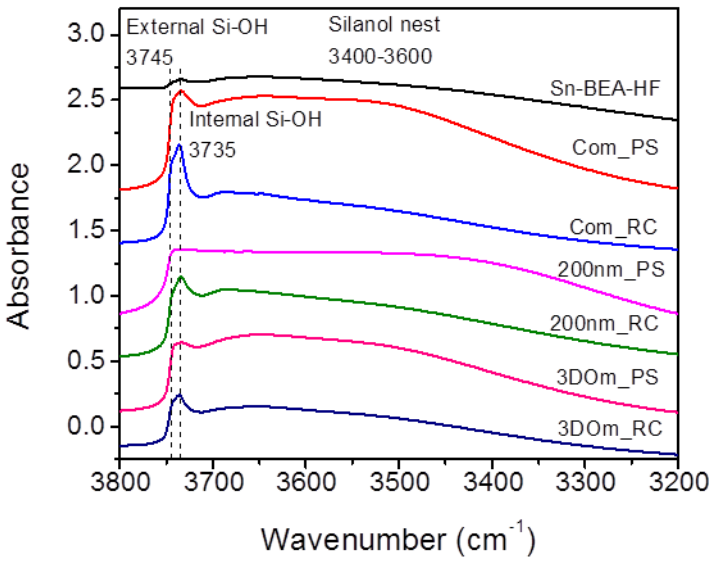

Figure 4.5 FT-IR spectra in the OH-stretch region (3800 – 3000 cm^{-1}) of the Sn-BEA catalysts.

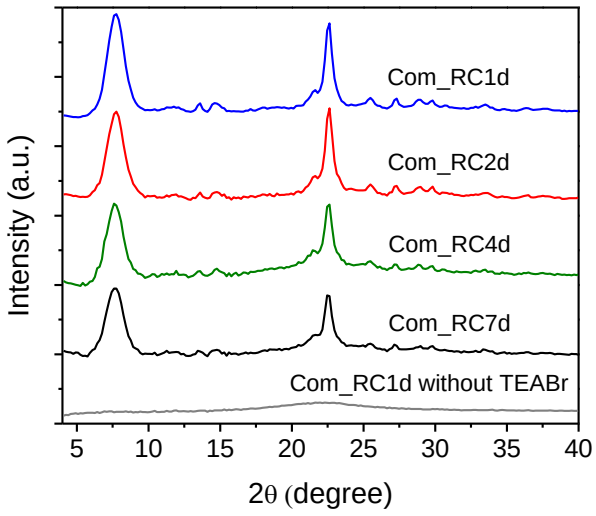

Figure 4.6 XRD patterns of Com_RC synthesized with different recrystallization times (1 day to 7 days) and Com_RC synthesized without TEABr.

Table 4.1 Peak ratio in XRD patterns of Com_RC synthesized with different recrystallization times

Peak ratio[a]	Com_RC1d	Com_RC2d	Com_RC4d	Com_RC7d
Peak area at 2θ = 7.5°/ Peak area at 2θ = 22.4°	1.39	1.38	1.18	1.16

[a] Peak area at 2θ = 7.5° divided by that at 2θ = 22.4° in the XRD patterns as shown in Figure 4.6.

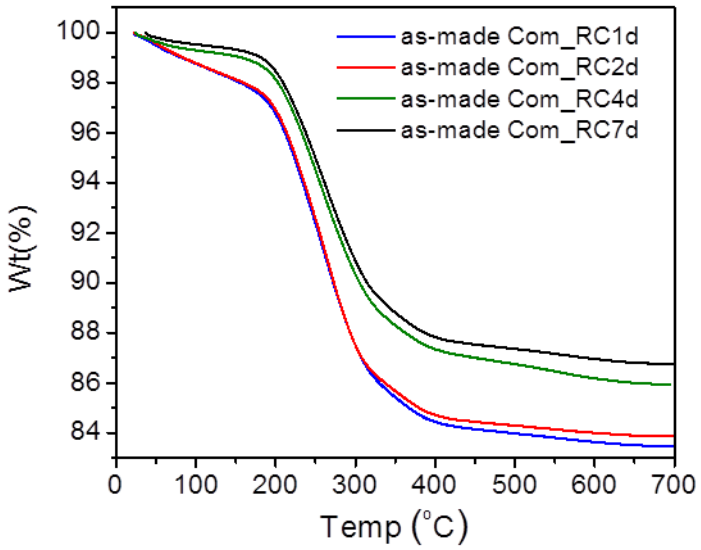

Figure 4.7 TGA curves of as-made Com_RC synthesized with different recrystallization times (1 day to 7 days). The weight decrease on the plot corresponds to the amount of TEA molecules occluded in the zeolite channels during the recrystallization. After recrystallization with specified times, as-made samples were collected by extensively washing with deionized water and drying at 90 °C oven overnight.

Table 4.2 TEA molecules occluded within as-made Com_RC during the recrystallization

Molar ratio[a]	As-made Com_RC1d	As-made Com_RC2d	As-made Com_RC4d	As-made Com_RC7d
TEA (mol)/ Com_RC (mol)	11.6	11.4	9.5	8.9

[a] The molar ratio of TEA molecules (mol) to Com_RC zeolites (mol) in the as-made Com_RC samples.

The three Sn-BEA-RC catalysts were investigated using Lewis acid catalyzed glucose isomerization in water, and compared with Sn-BEA-PS as well as Sn-BEA-HF. Glucose, which is the most abundantly available hexose sugar in cellulose, undergoes isomerization to generate fructose and mannose via an intramolecular 1,2 hydride shift.[39] As shown in Figure 4.8, Sn-BEA-HF produced 29.7% yields of fructose and mannose, whereas the three Sn-BEA-PS samples gave ~7.5% of the products, revealing that the post-synthetic approach reduced the reactivity in accordance with previous literature.[106, 151] This result is mainly because of hydrophilic surrounding coming from the highly defective surface in the vicinity of active Sn sites on Sn-BEA-PS. Notably, Sn-BEA-RC gave rise to ~18.5% yields of the product, which exhibits a 2.5 times higher activity than the Sn-BEA-PS despite the lower activity of Sn-BEA-RC than that of Sn-BEA-HF. It is evident that Sn-BEA-RC is more hydrophobic than Sn-BEA-PS, due to the lower density of silanol defects on Sn-BEA-RC compared with that on Sn-BEA-PS (Figure 4.5). Moreover, as represented in Figure 6, similar initial catalytic activities were observed on the three Sn-BEA-RC as well as the three Sn-BEA-PS for glucose isomerization in water, regardless of the crystal size or mesoporosity of the catalysts. This result suggests that there is no diffusion limitation in the isomerization of glucose over the Sn-BEA catalysts. Besides, we attempted to further improve the catalytic activity of Sn-BEA-RC by varying recrystallization times. Nevertheless, prolonged recrystallization times after 2 days tended to decrease the catalytic performance of Com_RC for the aqueous glucose isomerization (Figure 4.9). This is mainly caused by the lower crystallinity of Com_RC zeolites with longer recrystallization times, as described earlier.

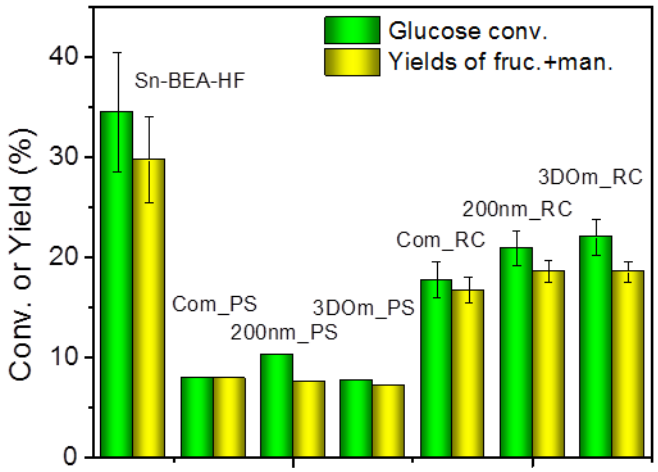

Figure 4.8 Initial catalytic activities of Sn-BEA-HF, Sn-BEA-PS and Sn-BEA-RC for isomerization of aqueous glucose. Reaction conditions are as follows: initial glucose concentration of 1 wt%; a glucose to Sn molar ratio of 20; 100 °C; 15 min.

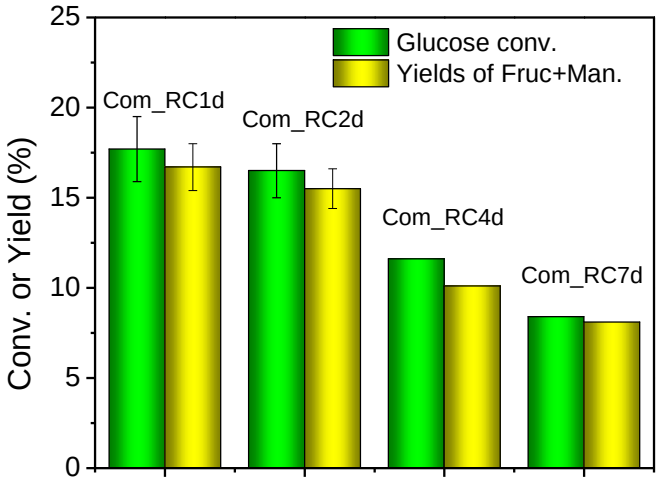

Figure 4.9 Initial catalytic activities of Com_RC with different recrystallization times (1 day to 7 days) for isomerization of aqueous glucose. Reaction conditions are as follows: initial glucose concentration of 1 wt%; a glucose to Sn molar ratio of 20; 100 °C; 15 min.

To better understand the hydrophobic property of the catalyst, water vapor adsorption isotherms were obtained at 25 °C. As displayed in Figure 4.10a, Sn-BEA-HF showed strong hydrophobic characteristics and lower water uptake in the entire range of relative pressure (P/P_o) than Com_RC and Com_PS. This is because of the low defected density of three types of silanol groups (i.e., internal and external Si-OH, and silanol nest) on Sn-BEA-HF derived from fluoride media, as shown in Figure 4.5. Com_RC exhibited a higher uptake of water in comparison with Com_PS, indicating the recrystallization can considerably increase the hydrophobicity of Sn-BEA. It is generally accepted that silica-based materials become more hydrophobic with decreasing numbers of silanol groups.[106, 152, 153]

In addition to the water vapor isotherms, thermogravimetric analysis (TGA) also provided the hydrophilic property of Sn-BEA samples. Water-treated Sn-BEA zeolites were prepared by mixing 20 mg of Sn-BEA with 0.4 mL of water at 90 °C for 1 h, followed by drying at 60 °C oven for 16 h. Upon heating the water-treated Sn-BEA samples, weakly bound physisorbed water disappears immediately (Figure 4.10b), while some more strongly hydrogen-bonded water is gradually released from the sample in the temperature range from ~110 °C to ~400 °C.[154-156] Apparently, the weight loss of Sn-BEA-HF is lower than that of both Com_RC and Com_PS, which is caused by the hydrophobic nature of the Sn-BEA synthesized in the presence of HF. This Com_RC released a lower amount of water than the Com_PS in the temperature range from ~110 °C to ~400 °C, suggesting no strongly hydrogen-bonded water in the Com_RC sample. This can be explained by the reduced silanol defects in the Com_RC.[152, 157] The

desorption above ~400 °C accounting for 1-3 wt% of the zeolite was observed for Com_RC and Com_PS, which is associated with condensation of silanol groups at an onset temperature between 400 °C and 700 °C.[154-156] Therefore, it can be concluded that the recrystallization method indeed improve the hydrophobicity of the Sn-BEA zeolite, however not all silanol defects can be eliminated by this method, which agrees well with the FT-IR spectra in the OH-stretch range (Figure 4.5).

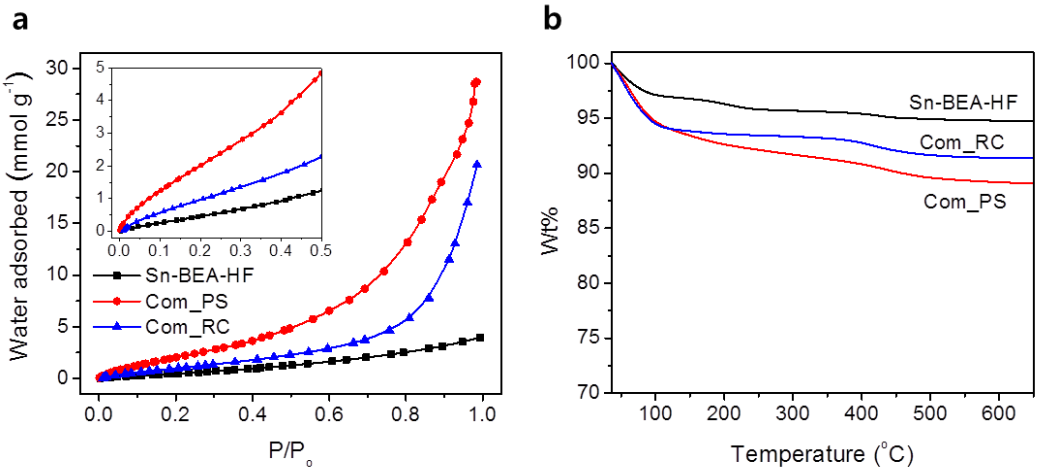

Figure 4.10 (a) Water vapor adsorption isotherms at 25 °C and (b) thermogravimetric analysis (TGA) of water adsorption on Sn-BEA-HF, Com_PS and Com_RC zeolites. Prior to TGA, 20 mg of samples was mixed with 0.4 mL of water and stirred at 90 °C for 1 h under 1000 rpm, followed by drying at 60 °C oven for 16 h.

To gain further insight into the effect of surface properties of the Sn-BEA on its catalytic activity, methanol (MeOH) was chosen as a solvent in glucose isomerization. In this reaction, Lewis acid Sn-BEA catalyzes glucose isomerization to fructose via intramolecular 1,2 hydride shift, which further reacts with MeOH to form methyl fructoside.[158] Three Sn-BEA-RC zeolites produced comparable product yields to Sn-BEA-

HF, and showed 2-fold higher performances than Sn-BEA-PS samples (Figure 4.11). This observation likely arises from the differences in the catalyst surface property and solvent polarity. Since the dielectric constant values are 80 and 32 for water and MeOH, respectively,[159] the presence of a less polar MeOH solvent than water increases MeOH interaction with non-polar siloxane bonds (Si-O-Si) on Sn-BEA.[106, 153] MeOH adsorption property on the catalysts was also evaluated using thermogravimetric analysis. Figure 4.12 clearly shows that Com_RC has similar MeOH uptake to Sn-BEA-HF below ~90 °C of the temperature. Above ~90 °C, however, a lower amount of MeOH was released from Com_RC than Sn-BEA-HF, which might be due to strong interaction of MeOH with hydrophobic non-polar surfaces of Sn-BEA-HF. Although Com_RC has an advantage of catalytic activity regarding the solvent adsorption over Sn-BEA-HF, it should be noted that Com_RC is prone to possessing a lower amount of open Sn sites than the counterpart, confirmed by CD_3CN FT-IR spectra (Figure 4.4a). Because open Sn sites have been found to be dominant active sites for glucose isomerization,[145, 148, 149] there is likely a trade-off between the advantage (i.e., weaker solvent interaction) and disadvantage (i.e., lower open site density) of the Com_RC, in comparison with the Sn-BEA-HF. Moreover, MeOH was highly adsorbed on Com_PS in the whole temperature region, which explains organophilic nature of Com_PS. This is probably because MeOH molecules are able to strongly bind at the silanol nest of Com_PS via hydrogen bonding.[153, 160, 161]

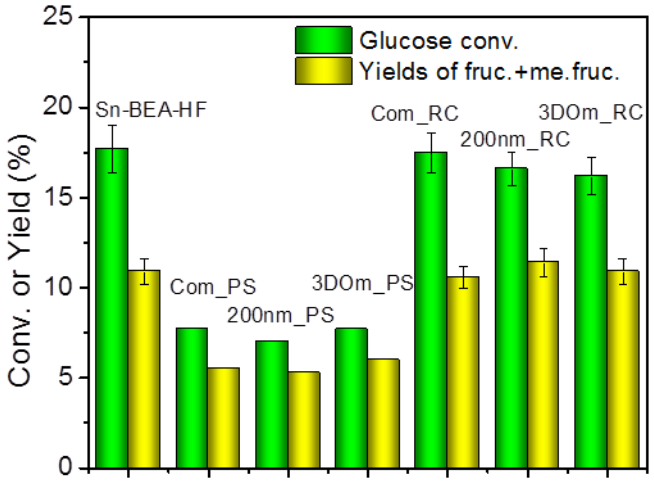

Figure 4.11 Initial catalytic activities of Sn-BEA-HF, Sn-BEA-PS and Sn-BEA-RC for glucose isomerization in MeOH. Reaction conditions are as follows: initial glucose concentration of 1 wt%; a glucose to Sn molar ratio of 20; 70 °C; 15 min.

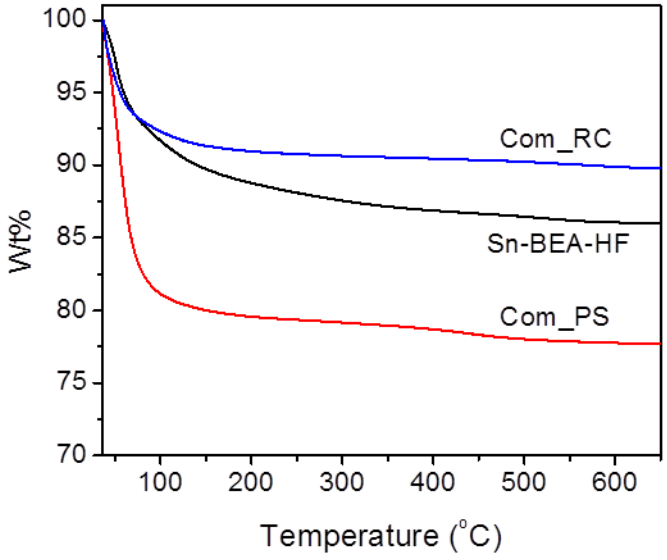

Figure 4.12 Thermogravimetric analysis (TGA) of MeOH adsorption on Sn-BEA-HF, Com_PS and Com_RC zeolites. Prior to TGA, 20 mg of samples was mixed with 0.4 mL of MeOH and stirred at 50 °C for 1 h under 1000 rpm, followed by drying at room temperature for 16 h.

Furthermore, catalytic activities of the Sn-BEA-RC zeolites were explored and compared with other Sn-BEA materials by using a bulky lactose reactant built of galactose and glucose units linked via a β (1-4) glycosidic bond (Scheme 4.2). Lactose serves as a precursor for sugar derivatives such as sugar acids and sugar alcohols in food and pharmaceutical industries.[162] Lewis acid Sn-BEA zeolites convert lactose into lactulose composed of galactose and fructose.[132, 162, 163] In aqueous lactose isomerisation, the three post-synthesized zeolites began to show different catalytic reactivities in the following order: 3DOm_PS > 200nm_PS > Com_PS (Figure 4.13a), demonstrating that Sn-BEA with higher surface area facilitates faster molecular diffusion of lactose to an active site and thus results in a greater catalyst performance. Likewise, Sn-BEA-RC materials performed higher catalytic activities with increasing surface area of the zeolites. Notably, the three RC zeolites produced higher lactulose yields than their corresponding PS ones by factors of 1.8-2.5. As a matter of fact, it is quite challenging for C_{12} lactose molecules to diffuse into the BEA micropores. In this case, molecular diffusion becomes critical for the reaction, giving rise to more pronounced differences in the performances between the hierarchical, 200 nm, and bulky Sn-BEA catalysts. Nevertheless, mesoporous 3DOm_RC and a few micron-sized Sn-BEA-HF catalyzed lactose isomerization to a similar extent. This can be attributable to catalytic inhibition associated with stronger adsorption of water on 3DOm_RC than Sn-BEA-HF whose surface mostly consists of non-polar Si-O-Si bonds. However, when switching solvent from water to MeOH in the isomerization, 3DOm_RC performed the reaction at a 3.2 times higher rate than Sn-BEA-HF (Figure 4.13b). The enhanced reaction rate on

3DOm_RC can be interpreted by the reduced diffusion limitation of lactose within the hierarchically structured catalyst. On the basis of the results, hierarchical Sn-BEA prepared from the recrystallization strategy can achieve high reactivity by tailoring surface property and enhancing open Sn sites as dominant active sites.

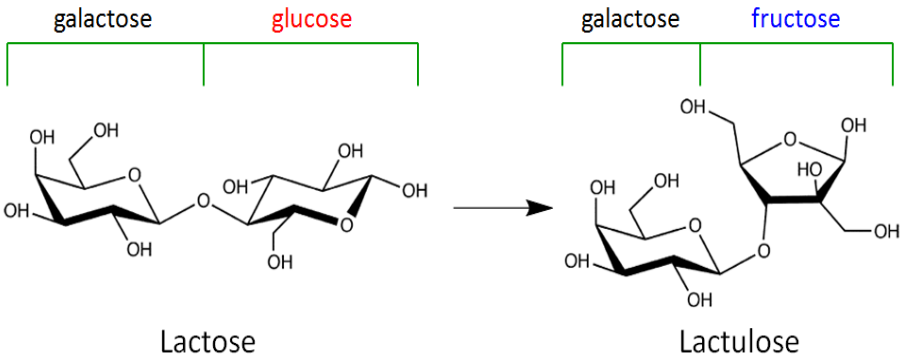

Scheme 4.2 Reaction scheme for the Lewis acid catalyzed isomerization of lactose into lactulose.

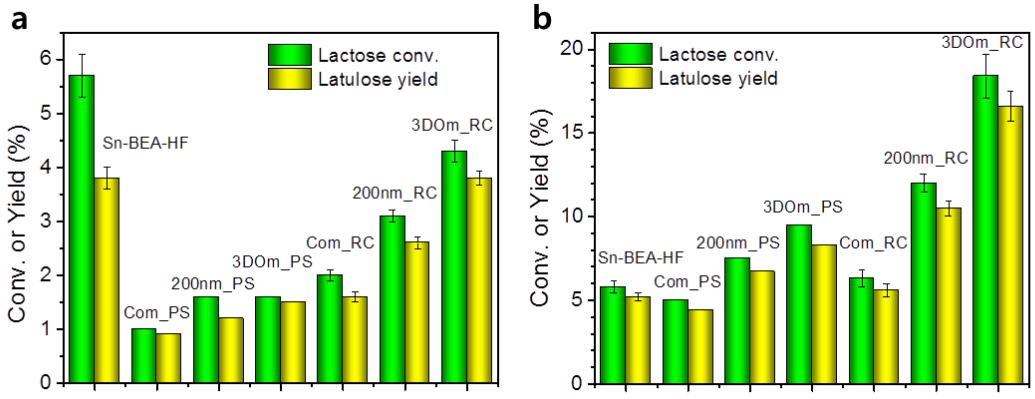

Figure 4.13 Initial catalytic activities of Sn-BEA-HF, Sn-BEA-PS and Sn-BEA-RC for lactose isomerization in (a) water and (b) MeOH solvents, respectively. Reaction conditions are as follows: initial lactose concentration of 1 wt% and 0.5 wt% in water and MeOH, respectively; a substrate to Sn molar ratio of 20; 110 °C at 2 h (in water), and 90 °C at 16 h (in MeOH).

CHAPTER 5

PHOSPHORUS-CONTAINING ZEOLITES FOR RENWABLE P-XYLENE PRODUCTION

5.1 Introduction

p-Xylene is a major commodity chemical and precursor in the production of the most widely used polyester, polyethylene terephthalate (PET). Due to the rapid growth in the global market of PET (6-8% per year),[164] its replacement with a renewable feedstock is a highly desired goal,[165] and there are ongoing research and development efforts to produce *p*-xylene from biomass feedstocks.[115-117, 166-170] Diels–Alder reactions of biomass-derived furans with subsequent dehydration have demonstrated the potential for producing renewable *p*-xylene and other aromatic derivatives with high stereospecificity.[115-117, 166, 167] To date, the most selective catalysts reported are acidic zeolites with large micropores (7.5 Å), which primarily catalyze the dehydration reaction. However, they also catalyze the formation of alkylated and oligomerized by-products (Scheme 5.1).[22] Due to these side reactions, the highest yield to *p*-xylene previously achieved was 75%.[21, 22]

Scheme 5.1 depicts a reaction pathway for *p*-xylene synthesis. The Diels–Alder cycloaddition of DMF and ethylene was carried out, followed, in the same reactor, by the dehydration of the cycloadduct intermediate. This reaction offers a completely renewable pathway for *p*-xylene production since both DMF and ethylene can be obtained from glucose.[85, 171] Increasing the efficiency of the reaction from DMF and ethylene to *p*-xylene is critical for ensuring the economic and technical feasibility for the

entire process. As suggested by a techno-economic analysis on the process of Scheme 5.1, an increase in the yield substantially improves the economics of renewable *p*-xylene.[172]

Conversion of DMF with ethylene to *p*-xylene in *n*-heptane has been demonstrated using acidic zeolite catalysts, including zeolite Y and Al-BEA.[22, 117] There are three competing side reactions: (a) hydrolysis of DMF to form 2,5-hexanedione, (b) multiple additions of ethylene to form alkylated aromatic species, and (c) dimerization of the furan feedstock and/or aromatic products to form oligomers (Scheme 5.1). Density functional theory (DFT) calculations have emphasized the role of Brønsted acids catalyzing the main reaction pathway and enhancing the yield of *p*-xylene by reducing the cycloadduct dehydration barrier from ~60 kcal mol^{-1} to ~10-20 kcal mol^{-1}.[47, 117] However, these Brønsted acid zeolites also catalyze the alkylation and isomerization reactions, which not only reduce *p*-xylene yield but also lead to fast catalyst deactivation.[21] Lewis acid zeolites (e.g., Zr-BEA and Sn-BEA) also catalyze the production of *p*-xylene from DMF with an initial formation rate of *p*-xylene comparable to that of Brønsted acid zeolite, Al-BEA.[21, 115, 116] In particular, Zr-BEA exhibited the highest reported *p*-xylene yield (75%) with much slower deactivation rates. The properties of Zr-BEA were ascribed to the weaker adsorption of DMF and reduced formation of by-products compared with Al-BEA.[21]

Herein, we report that phosphorous-containing siliceous zeolites are highly selective and stable catalysts for this reaction with an unprecedented *p*-xylene yield of 97%. Two phosphorous-containing siliceous zeolites, zeolite Beta (BEA) and self-pillared

pentasil (SPP) zeolite, were investigated, which were known to us to be inactive for alkylation and oligomerization reactions. The P-containing zeolites are not only excellent catalysts for *p*-xylene production but also highly selective, leading to unprecedented high yields.

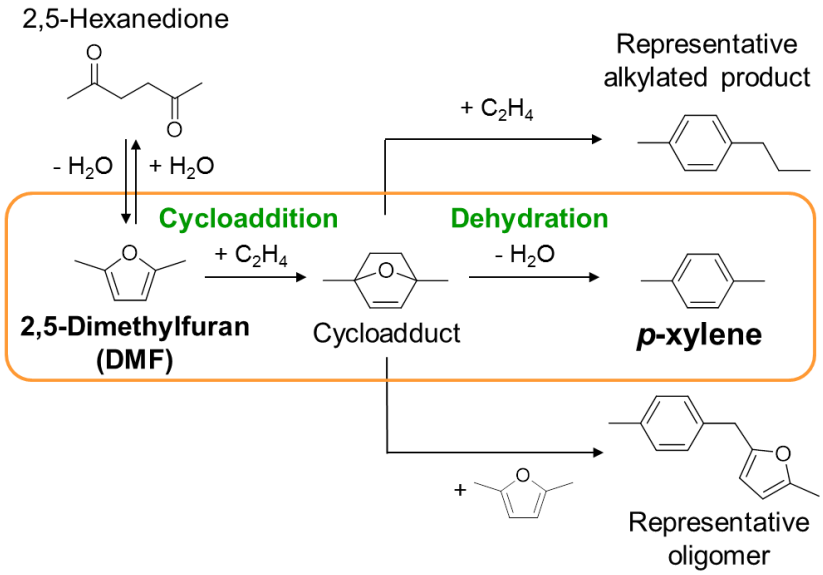

Scheme 5.1 Production of renewable *p*-xylene. The pathway for the synthesis of *p*-xylene from the reaction of DMF with ethylene including major intermediates and by-products is indicated in the highlighted block. The renewable route for the production of DMF from cellulose is also indicated. Renewable ethylene can be commercially produced from ethanol dehydration. It can also be obtained from natural gas or other non-renewable sources.

5.2 Experimental

5.2.1 Material Syntheses

Commercial zeolite Al-BEA (Zeolyst, CP814E, Si/Al = 12.5) was dealuminated by treatment with 70 wt % nitric acid (HNO_3, Fisher Scientific). Typically, 0.5 g of the Al-BEA was mixed with 25 mL of 70 wt % HNO_3 in a Teflon-lined stainless steel autoclave. The

autoclave was then put into an oven at 80 °C for 24 h under static conditions. The dealuminated zeolite BEA (DeAl-BEA) was washed extensively with deionized water and dried overnight at 100 °C. In order to prepare P-BEA with Si/P = 27 (confirmed by ICP analysis), wet impregnation was performed by stirring 0.4 g of DeAl-BEA and 18.2 µL of 85 wt % phosphoric acid (H_3PO_4, Sigma-Aldrich) in 3.33 mL of deionized water. The impregnated sample was dried at 90 °C overnight, followed by calcination in a tube furnace with dry air at 600 °C for 25 min.

P-SPP with Si/P = 27 (confirmed by ICP analysis) was synthesized according to the literature.[27] Typically, tetra(n-butyl) phosphonium hydroxide (TBPOH, 40 wt %, Sigma-Aldrich) as an organic structure-directing agent (OSDA) was added dropwise into tetraethylorthosilicate (TEOS, 98%, Sigma-Aldrich) under stirring. Deionized water was then added to this mixture, and stirred for 24 h. The mixture became a clear sol with a composition of 1 SiO_2 : 0.3 TBPOH : 10 H_2O : 4 EtOH. The sol was sealed in a Teflon-lined stainless steel autoclave and heated for 3 days in an oven at 115 °C. Tetra(n-butyl)ammonium hydroxide solution (TBAOH, 40 wt %, Sigma-Aldrich) can also be used to prepare Si-SPP. After crystallization, the solid product was extensively washed with deionized water by centrifugation and decanting of the supernatant. This process was repeated until the pH of the final supernatant was lower than 9. Subsequently, the collected sample was dried at 90 °C overnight and calcined in a tube furnace at 550 °C for 12 h under dry air.

P-Celite with Si/P = 5.0 (confirmed by ICP analysis) was prepared through an impregnation method.[173, 174] First, the Celite® S (Diatomaceous silica, Sigma-Aldrich) was

calcined at 500 °C for 5 h under air. Then, 1 g of the calcined Celite was ion-exchanged with 100 mL of 0.2 M NH_4NO_3 solution at 60 °C for 20 h. The resulting product was filtered and washed by deionized water thoroughly, followed by drying at 90 °C overnight. The solid was then calcined at 500 °C for 5 h under air. Thereafter, 1 g of the calcined powder was mixed with 4 mL of 0.75 M H_3PO_4 solution, and then dried at 90 °C overnight. The dried mixture was calcined at 500 °C for 5 h under air.

P-Al-BEA was prepared by impregnation of H_3PO_4 on zeolite Al-BEA (Zeolyst, CP814E, Si/Al = 12.5), according to the same procedure described in the preparation of P-BEA, without the dealumination step.

Si-BEA was synthesized following a published method.[175] Typically, 8.72 g of tetraethylammonium hydroxide (TEAOH, 35 wt %, Alfa Aesar or SACHEM) was mixed in 1.24 g of deionized water. To this mixture, tetraethylorthosilicate (TEOS, 98%, Sigma-Aldrich) was added and stirred for 7 h at room temperature. Thereafter, 0.86 g of HF (49%, Alfa Aesar) was added, and the mixture became white solid with a molar composition of 1 SiO_2 : 0.54 TEAOH : 0.54 HF : 7.25 H_2O. The resulting solid was sealed in a Teflon-lined stainless steel autoclave, followed by crystallization for 2 days in an oven at 140 °C. Subsequently, the solid product was extensively washed with deionized water by vacuum filtration. The collected sample was dried at 90 °C overnight and calcined in a tube furnace at 550 °C for 12 h under dry air. Zr-BEA with Si/Zr = 168 (determined by ICP) was synthesized by a seeded-growth method reported earlier.[21] In a typical synthesis, 23.72 g of tetraethylorthosilicate (TEOS, 99%, Alfa Aesar) was added to 27.39 g of tetraethylammonium hydroxide solution (TEAOH, 35 wt %, SACHEM). The mixture was

stirred for 1 h to form a silicate solution. After 0.3 g of zirconium(IV) oxychloride octahydrate ($ZrOCl_2 \cdot 8\ H_2O$, Sigma-Aldrich) was dissolved in 1.92 g water, this solution was added dropwise into the silicate solution. The resulting mixture was stirred in a fume hood until the desired amount of ethanol (generated from TEOS hydrolysis) was evaporated. To this mixture, 1.712 mL of dealuminated zeolite BEA seed suspension with 0.163 g of seed crystal per mL (corresponding to 4.0 wt% seed with respect to silica) was added and mixed by a plastic spatula. Subsequently, 2.36 mL of hydrofluoric acid (HF, 49%, Alfa Aesar) was added and mixed by a plastic spatula to become a hard gel. The final gel with a composition of SiO_2 : 0.008 ZrO_2 : 0.56 TEAOH : 0.56 HF : 7.5 H_2O was transferred to a Teflon lined stainless steel autoclave and crystallized at 140 °C for 4 days under 2 rpm rotation. The solids were extensively washed with deionized water by vacuum filtration, dried in an 80 °C oven overnight, and calcined at 550 °C for 12 h under flowing dry air.

5.2.2 Material Characterization

Powder X-ray diffraction (XRD) patterns of the samples were recorded on an XRD diffractometer (X'Pert Pro, PANalytical) operated at 45 kV of an acceleration voltage and 40 mA of a current using Cu Kα radiation. The data were collected over 4−40° of a 2θ range.

A scanning electron microscope (SEM, Magellan 400, FEI) was used to examine the morphology of catalysts. Prior to the SEM measurement, the samples were coated with platinum/palladium alloy. To take TEM images, aqueous suspensions of the zeolite samples were prepared. TEM specimens were made by placing droplets of the

suspension onto the copper grid coated with ultra-thin carbon film and holey carbon film (Ted Pella Inc.), followed by air-drying at room temperature. TEM imaging was performed using a CCD camera on an FEI Tecnai G^2 F30 TEM operating at 300 kV.

Elemental analysis was performed on inductively coupled plasma optical emission spectroscopy (ICP-OES, iCap 6500 Dual view, Thermo Scientific) in Analytical Geochemistry Lab, Department of Earth Sciences in University of Minnesota. Argon adsorption−desorption isotherms were measured at 87 K by using an automated gas sorption analyzer (Autosorb iQ2, Quantachrome) after the samples were degassed at 300 °C under vacuum.

Catalytically active sites on the catalyst were characterized by pyridine Fourier transform infrared (FT-IR) spectroscopy[56, 176] on an Agilent Cary 660 FT-IR Spectrometer equipped with a MCT detector (128 scans at a spectral resolution of 2 cm^{-1}). The solid sample was heated to 450 °C for 1 h under vacuum of approximately 10^{-5} Pa to completely remove adsorbed water and impurity from the sample. Thereafter, the dehydrated sample was cooled to the desired temperature and then, pyridine (>99%, Sigma-Aldrich) was introduced to the sample cell via the vacuum manifold for 30 min, allowing the sample to be fully saturated with the adsorbate. In the absence of further flowing the pyridine, FT-IR spectra were collected every 10 °C in the process of heating the zeolite at a ramp of 2.5 °C min^{-1}.

Temperature-programmed desorption (TPD) coupled with thermogravimetric analysis (TGA) experiments were carried out, according to earlier literature.[118] The system consists of a Cahn 2000 microbalance mounted within a vacuum chamber at a

base pressure of approximately 10^{-5} Pa. The partial pressures during evacuation were monitored using an SRI quadrupole mass spectrometer (RGA100). The probe molecules of interest were 2-propanamine (99%, Alfa Aesar) and 2,5-hexanedione (97%, Acros Organics). Typically, 50 mg samples were heated under vacuum to 500 °C, prior to performing the adsorption experiments. Subsequently, the samples were saturated with adsorbates of interest at room temperature for 1 h. The TPD-TGA data were collected with 10 °C min^{-1} of a heating rate.

For determination of Brønsted acid sites on Al-BEA (Zeolyst, CP814E, Si/Al = 12.5), 2-Propanamine temperature-programmed desorption (TPD) coupled with thermogravimetric analysis (TGA) experiment was performed. After TPD-TGA data were collected from room temperature to 560 °C, Brønsted-site density was determined by the weight difference between 300 °C and 400 °C which is the temperature range where 2-propanamine decomposes into propene and ammonia on the Brønsted acid sites. As a result, Al-BEA possessed 620 μmol g^{-1}. On the contrary, Lewis acid site density of Zr-BEA came from the metal content of Zr that was quantified by ICP analysis, giving 98 μmol g^{-1} of Lewis acid sites within Zr-BEA.

Solid state ^{31}P-NMR spectra were recorded using a Bruker DSX-500 spectrometer and a Bruker 4 mm MAS probe. The operating frequency is 202.5 MHz for ^{31}P. Powder samples packed into 4 mm zirconia rotors were spun at ambient conditions. For MAS NMR experiments, an rf pulse of 4 μs-π/2 and strong ^{1}H decoupling pulse with two pulse phase modulation (TPPM) were employed for signal averaging of ^{31}P MAS NMR. Chemical shifts were externally referenced to concentrated H_3PO_4 for ^{31}P NMR.

5.2.3 Catalyst Testing for Diels-Alder Cycloaddition and Subsequent Dehydration of 2,5-Dimethylfuran (DMF) with Ethylene

50 mL of 1.35 M DMF (>98%, Alfa Aesar) in *n*-heptane (99%, Alfa Aesar) including 0.08 M *n*-tridecane (>98%, Alfa Aesar, internal standard) was mixed with the catalysts in a bench-top Parr reactor. The reactor was purged with nitrogen at room temperature and then heated to 250 °C by a 4848 temperature control unit (Parr). At 250 °C, ethylene gas (Airgas) with 38 bar partial pressure was introduced into the system, and the reaction was allowed to proceed. During the entire reaction, the total pressure of the reactor was maintained at 62 bar. Time course of the reaction was monitored by taking samples (0.5 mL) for analysis at specified time intervals. The quantitative analysis of the sample was performed by Agilent 6890 gas chromatography (GC) equipped with a flame ionization detector and a Restek RTX-VMS capillary column (30.0 m length, 0.25 mm id, 1.4 µm film thickness). The products, DMF, *p*-xylene (>99%, Sigma-Aldrich) and 2,5-hexanedione were identified by comparing the retention times of each standard chemical, and also cross-checked on a GC-MS system (7890B GC, Agilent). The alkylated products were quantified by using the response factor (RF) for 1-methyl-4-propylbenzene while the oligomer contents were estimated using the additive RF of DMF and *p*-xylene. The concentration of cycloadduct, the intermediate produced from the Diels-Alder reaction of DMF and ethylene, was estimated by using the RF for *p*-xylene, following the previous literature.[21, 22]

5.2.4 Catalyst Removal Test of P-BEA and P-SPP

After 24 h of the reaction of DMF with ethylene at 250 °C, the reaction was stopped by cooling the reactor to room temperature. The spent catalyst was removed from the reaction mixture by centrifugation. 1.35 M DMF was added to this mixture to check if the reaction is heterogeneously catalyzed. The reaction of DMF with ethylene after removing the catalyst from the reactor was carried out using the procedure described above.

5.2.5 Catalyst Reusability of P-BEA and P-SPP

After 24 h of the reaction of DMF with ethylene at 250 °C, the reaction was stopped by cooling the reactor to room temperature. The spent catalyst was separated from the reaction mixture, washed with *n*-heptane 3 times by centrifugation, and dried at 90 °C overnight. The dried solid was calcined in a tube furnace with dry air at 550 °C for 12 h. In order to have the same amount of catalyst in the reactor during the recycling test, 20 wt % of fresh catalyst was mixed with the spent catalyst and used for the reactions.

5.3 Results and Discussions

P-containing zeolite Beta (P-BEA) was prepared using a post-synthetic route, by which P was incorporated within the dealuminated BEA micropores by calcining a phosphoric acid (H_3PO_4) impregnated sample. The synthesis procedure includes first the dealumination of Al-BEA (Zeolyst, CP814E, Si/Al = 12.5) using nitric acid, and second, the impregnation of the dealuminated zeolite BEA with H_3PO_4, followed by the

incorporation of P within the zeolite by calcination. The crystal structure and morphology of the zeolite BEA were preserved after the incorporation of P, as revealed by the XRD patterns of the initial and treated samples in Figure 5.1 and by the SEM/TEM images in Figure 5.2. The micropore volume and BET specific surface area of the zeolite suggest that the high surface area and microporous structure were retained during the P modification step (Figure 5.3 and Table 5.1).

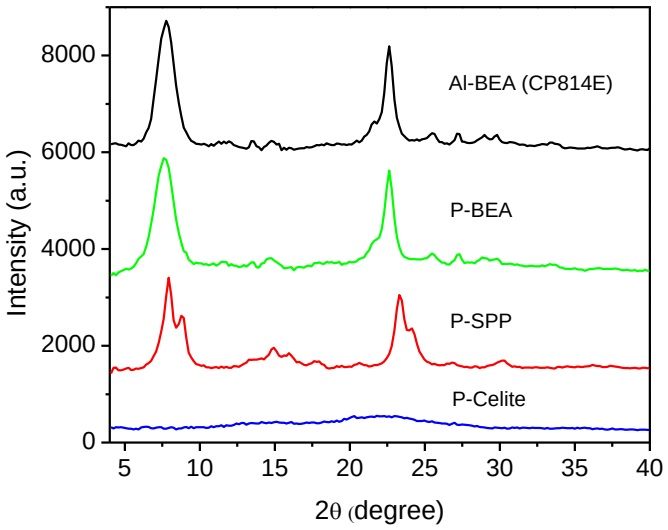

Figure 5.1 XRD patterns of Al-BEA (Zeolyst, CP814E, Si/Al = 12.5), P-BEA, P-SPP and P-Celite.

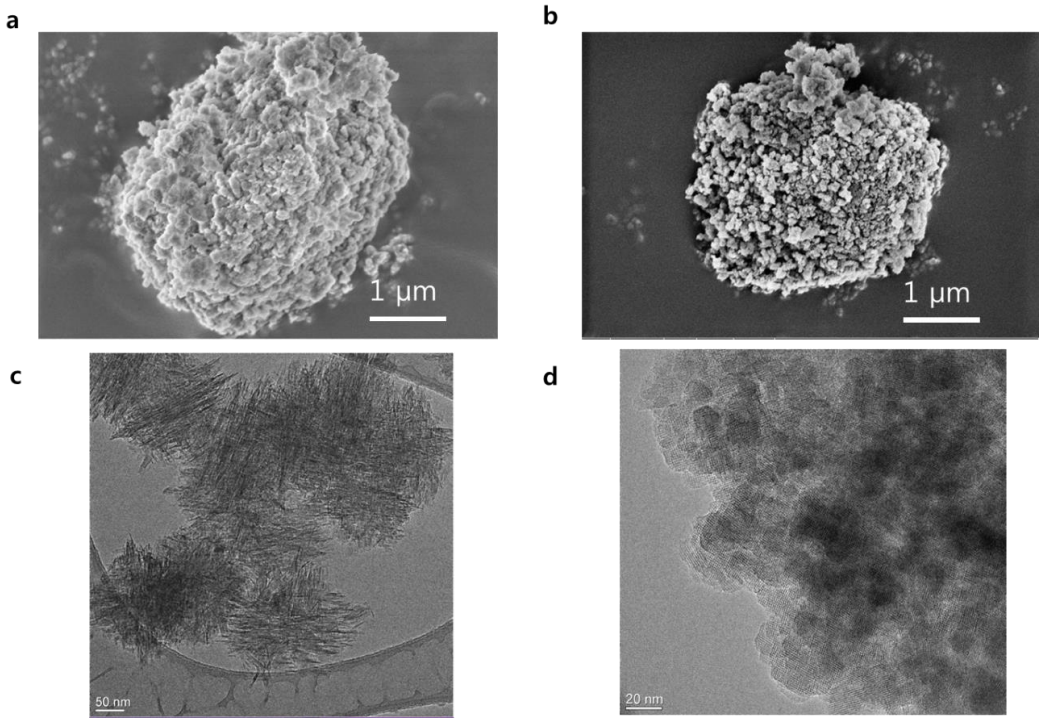

Figure 5.2 SEM images of (a) Al-BEA (Zeolyst, CP814E, Si/Al = 12.5) and (b) P-BEA, and TEM images of (c) P-SPP and (d) P-BEA.

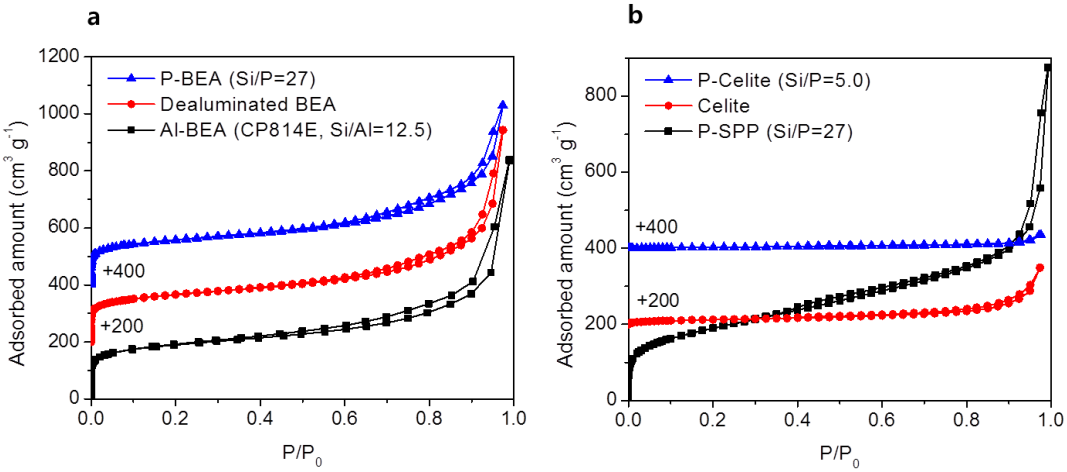

Figure 5.3 Argon adsorption-desorption isotherms for (a) P-BEA, dealuminated BEA and Al-BEA and (b) P-Celite, Celite and P-SPP. The isotherms of dealuminated BEA (DeAl-BEA) and Celite were shifted upward by 200 and those of P-BEA and P-Celite by 400.

Table 5.1 ICP analysis and textural properties of the samples

Catalysts	Si/P [a] (mol mol^{-1})	Si/Al [a] (mol mol^{-1})	Micropore volume [c] (cm^3 g^{-1})	Surface area [d] (m^2 g^{-1})	Total pore volume [e] (cm^3 g^{-1})
P-BEA	27.1	1471	0.10	499	0.801
DeAl-BEA	-	1465	0.07	508	0.946
Al-BEA	-	12.5 [b]	0.15	563	1.069
P-SPP	27.3	N.D. [f]	0.08	598	1.114
P-Celite	5.0	13.3	0.00	12	0.045

[a] Determined by ICP. [b] Data from supplier. [c] *t*-plot method obtained from Ar Adsorption-desorption isotherms. [d] BET surface area obtained from Ar Adsorption-desorption isotherms. [e] Calculated from the amount adsorbed at $P/P_0 = 0.97$ in Ar Adsorption-desorption isotherms. [f] N.D. = Not detected.

A second P-containing zeolite investigated is a hierarchical MFI zeolite called self-pillared pentasil (SPP).[27] P-containing self-pillared pentasil (P-SPP) was synthesized by a direct synthesis method using tetrabutylphosponium hydroxide (TBPOH) as OSDA.[27] After crystallization, the formed SPP zeolite containing the OSDA was calcined, resulting in the decomposition of the OSDA and incorporation of P within the zeolite, as evidenced by ICP (Table 5.1). In contrast, the use of tetrabutylammonium hydroxide (TBAOH) as the OSDA or extensive washing of TBPOH-synthesized SPP with water results in a SPP zeolite free of phosphorous active sites. The crystallinity and morphology of P-SPP are the same as those of pure silica SPP displaying orthogonally connected single-unit cell lamellae of MFI,[27] as indicated by the XRD patterns, TEM images and Ar adsorption isotherms (Figures 5.1-5.3). For further comparison, a commonly used P-based catalyst, P-Celite, was also examined. It is a solid phosphoric acid (SPA) catalyst synthesized by impregnation of H_3PO_4 on Celite (diatomaceous silica), a commercially available amorphous silica material (Figures 5.1-5.3 and Table 5.1).[173, 177]

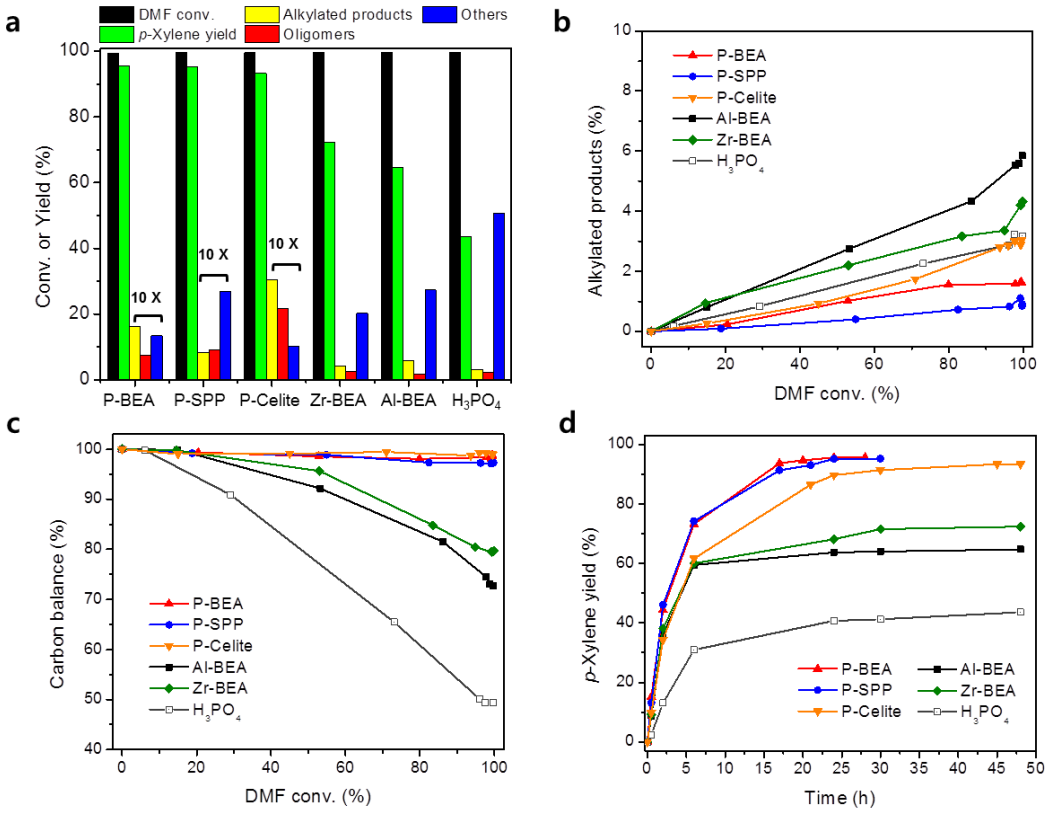

Figure 5.4 Catalytic performance of various catalysts for the *p*-xylene production from the reaction of DMF with ethylene: (a) overall product distributions, (b) yield of alkylated by-products, (c) carbon balance versus DMF conversion and (d) yield of *p*-xylene versus reaction time. Reaction conditions are as follows: 1.35 M DMF in *n*-heptane; 250 °C; 62 bar ethylene; DMF/P (mol mol^{-1}) = 100 for P-BEA, P-SPP, P-Celite and H_3PO_4; 4.0 mM acid for Al-BEA and Zr-BEA. Reaction times in (a) for all catalysts were 48 h, except 24 h for P-BEA and P-SPP.

Figure 5.4 shows the results from reacting DMF with ethylene over the P-containing solid catalysts, other Brønsted and Lewis acid zeolites and a homogeneous acid catalyst, H_3PO_4, under the same acid concentration (4.0 mM for both Brønsted and Lewis acid sites) or the same DMF/P molar ratio = 100 at 250 °C. All P-containing materials catalyze the reaction to some extent producing *p*-xylene (Figure 5.4a). In the absence of P, the same zeolites (siliceous zeolites; Si-SPP made using TBAOH, and Si-BEA)

did not exhibit detectable catalysis (Figure 5.5). Among the catalysts, P-BEA (Si/P = 27) and P-SPP (Si/P = 27) exhibited superior performances with an excellent yield (97%) of *p*-xylene at 99% DMF conversion (Figure 5.4a). The remarkable properties of P-BEA and P-SPP could be attributed to the large micropore of P-BEA and the highly branched hierarchical micro-/meso-porous structure of P-SPP, respectively, which provide efficient dispersion of the active sites and facile transport of reactants and products.[21, 117] The non-zeolitic P-based solid catalyst, P-Celite (Si/P = 5.0), showed a high *p*-xylene yield (about 90%), but lower than those obtained from P-BEA and P-SPP. The yields of *p*-xylene from Brønsted acid Al-BEA and Lewis acid Zr-BEA were significantly lower (i.e., 65% and 72% at 99% DMF conversion, respectively). Homogeneous H_3PO_4 also catalyzed the reaction but with a much lower yield to *p*-xylene (i.e., 39% at 99% DMF conversion). A control experiment conducted over P-containing Al-BEA prepared by impregnation of P on Al-BEA, P-Al-BEA, using the same post-synthetic method as P-BEA showed a low yield to *p*-xylene, suggesting that the use of siliceous zeolites as P supports is essential for the high-yield production of *p*-xylene (Figure 5.6).

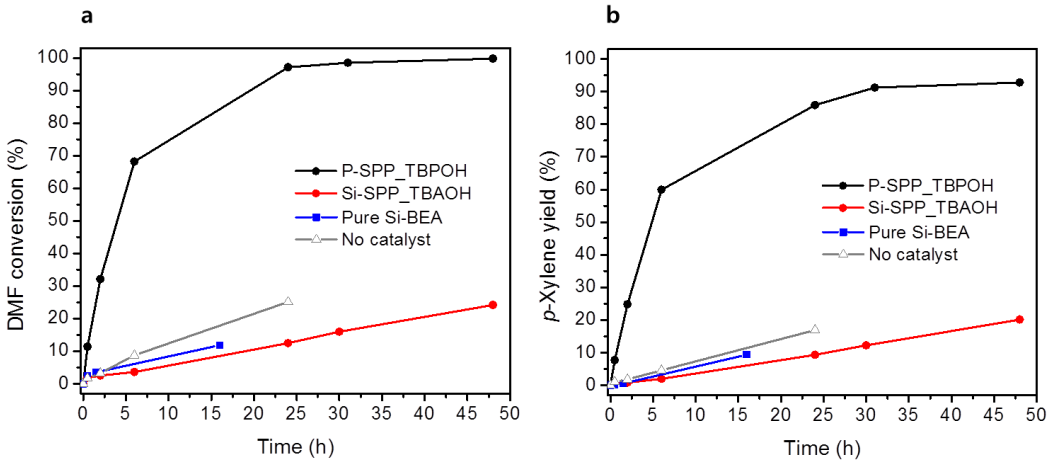

Figure 5.5 Catalytic activities for the DMF reaction with ethylene over P-SPP made using TBPOH, Si-SPP made using TBAOH, pure siliceous BEA and no catalyst: (a) DMF conversion and (b) *p*-xylene yield. Reaction conditions are as follows: 50 mL of 1.35 M DMF in *n*-heptane; 250 °C; 62 bar ethylene; 0.228 g catalyst.

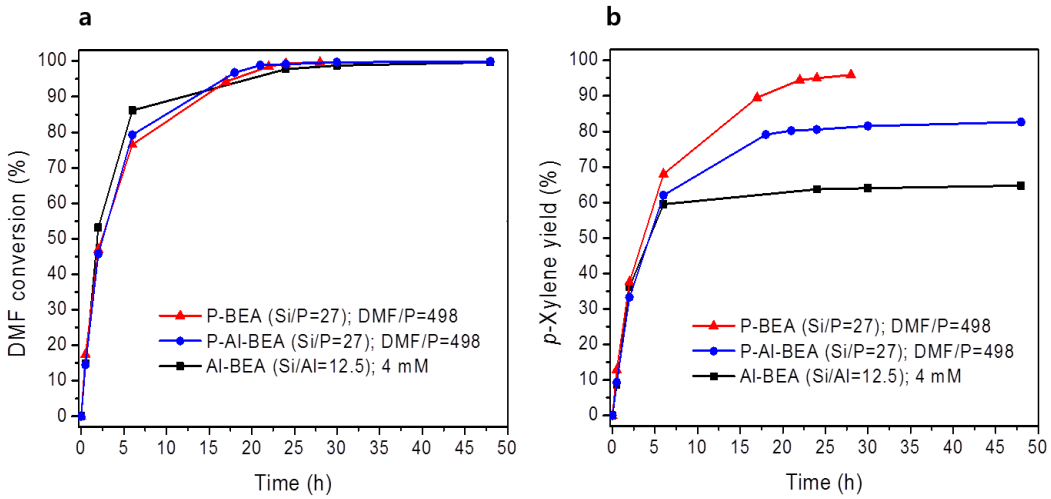

Figure 5.6 Catalytic performances of P-Al-BEA for the production of *p*-xylene: (a) DMF conversion and (b) *p*-xylene yield. Reaction conditions are as follows: 1.35 M DMF in *n*-heptane; 250 °C; 62 bar ethylene.

The yield of alkylated by-products and carbon balance versus DMF conversion (Figure 5.4b and c), respectively, and the yield to *p*-xylene with reaction time (Figure 5.4d) illustrate the excellent catalytic properties of the P-containing microporous silica materials for this reaction. Outstanding performance of the P-containing catalysts is due to the lower rate of formation of by-products, such as alkylated aromatics and other unidentified products formed during the reaction. Al-BEA, Zr-BEA and H_3PO_4, however, produced more alkylated and oligomerized by-products with rapid reduction of quantified carbon (i.e., lower carbon balance) (Figure 5.4b and c, Figure 5.7). Although DMF can be fully converted over Al-BEA, Zr-BEA and H_3PO_4 catalysts, the *p*-xylene yield did not increase after 6 h of reaction time (Figure 5.4d and Figure 5.7a); this is likely due to coke formation and blockage of the active sites. Compared to the Brønsted acidity of Al-OH-Si sites in Al-BEA, the active sites on the P-containing catalysts still catalyze the dehydration reaction to produce *p*-xylene, but only catalyze the side reactions at very slow rates.

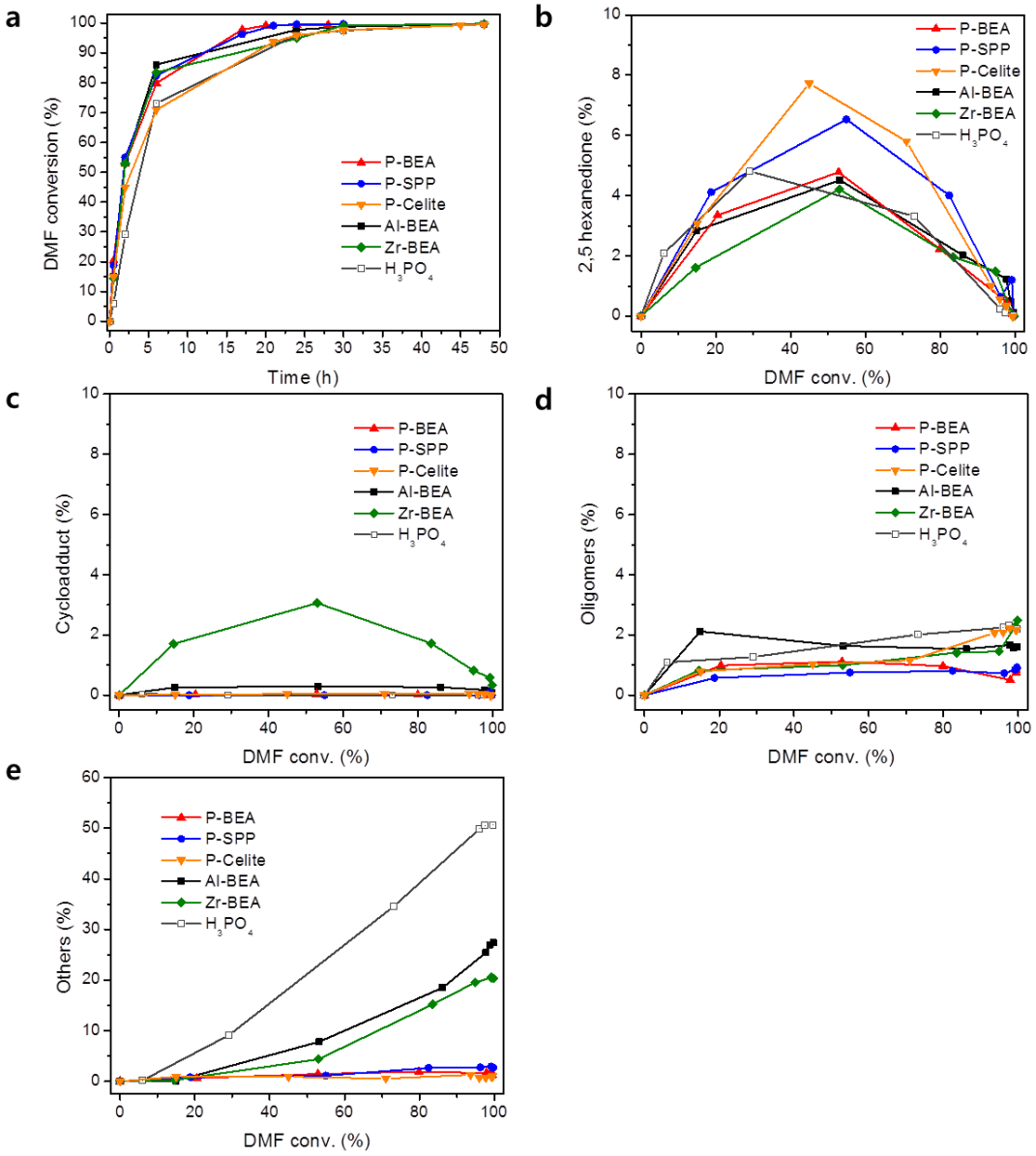

Figure 5.7 Catalytic activities for the *p*-xylene production from the reaction of DMF with ethylene: (a) DMF conversion and (b-e) overall product distributions. Reaction conditions are as follows: 1.35 M DMF in *n*-heptane; 250 °C; 62 bar ethylene; DMF/P (mol mol^{-1}) = 100 for P-BEA, P-SPP, P-Celite and H_3PO_4; 4.0 mM acid for Al-BEA and Zr-BEA.

Catalyst removal and recycle tests were conducted to verify that the reactions are heterogeneously catalyzed and not catalyzed due to the leaching of phosphorous

into the reaction mixture. In the catalyst removal test, the reaction of DMF was performed after separating the spent P-BEA catalyst from the reaction mixture. Upon removal of the catalyst the reaction showed almost the same reaction rate as a control experiment without a catalyst, indicating that the catalytic activity observed was fully attributed to the solid catalyst (Figure 5.8). In Figure 5.9a, the reusability of the P-BEA catalyst was tested showing high selectivity to *p*-xylene (94%) at 98% conversion of DMF after the third recycling test. There were no significant changes in structure of P-BEA catalyst during the recycling test, as determined by SEM and XRD measurement (Figure 5.10). However, *p*-xylene yield from P-SPP was considerably reduced after sequential catalyst recycling (Figure 5.9b). By the third recycle, DMF conversion decreased to 76% with a *p*-xylene yield of only 65% (Figure 5.9c).

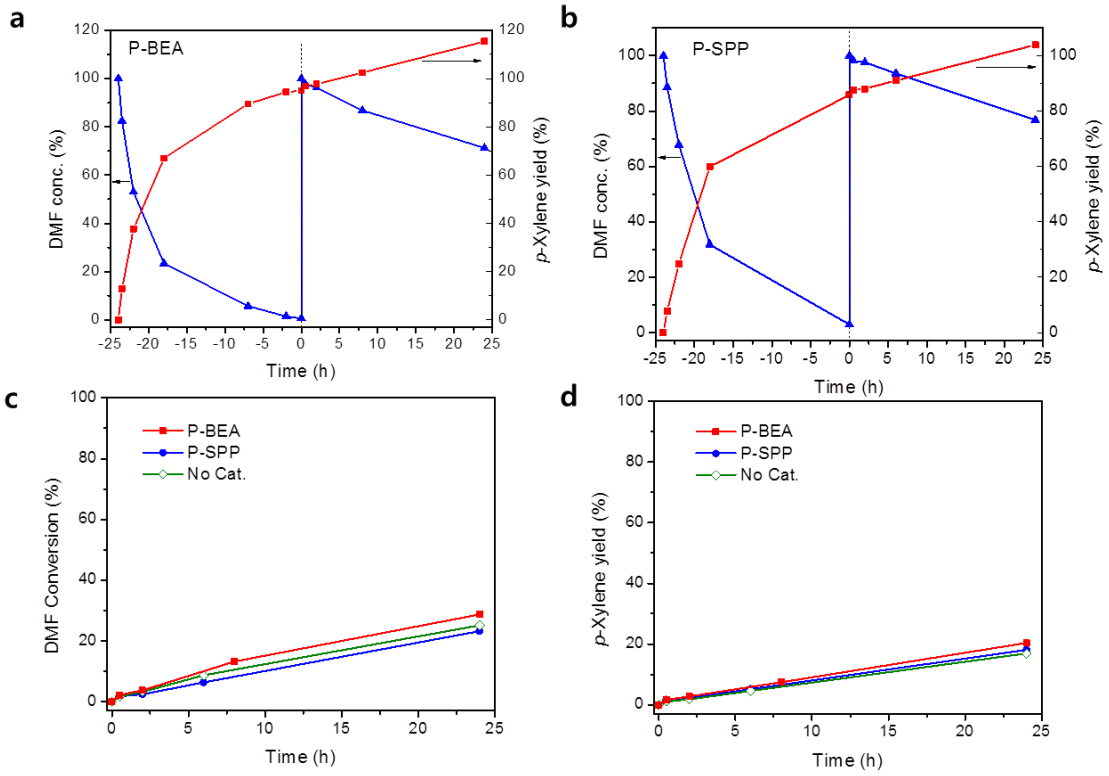

Figure 5.8 Heterogeneous nature of the DMF reaction with ethylene over P-BEA and P-SPP (a-d). Reaction conditions are as follows: 50 mL of 1.35 M DMF in *n*-heptane; 250 °C; 62 bar ethylene; DMF/P (mol mol^{-1}) = 498 for P-BEA and P-SPP; 24 h. The spent catalyst was removed from the reactor after 24 h of reaction. Fresh DMF was filled at 0 h on the plots (a) and (b), followed by the reaction occurring for additional 24 h. The DMF conversion and *p*-xylene yield obtained from the experiments were similar to the blank experiments, indicating the reaction was heterogeneously catalyzed.

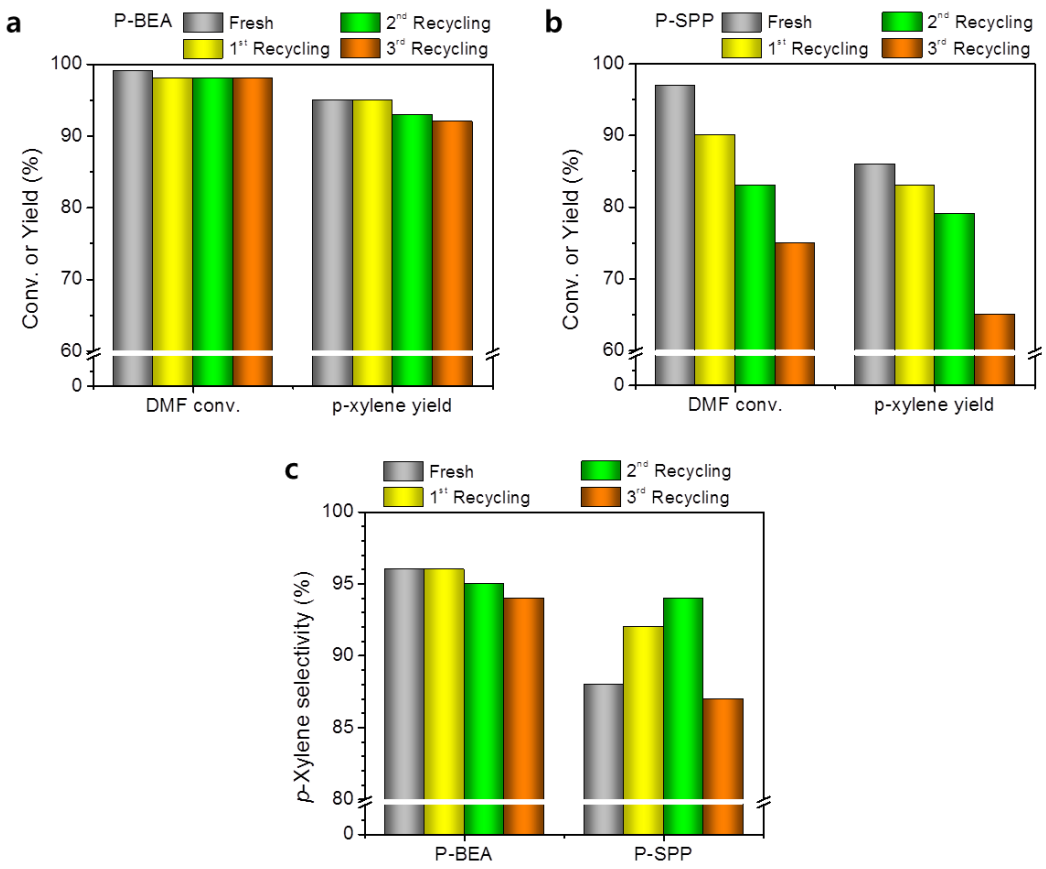

Figure 5.9 Catalyst reusability of P-containing catalysts: (a,b) DMF conversion and *p*-xylene yield over P-BEA and P-SPP during catalyst recycling and (c) *p*-xylene selectivity over P-BEA and P-SPP during catalyst recycling. Reaction conditions are as follows: 50 mL of 1.35 M DMF in *n*-heptane; 250 °C; 62 bar ethylene; DMF/P (mol mol^{-1}) = 498 for P-BEA and P-SPP; 24 h. For catalyst reusability, the spent catalyst was washed with *n*-heptane, dried and calcined at 550 °C for 12 h.

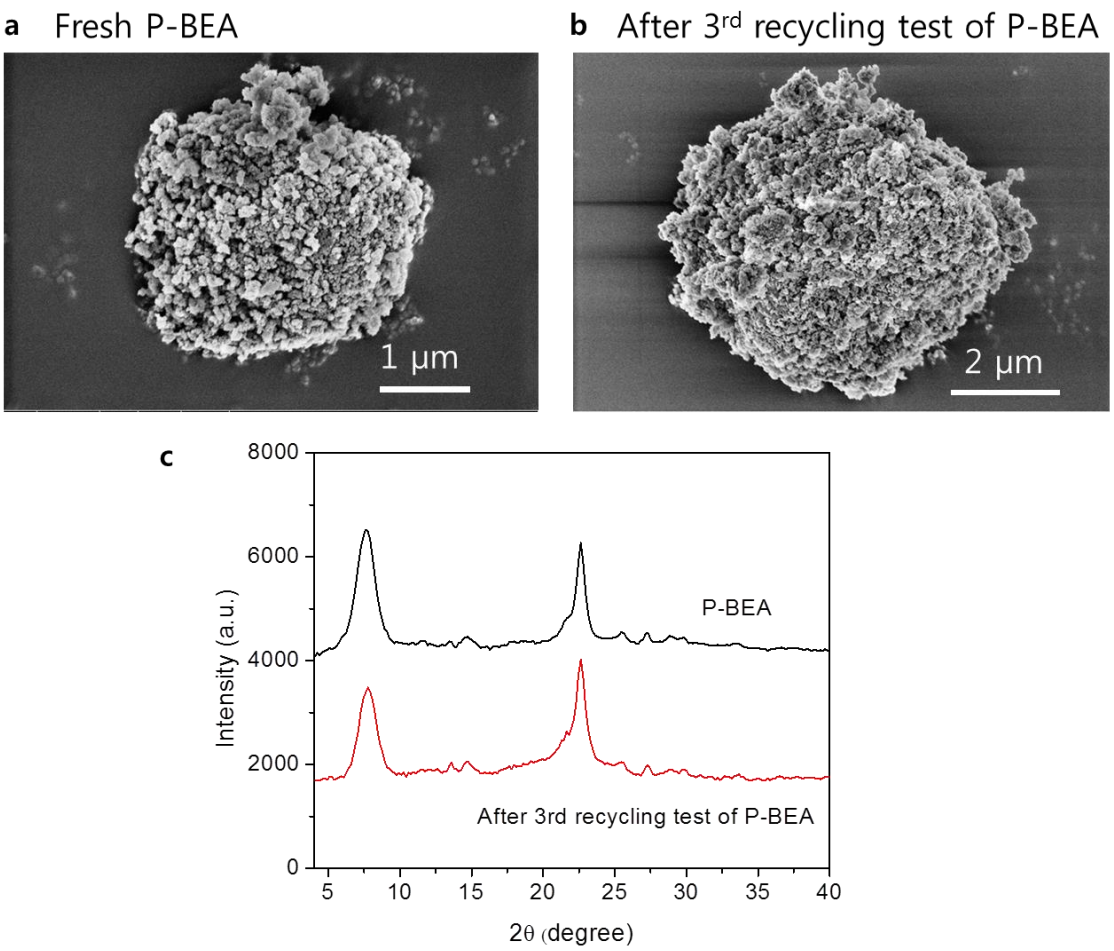

Figure 5.10 SEM images (a-b) and XRD patterns (c) of fresh P-BEA and spent P-BEA after 3rd recycling test.

^{31}P solid state MAS NMR provided insights into the chemical interaction of P with the silicate frameworks of the P-containing catalysts. As displayed in Figure 5.11, P-BEA and P-SPP showed three main signals at 0 (Q^0), -11 (Q^1) and -24 (Q^2) ppm that could be assigned to free H_3PO_4 not chemically bonded to silicate matrices, to O=P(OSi or OP)$(OH)_2$ and to O=P(OSi or OP)$_2$(OH), respectively.[178, 179] The relative peak area for the P-BEA was 35% for Q^0, 46% of Q^1 and 19% of Q^2 while P-SPP exhibited 68% for Q^0, 26%

of Q^1 and 6% of Q^2. These spectra indicate that P binds more effectively in the micropores of the dealuminated BEA than with Si-SPP. P-Celite presented two main resonance peaks at -45 (Q^4) and -54 ppm, corresponding to PO_4 tetrahedra (oligomers of P) and silicon pyrophosphate (SiP_2O_7), respectively, in agreement with previous reports on phosphosilicate materials.[180, 181] Although all the three P-containing materials catalyze the *p*-xylene production, P speciation detected by the MAS NMR is distinctly different. The enhanced catalytic performance of P-BEA and P-SPP (Table 5.2) could arise from the presence of isolated P sites, which are not dominant in the conventional solid phosphoric acid catalyst (i.e., P-Celite).

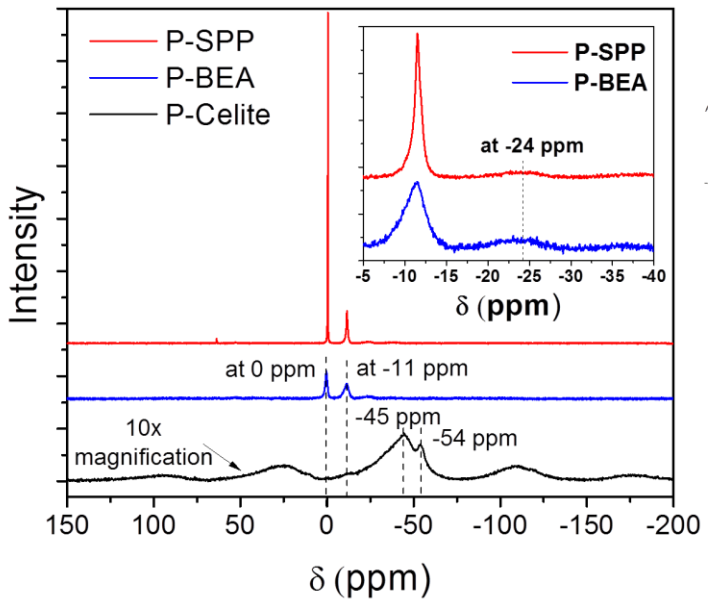

Figure 5.11 ^{31}P solid state MAS NMR spectra of P-BEA, P-SPP and P-Celite.

Table 5.2 Comparison of catalytic activities for DMF reaction with ethylene in this study[a]

Catalyst	DMF/P (mol mol^{-1})	Production rate of *p*-xylene[b,c] (mM h^{-1})	DMF conv.[c] at 24 h (%)	*p*-xylene yield[c] at 24 h (%)	*p*-xylene selectivity at 24 h (%)
P-BEA	100	411 (± 21)	99 (± 0.7)	97 (± 1.1)	98
P-SPP	100	357 (± 20)	100 (± 0.3)	97 (± 1.3)	97
P-Celite	100	268 (± 17)	96 (± 1.1)	90 (± 1.5)	94
H_3PO_4	100	67	96	41	43
Al-BEA	4 mM[d]	214	98	64	65
Zr-BEA	4 mM[d]	249	99	72	73
P-BEA[e]	498	349 (± 12)	99 (± 0.6)	95 (± 1.3)	96
P-SPP[e]	498	209 (± 10)	97 (± 1.1)	86 (± 1.6)	89
Al-BEA	1 mM[d]	122 (± 11)	55 (± 3.7)	30 (± 0.5)	55
Zr-BEA	1 mM[d]	129 (± 5)	84 (± 1.6)	65 (± 1.6)	77
Si-BEA[e]	-	6 (± 1.7)	12[f] (± 2.3)	9[f] (± 2.4)	75[f]
Si-SPP[e]	-	14	13	9	69

[a] Reaction conditions: 50 mL of 1.35 M DMF in *n*-heptane; 250 °C; 62 bar ethylene. [b] Reaction time: 30 min. [c] 95% confidence interval in parentheses. [d] Concentration of Brønsted acid sites on Al-BEA, and that of Lewis acid sites on Zr-BEA. [e] 0.228 g of catalyst. [f] Reaction time: 16 h.

Temperature-programmed desorption coupled with thermogravimetric analysis (TPD-TGA) of 2-propanamine was used to characterize the active sites on the P-containing solid catalysts. 2-Propanamine molecules that are protonated by Brønsted sites react via the Hoffman-elimination to form ammonia and propene, allowing easy quantification of Brønsted-site density.[182] The results are shown in Figure 5.12. After P-BEA, P-SPP and P-Celite were saturated with 2-propanamine at room temperature, initial coverage of 2-propanamine was around 1100 µmol g^{-1}, 1200 µmol g^{-1} and 600 µmol g^{-1}, respectively. Physically adsorbed 2-propanamine was desorbed from the samples below 300 ^{o}C. No significant decomposition of 2-propanamine was observed

over P-BEA and P-SPP, suggesting no Brønsted acid sites on either P-BEA or P-SPP. However, P-Celite possessed Brønsted-site density of 150 μmol g^{-1} evidenced by the formation of ammonia and propene between 300 °C and 380 °C. In the same experiment, Al-BEA showed Brønsted-site density of 620 μmol g^{-1}. By this measurement, the observation that there are no significant Brønsted acid sites on P-BEA is consistent with the pyridine FT-IR measurement on the dehydrated P-BEA sample as seen in Figure 5.13. A demonstration that the P-containing zeolites have catalytic sites was shown by the ability of P-BEA to catalyze dehydration of 2,5-hexanedione during the TPD-TGA measurement. The dehydration of 2,5- hexanedione into DMF and water occurred at moderate temperatures (around 180 °C), without catalyzing the oligomerization of DMF (Figure 5.14). Previous work has shown that the Brønsted acid sites in Al-BEA catalyze the dehydration of 2,5-hexanedione at low temperatures; however, the Brønsted acid sites also catalyzed the oligomerization of DMF during desorption.[118]

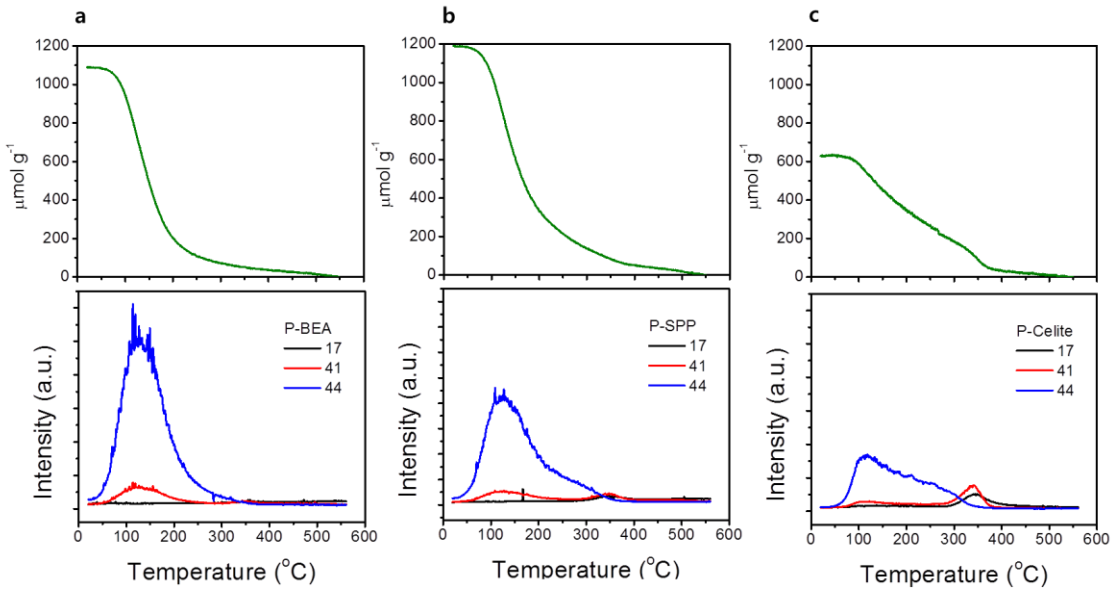

Figure 5.12 TPD-TGA of 2-propanamine on (a) P-BEA, (b) P-SPP and (c) P-Celite. The peaks correspond to ammonia (m/z = 17), propene (m/z = 41) and 2-propanamine (m/z = 44).

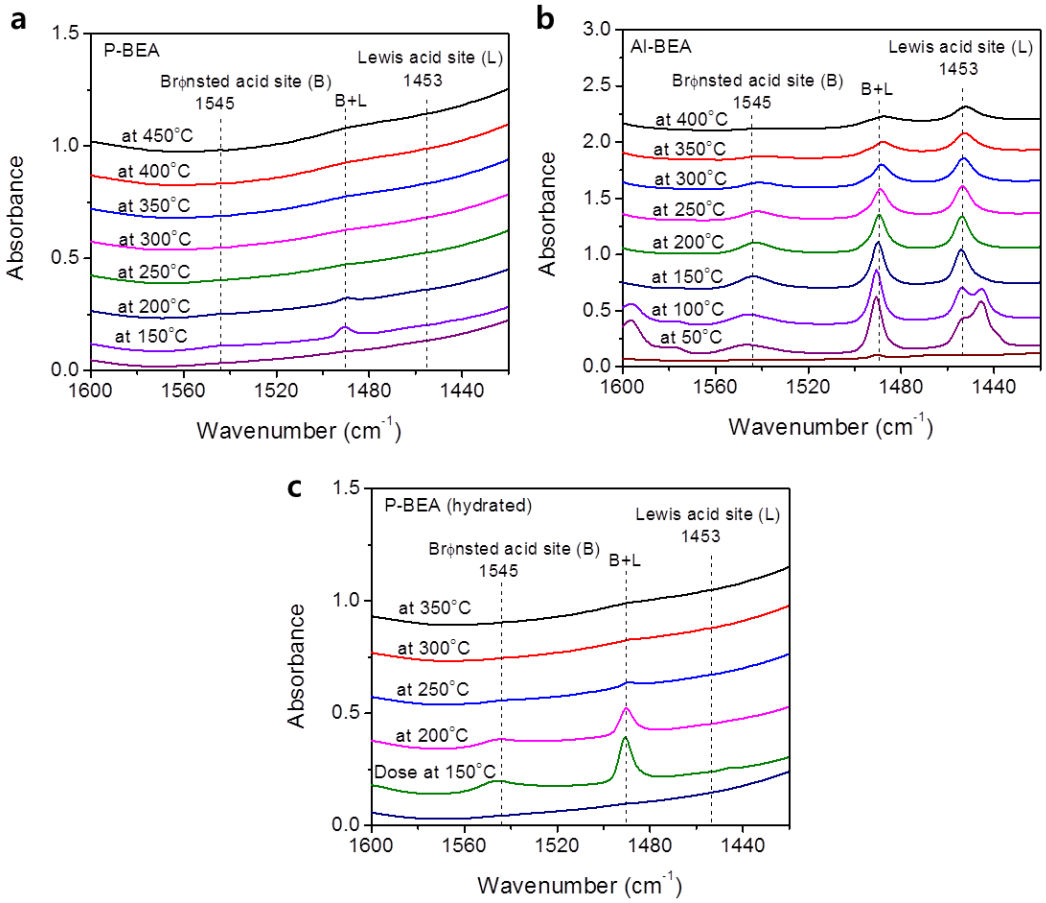

Figure 5.13 Pyridine FT-IR spectra of (a) P-BEA and (b) Al-BEA under dehydrated condition and (c) P-BEA under hydrated condition. After Al-BEA and P-BEA were evacuated at 450 ^{o}C for 1 h, they were saturated with pyridine at 50 ^{o}C and 150 ^{o}C, respectively under dehydrated condition. For collecting the spectra under hydrated condition, a 10% volume pyridine in water mixture was used. In the desorption stage of the adsorbate, FT-IR spectra were shown every 50 ^{o}C. The peak at 1545 cm^{-1} is associated with Brønsted acid sites, 1490 cm^{-1} is associated with Brønsted acid sites or Lewis acid sites, and 1453 cm^{-1} is associated with Lewis acid sites. For P-BEA, a very weak peak corresponding to Brønsted acid sites was observed at 1545 cm^{-1} in the FT-IR spectrum, and disappeared when the temperature was increased to 250 ^{o}C (Figure 5.13a), much lower than Al-BEA.

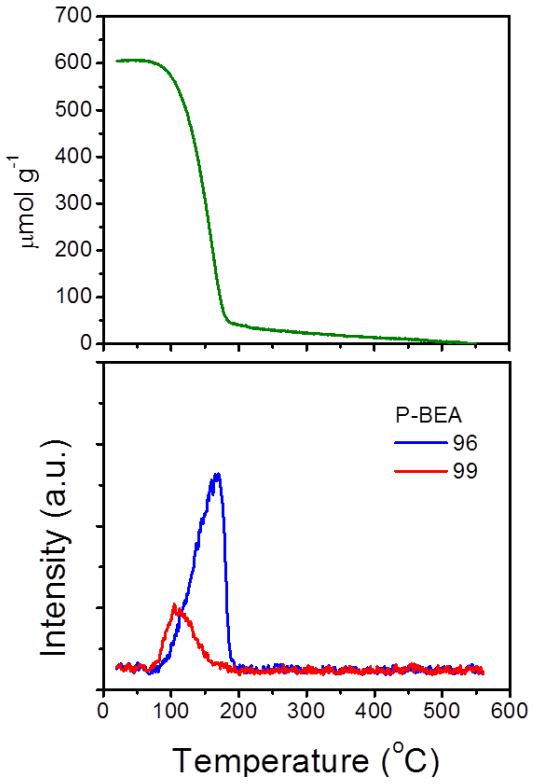

Figure 5.14 TPD-TGA of 2,5-hexanedione on P-BEA. The peaks correspond to 2,5-hexanedione (m/z = 99) and DMF (m/z = 96). P-BEA was exposed to 2,5-hexanedione with an initial coverage of 600 µmol g^{-1} at room temperature. The appearance of DMF at moderate temperature (100 – 200 °C) during the TPD-TGA measurement suggests the dehydration of 2,5-hexanedione to DMF can occur on P-BEA catalyst. Interestingly, no further oligomerization of DMF was observed over P-BEA catalyst. Previous study demonstrated that the Brønsted acid sites in Al-BEA catalyze the dehydration of 2,5-hexanedione at low temperatures; however, the Brønsted acid sites also catalyzed the oligomerization of DMF during desorption.[118]

CHAPTER 6

CONCLUSIONS

In the first part of the thesis, hierarchical Sn-MFI catalysts with mesoporous structures were successfully synthesized within the confined space of 3DOm carbon by a seeded growth approach. The obtained 3DOm-i Sn-MFI consisting of 30 nm spherical elements forming an opaline structure contains highly ordered mesopores ranging from 4 to 11 nm. Compared with conventional Sn-MFI, this hierarchical catalyst exhibits superior catalytic performance for the isomerization of cellulosic sugars. No diffusion limitation was observed for the isomerization of a triose sugar, DHA, into methyl lactate (ML). 3DOm-i Sn-MFI offers significant improvements for the isomerizations of C_5 and C_6 sugars, such as xylose and glucose, by greatly enhancing molecular transport. The reaction rate of xylose on 3DOm-i Sn-MFI is at least 20 times higher than that on conventional bulky sized Sn-MFI. The reaction rate for glucose is also enhanced by using 3DOm-i Sn-MFI, but to a lesser extent as compared with the reaction of xylose, possibly because glucose cannot diffuse into the 10-membered-ring pore of MFI, and the reaction is catalyzed only on the external surface of the Sn-MFI catalysts. Moreover, the combination of seeded growth with confined synthesis allows us to synthesize hierarchical Sn-MFI, indicating that the synthesis strategy is a versatile and reliable method for tailoring the structure of hierarchical zeolites.

In the second part of this thesis, we have developed a base-free one-pot reaction pathway to produce LA in high yields from the oxidation of glycerol over a bifunctional

Pt/Sn-MFI catalyst under mild conditions. In the cascade reaction route, the selective oxidation of glycerol to GLA proceeds on the Pt catalyst. Subsequently, Sn-MFI exhibits outstanding Lewis acidity for converting GLA into DHA and DHA into the final product LA. The superior performance is mainly due to its microporous structure, accessible Sn sites and Lewis acidity.

In the third part of this thesis, hydrophobic Sn-BEA zeolites with different crystal morphologies were successfully synthesized by recrystallization of post-synthesized Sn-BEA (Sn-BEA-PS) using NH_4F and TEABr. The recrystallization includes simultaneous procedures of dissolution-reassembly. The dissolution of Sn-BEA-PS surface by fluoride ions occurs on mainly silanol nests. The etched silica species were reorganized in the presence of TEA ions, forming defect-free Si-O-Si bonds on the surface of recrystallized Sn-BEA (Sn-BEA-RC). Although this recrystallization could not fully eliminate silanol defects, the reduced density of silanol nests on Sn-BEA-RC mitigates the interaction with water, rendering Sn-BEA-RC more hydrophobic than Sn-BEA-PS. In addition, this method also increased open Lewis acid Sn sites. These findings can explain why Sn-BEA-RC achieved a 2.5 times higher activity for aqueous glucose isomerization, compared with Sn-BEA-PS. Moreover, similar catalytic activities of Sn-BEA irrespective of particle size and mesoporosity indicate no diffusion limitation of glucose into BEA micropores. In the isomerization of bulky lactose (C_{12} sugar) dissolved in MeOH, however, hierarchical Sn-BEA-RC showed a 3.2-fold higher activity than hydrothermally synthesized Sn-BEA (Sn-BEA-HF), due to the mesopores and enhanced organophobic character of the recrystallized catalyst. These unique properties of Sn-BEA-RC open new opportunities in

applications of catalysis, separation and adsorption.

In the last part of the thesis, phosphorous-containing zeolite with BEA topology, P-BEA, exhibited an unprecedented *p*-xylene yield of 97% in the Diels-Alder cycloaddition and dehydration of DMF with ethylene, and establishes a commercially attractive process for renewable *p*-xylene production. This material is able to selectively catalyze the dehydration reaction from the furan-ethylene cycloadduct to *p*-xylene, without performing side reactions which include alkylation and oligomerization. This catalytic behavior is distinct from that of Al-containing zeolites and other solid phosphoric acid catalysts. The results presented here demonstrate that P-containing zeolite materials have intrinsically new catalytic properties and are a novel class of acidic zeolite catalysts, worthy of further investigation for other dehydration and acid catalyzed reactions.

CHAPTER 7

SUGGESTED FUTURE DIRECTIONS

In Chapter 2, hierarchical Sn-MFI zeolites led to higher catalytic activities for C_5 and C_6 sugar isomerization than conventional Sn-MFI zeolites because C_5 and C_6 sugar molecules are bigger than MFI pore dimension and thus, mesopores in the hierarchical zeolites likely facilitate the molecular diffusion. Also, three different Sn-MFI zeolites had the same initial catalytic activity for C_3 sugar isomerization, indicating there is no diffusion limitation in MFI pore channels. Nevertheless, how such sugar substrates diffuse into Sn-MFI zeolites with different morphology remains unclear, in order to directly provide evidences on the molecular diffusion into Sn-MFI zeolites, apart from the chemical reactions. This study will include the adsorption of sugar molecules into the zeolite MFI pore.

In Chapter 3, a bifunctional Pt/Sn-MFI catalyst has been shown to be very active for the conversion of base-free glycerol into lactic acid. But, as shown in Figure 3.7, the spent catalyst led to a gradual decrease in catalyst activity with recycling the catalyst. This trend has also been found over Pt/TiO_2 catalyst for conversion of glycerol into lactate in the presence of base.[113] Regarding catalyst deactivation in oxidation reactions over metal/support catalysts, it is generally believed that there are four main reasons for the deactivation:[183] i) coke formation on the catalyst, ii) metal leaching from the support, iii) over-oxidation of metal during the oxidation (i.e., evolution from metal to metal oxide), and iv) metal sintering during the reaction. Thus, further study will be able

to focus on why the activity from Pt/Sn-MFI was partly lost during the recycling test and how to improve the catalyst reusability.

In Chapter 4, Sn-BEA-RC obtained from the recrystallization possessed higher hydrophobicity than Sn-BEA-PS, by greatly reducing silanol nests of Sn-BEA-PS. Nevertheless, Sn-BEA-RC was still less hydrophobic than Sn-BEA-HF because higher silanol defects such as internal and external Si-OH groups were observed on Sn-BEA-RC, in comparison with the counterpart. Along this line, future research will focus on how to further decrease silanol defects by recrystallization. In addition, interestingly, this recrystallization enables Sn-BEA-RC to have more open Lewis acid Sn sites than closed ones. But, the transformation from closed Sn sites to open Sn ones has been poorly understood during the recrystallization. Another direction involves organophobic character of Sn-BEA-RC. Because Sn-BEA-RC shows higher organophobicity than Sn-BEA-PS and Sn-BEA-HF, Sn-BEA-RC can be promising for other catalytic reactions in organic solvents.

In Chapter 5, phosphorus-containing zeolites such as P-BEA were synthesized and exhibited remarkable performances of converting DMF into *p*-xylene. The high activities of P-BEA can arise from the Brønsted acid sites (P-OH) groups on the materials, which are distinct from that of Al-containing zeolites. Thus, it is inevitable to study how to quantify Brønsted acidic P-OH groups, in contrast to well-known studies on the titration of Brønsted acidic Al-OH-Si groups on Al-containing zeolites by 2-propanamine.[182, 184] In addition, as P-NMR data show in Figure 5.11, P-BEA has three different phosphorous structures (Q^0 with three P-OH groups, Q^1 with two P-OH groups,

and Q^2 with one P-OH group). It is interesting to identify how P-OH groups in different P-structures contribute to Brønsted acidity, since phosphoric acid H_3PO_4 with three P-OH groups shows different degrees of deprotonation. Besides, as shown in Figure 5.13c, the presence of water creates more Brønsted acid sites, which can be caused by hydrolysis of P-O-P or Si-O-P bonds on the catalyst into P-OH or Si-OH groups. Because water is generated as a result of 2^{nd} step of cycloadduct dehydration (Scheme 5.1), systematic studies on the effect of water on the catalytic active sites are necessary. Moreover, because P-containing zeolite materials are a novel class of acidic zeolite catalysts, these are worthy of further investigation for other dehydration and acid catalyzed reactions.

BIBLIOGRAPHY

1. Holm, M. S.; Saravanamurugan, S.; Taarning, E., Conversion of Sugars to Lactic Acid Derivatives Using Heterogeneous Zeotype Catalysts. *Science* **2010,** 328, (5978), 602-605.
2. Huber, G. W.; Iborra, S.; Corma, A., Synthesis of transportation fuels from biomass: Chemistry, catalysts, and engineering. *Chem. Rev.* **2006,** 106, (9), 4044-4098.
3. Huber, G. W.; Corma, A., Synergies between bio- and oil refineries for the production of fuels from biomass. *Angew. Chem. Int. Ed.* **2007,** 46, (38), 7184-7201.
4. Wang, L.; Xiao, F. S., Nanoporous catalysts for biomass conversion. *Green Chem.* **2015,** 17, (1), 24-39.
5. Taarning, E.; Osmundsen, C. M.; Yang, X. B.; Voss, B.; Andersen, S. I.; Christensen, C. H., Zeolite-catalyzed biomass conversion to fuels and chemicals. *Energ. Environ. Sci.* **2011,** 4, (3), 793-804.
6. Corma, A., From microporous to mesoporous molecular sieve materials and their use in catalysis. *Chem. Rev.* **1997,** 97, (6), 2373-2419.
7. Davis, M. E., Ordered porous materials for emerging applications. *Nature* **2002,** 417, (6891), 813-821.
8. Lewis, J. D.; Van de Vyver, S.; Roman-Leshkov, Y., Acid-Base Pairs in Lewis Acidic Zeolites Promote Direct Aldol Reactions by Soft Enolization. *Angew. Chem. Int. Ed.* **2015,** 54, (34), 9835-9838.
9. Auerbach, S. M.; Carrado, K. A.; Dutta, P. K., *Handbook of Zeolite Science and Technology*. CRC Press: 2003.
10. Sheldon, R. A., Green and sustainable manufacture of chemicals from biomass: state of the art. *Green Chem.* **2014,** 16, (3), 950-963.
11. Chheda, J. N.; Huber, G. W.; Dumesic, J. A., Liquid-phase catalytic processing of biomass-derived oxygenated hydrocarbons to fuels and chemicals. *Angew. Chem. Int. Ed.* **2007,** 46, (38), 7164-7183.
12. Moliner, M.; Roman-Leshkov, Y.; Davis, M. E., Tin-containing zeolites are highly active catalysts for the isomerization of glucose in water. *Proc. Natl. Acad. Sci. U.S.A.* **2010,** 107, (14), 6164-6168.
13. Garcia, R.; Besson, M.; Gallezot, P., Chemoselective Catalytic-Oxidation of Glycerol with Air on Platinum Metals. *Applied Catalysis a-General* **1995,** 127, (1-2), 165-176.
14. Jerome, F.; Pouilloux, Y.; Barrault, J., Rational Design of Solid Catalysts for the Selective Use of Glycerol as a Natural Organic Building Block. *Chemsuschem* **2008,** 1, (7), 586-613.
15. Liang, D.; Gao, J.; Sun, H.; Chen, P.; Hou, Z.; Zheng, X., Selective oxidation of glycerol with oxygen in a base-free aqueous solution over MWNTs supported Pt catalysts. *Applied Catalysis B: Environmental* **2011,** 106, (3–4), 423-432.
16. Katryniok, B.; Kimura, H.; Skrzynska, E.; Girardon, J. S.; Fongarland, P.; Capron, M.; Ducoulombier, R.; Mimura, N.; Paul, S.; Dumeignil, F., Selective catalytic oxidation of glycerol: perspectives for high value chemicals. *Green Chemistry* **2011,** 13, (8), 1960-1979.

17. Pagliaro, M.; Ciriminna, R.; Kimura, H.; Rossi, M.; Della Pina, C., From glycerol to value-added products. *Angewandte Chemie-International Edition* **2007,** 46, (24), 4434-4440.
18. Roman-Leshkov, Y.; Chheda, J. N.; Dumesic, J. A., Phase modifiers promote efficient production of hydroxymethylfurfural from fructose. *Science* **2006,** 312, (5782), 1933-1937.
19. Wang, G. H.; Hilgert, J.; Richter, F. H.; Wang, F.; Bongard, H. J.; Spliethoff, B.; Weidenthaler, C.; Schuth, F., Platinum-cobalt bimetallic nanoparticles in hollow carbon nanospheres for hydrogenolysis of 5-hydroxymethylfurfural. *Nat. Mater.* **2014,** 13, (3), 294-301.
20. Jae, J.; Zheng, W. Q.; Lobo, R. F.; Vlachos, D. G., Production of Dimethylfuran from Hydroxymethylfurfural through Catalytic Transfer Hydrogenation with Ruthenium Supported on Carbon. *ChemSusChem* **2013,** 6, (7), 1158-1162.
21. Chang, C. C.; Cho, H. J.; Yu, J. Y.; Gorte, R. J.; Gulbinski, J.; Dauenhauer, P.; Fan, W., Lewis acid zeolites for tandem Diels-Alder cycloaddition and dehydration of biomass-derived dimethylfuran and ethylene to renewable p-xylene. *Green Chem.* **2016,** 18, (5), 1368-1376.
22. Chang, C. C.; Green, S. K.; Williams, C. L.; Dauenhauer, P. J.; Fan, W., Ultra-selective cycloaddition of dimethylfuran for renewable p-xylene with H-BEA. *Green Chem.* **2014,** 16, (2), 585-588.
23. Do, P. T. M.; McAtee, J. R.; Watson, D. A.; Lobo, R. F., Elucidation of Diels-Alder Reaction Network of 2,5-Dimethylfuran and Ethylene on HY Zeolite Catalyst. *ACS Catal.* **2013,** 3, (1), 41-46.
24. Perez-Ramirez, J.; Christensen, C. H.; Egeblad, K.; Christensen, C. H.; Groen, J. C., Hierarchical zeolites: enhanced utilisation of microporous crystals in catalysis by advances in materials design. *Chem. Soc. Rev.* **2008,** 37, (11), 2530-2542.
25. Egeblad, K.; Christensen, C. H.; Kustova, M.; Christensen, C. H., Templating mesoporous zeolites. *Chem. Mater.* **2008,** 20, (3), 946-960.
26. Na, K.; Jo, C.; Kim, J.; Cho, K.; Jung, J.; Seo, Y.; Messinger, R. J.; Chmelka, B. F.; Ryoo, R., Directing Zeolite Structures into Hierarchically Nanoporous Architectures. *Science* **2011,** 333, (6040), 328-332.
27. Zhang, X. Y.; Liu, D. X.; Xu, D. D.; Asahina, S.; Cychosz, K. A.; Agrawal, K. V.; Al Wahedi, Y.; Bhan, A.; Al Hashimi, S.; Terasaki, O.; Thommes, M.; Tsapatsis, M., Synthesis of Self-Pillared Zeolite Nanosheets by Repetitive Branching. *Science* **2012,** 336, (6089), 1684-1687.
28. Choi, M.; Na, K.; Kim, J.; Sakamoto, Y.; Terasaki, O.; Ryoo, R., Stable single-unit-cell nanosheets of zeolite MFI as active and long-lived catalysts. *Nature* **2009,** 461, (7261), 246-U120.
29. Fan, W.; Snyder, M. A.; Kumar, S.; Lee, P. S.; Yoo, W. C.; McCormick, A. V.; Penn, R. L.; Stein, A.; Tsapatsis, M., Hierarchical nanofabrication of microporous crystals with ordered mesoporosity. *Nat. Mater.* **2008,** 7, (12), 984-991.
30. Tao, Y. S.; Kanoh, H.; Abrams, L.; Kaneko, K., Mesopore-modified zeolites: Preparation, characterization, and applications. *Chemical Reviews* **2006,** 106, (3), 896-910.

31. Tao, Y. S.; Kanoh, H.; Hanzawa, Y.; Kaneko, K., Template synthesis and characterization of mesoporous zeolites. *Colloids and Surfaces a-Physicochemical and Engineering Aspects* **2004,** 241, (1-3), 75-80.
32. Corma, A.; Fornes, V.; Pergher, S. B.; Maesen, T. L. M.; Buglass, J. G., Delaminated zeolite precursors as selective acidic catalysts. *Nature* **1998,** 396, (6709), 353-356.
33. Groen, J. C.; Zhu, W. D.; Brouwer, S.; Huynink, S. J.; Kapteijn, F.; Moulijn, J. A.; Perez-Ramirez, J., Direct demonstration of enhanced diffusion in mesoporous ZSM-5 zeolite obtained via controlled desilication. *J. Am. Chem. Soc.* **2007,** 129, (2), 355-360.
34. Chen, H. Y.; Wydra, J.; Zhang, X. Y.; Lee, P. S.; Wang, Z. P.; Fan, W.; Tsapatsis, M., Hydrothermal Synthesis of Zeolites with Three-Dimensionally Ordered Mesoporous-Imprinted Structure. *J. Am. Chem. Soc.* **2011,** 133, (32), 12390-12393.
35. Wang, Z. P.; Dornath, P.; Chang, C. C.; Chen, H. Y.; Fan, W., Confined synthesis of three-dimensionally ordered mesoporous-imprinted zeolites with tunable morphology and Si/Al ratio. *Micropor. Mesopor. Mat.* **2013,** 181, 8-16.
36. Teixeira, A. R.; Chang, C. C.; Coogan, T.; Kendall, R.; Fan, W.; Dauenhauer, P. J., Dominance of Surface Barriers in Molecular Transport through Silicalite-1. *J. Phys. Chem. C* **2013,** 117, (48), 25545-25555.
37. Chang, C. C.; Teixeira, A. R.; Li, C.; Dauenhauer, P. J.; Fan, W., Enhanced Molecular Transport in Hierarchical Silicalite-1. *Langmuir* **2013,** 29, (45), 13943-13950.
38. Choudhary, V.; Pinar, A. B.; Sandler, S. I.; Vlachos, D. G.; Lobo, R. F., Xylose Isomerization to Xylulose and its Dehydration to Furfural in Aqueous Media. *ACS Catal.* **2011,** 1, (12), 1724-1728.
39. Moliner, M.; Roman-Leshkov, Y.; Davis, M. E., Tin-containing zeolites are highly active catalysts for the isomerization of glucose in water. *P. Natl. Acad. Sci. USA* **2010,** 107, (14), 6164-6168.
40. Roman-Leshkov, Y.; Moliner, M.; Labinger, J. A.; Davis, M. E., Mechanism of Glucose Isomerization Using a Solid Lewis Acid Catalyst in Water. *Angew. Chem. Int. Ed.* **2010,** 49, (47), 8954-8957.
41. Corma, A.; Domine, M. E.; Nemeth, L.; Valencia, S., Al-free Sn-beta zeolite as a catalyst for the selective reduction of carbonyl compounds (Meerwein-Ponndorf-Verley reaction). *J. Am. Chem. Soc.* **2002,** 124, (13), 3194-3195.
42. Boronat, M.; Corma, A.; Renz, M., Mechanism of the Meerwein-Ponndorf-Verley-Oppenauer (MPVO) redox equilibrium on Sn- and Zr-beta zeolite catalysts. *J. Phys. Chem. B* **2006,** 110, (42), 21168-21174.
43. Boronat, M.; Corma, A.; Renz, M.; Viruela, P. M., Predicting the activity of single isolated Lewis acid sites in solid catalysts. *Chem-Eur. J.* **2006,** 12, (27), 7067-7077.
44. Corma, A.; Nemeth, L. T.; Renz, M.; Valencia, S., Sn-zeolite beta as a heterogeneous chemoselective catalyst for Baeyer-Villiger oxidations. *Nature* **2001,** 412, (6845), 423-425.
45. Boronat, M.; Concepcion, P.; Corma, A.; Renz, M.; Valencia, S., Determination of the catalytically active oxidation Lewis acid sites in Sn-beta zeolites, and their optimisation by the combination of theoretical and experimental studies. *J. Catal.* **2005,** 234, (1), 111-118.

46. Boronat, M.; Concepcion, P.; Corma, A.; Navarro, M. T.; Renz, M.; Valencia, S., Reactivity in the confined spaces of zeolites: the interplay between spectroscopy and theory to develop structure-activity relationships for catalysis. *Phys. Chem. Chem. Phys.* **2009,** 11, (16), 2876-2884.
47. Patet, R. E.; Nikbin, N.; Williams, C. L.; Green, S. K.; Chang, C. C.; Fan, W.; Caratzoulas, S.; Dauenhauer, P. J.; Vlachos, D. G., Kinetic Regime Change in the Tandem Dehydrative Aromatization of Furan Diels-Alder Products. *ACS Catal.* **2015,** 5, (4), 2367-2375.
48. Taarning, E.; Saravanamurugan, S.; Holm, M. S.; Xiong, J. M.; West, R. M.; Christensen, C. H., Zeolite-Catalyzed Isomerization of Triose Sugars. *Chemsuschem* **2009,** 2, (7), 625-627.
49. Holm, M. S.; Taarning, E.; Egeblad, K.; Christensen, C. H., Catalysis with hierarchical zeolites. *Catal. Today* **2011,** 168, (1), 3-16.
50. Lew, C. M.; Rajabbeigi, N.; Tsapatsis, M., Tin-containing zeolite for the isomerization of cellulosic sugars. *Micropor. Mesopor. Mat.* **2012,** 153, 55-58.
51. Osmundsen, C. M.; Holm, M. S.; Dahl, S.; Taarning, E., Tin-containing silicates: structure-activity relations. *P. Roy. Soc. a-Math. Phy.* **2012,** 468, (2143), 2000-2016.
52. Li, L.; Stroobants, C.; Lin, K. F.; Jacobs, P. A.; Sels, B. F.; Pescarmona, P. P., Selective conversion of trioses to lactates over Lewis acid heterogeneous catalysts. *Green Chem.* **2011,** 13, (5), 1175-1181.
53. Davis, T. M.; Snyder, M. A.; Krohn, J. E.; Tsapatsis, M., Nanoparticles in lysine-silica sols. *Chem. Mater.* **2006,** 18, (25), 5814-5816.
54. Yokoi, T.; Sakamoto, Y.; Terasaki, O.; Kubota, Y.; Okubo, T.; Tatsumi, T., Periodic arrangement of silica nanospheres assisted by amino acids. *J. Am. Chem. Soc.* **2006,** 128, (42), 13664-13665.
55. Mal, N. K.; Ramaswamy, V.; Rajamohanan, P. R.; Ramaswamy, A. V., Sn-MFI molecular sieves: synthesis methods, Si-29 liquid and solid MAS-NMR, Sn-119 static and MAS NMR studies. *Micropor. Mater.* **1997,** 12, (4-6), 331-340.
56. Cho, H. J.; Dornath, P.; Fan, W., Synthesis of Hierarchical Sn-MFI as Lewis Acid Catalysts for Isomerization of Cellulosic Sugars. *ACS Catal.* **2014,** 4, (6), 2029-2037.
57. Roy, S.; Bakhmutsky, K.; Mahmoud, E.; Lobo, R. F.; Gorte, R. J., Probing Lewis Acid Sites in Sn-Beta Zeolite. *ACS Catal.* **2013,** 3, (4), 573-580.
58. West, R. M.; Holm, M. S.; Saravanamurugan, S.; Xiong, J. M.; Beversdorf, Z.; Taarning, E.; Christensen, C. H., Zeolite H-USY for the production of lactic acid and methyl lactate from C-3-sugars. *J. Catal.* **2010,** 269, (1), 122-130.
59. Chang, C. C.; Wang, Z. P.; Dornath, P.; Cho, H. J.; Fan, W., Rapid synthesis of Sn-Beta for the isomerization of cellulosic sugars. *RSC Adv.* **2012,** 2, (28), 10475-10477.
60. Vargas, N. G.; Stevenson, S.; Shantz, D. F., Synthesis and characterization of tin(IV) MFI: Sodium inhibits the synthesis of phase pure materials. *Micropor. Mesopor. Mat.* **2012,** 152, 37-49.

61. de Clippel, F.; Dusselier, M.; Van Rompaey, R.; Vanelderen, P.; Dijkmans, J.; Makshina, E.; Giebeler, L.; Oswald, S.; Baron, G. V.; Denayer, J. F. M.; Pescarmona, P. P.; Jacobs, P. A.; Sels, B. F., Fast and Selective Sugar Conversion to Alkyl Lactate and Lactic Acid with Bifunctional Carbon-Silica Catalysts. *Journal of the American Chemical Society* **2012,** 134, (24), 10089-10101.
62. Roman-Leshkov, Y.; Moliner, M.; Labinger, J. A.; Davis, M. E., Mechanism of Glucose Isomerization Using a Solid Lewis Acid Catalyst in Water. *Angewandte Chemie-International Edition* **2010,** 49, (47), 8954-8957.
63. Mal, N. K.; Ramaswamy, A. V., Hydroxylation of phenol over Sn-silicalite-1 molecular sieve: Solvent effects. *J. Mol. Catal. a-Chem.* **1996,** 105, (3), 149-158.
64. Niphadkar, P. S.; Patil, K. R.; Joshi, P. N., Characterization of surface acid sites in tin-silicalite-1 (Sn-MFI) molecular sieve by X-ray photoelectron spectroscopy. *Micropor. Mesopor. Mat.* **2011,** 141, (1-3), 236-240.
65. Roman-Leshkov, Y.; Davis, M. E., Activation of Carbonyl-Containing Molecules with Solid Lewis Acids in Aqueous Media. *ACS Catal.* **2011,** 1, (11), 1566-1580.
66. Pescarmona, P. P.; Janssen, K. P. F.; Delaet, C.; Stroobants, C.; Houthoofd, K.; Philippaerts, A.; De Jonghe, C.; Paul, J. S.; Jacobs, P. A.; Sels, B. F., Zeolite-catalysed conversion of C-3 sugars to alkyl lactates. *Green Chem.* **2010,** 12, (6), 1083-1089.
67. Bordiga, S.; Roggero, I.; Ugliengo, P.; Zecchina, A.; Bolis, V.; Artioli, G.; Buzzoni, R.; Marra, G.; Rivetti, F.; Spano, G.; Lamberti, C., Characterisation of defective silicalites. *J. Chem. Soc. Dalton Trans.* **2000**, (21), 3921-3929.
68. Corma, A.; Rey, F.; Rius, J.; Sabater, M. J.; Valencia, S., Supramolecular self-assembled molecules as organic directing agent for synthesis of zeolites. *Nature* **2004,** 431, (7006), 287-290.
69. Trzpit, M.; Soulard, M.; Patarin, J.; Desbiens, N.; Cailliez, F.; Boutin, A.; Demachy, I.; Fuchs, A. H., The effect of local defects on water adsorption in silicalite-1 zeolite: A joint experimental and molecular simulation study. *Langmuir* **2007,** 23, (20), 10131-10139.
70. Barbera, K.; Bonino, F.; Bordiga, S.; Janssens, T. V. W.; Beato, P., Structure-deactivation relationship for ZSM-5 catalysts governed by framework defects. *J. Catal.* **2011,** 280, (2), 196-205.
71. Trombetta, M.; Alejandre, A. G.; Solis, J. R.; Busca, G., An FT-IR study of the reactivity of hydrocarbons on the acid sites of HZSM5 zeolite. *Appl. Catal. A* **2000,** 198, (1-2), 81-93.
72. Jae, J.; Tompsett, G. A.; Foster, A. J.; Hammond, K. D.; Auerbach, S. M.; Lobo, R. F.; Huber, G. W., Investigation into the shape selectivity of zeolite catalysts for biomass conversion. *J. Catal.* **2011,** 279, (2), 257-268.
73. Yu, M.; Wyss, J. C.; Noble, R. D.; Falconer, J. L., 2,2-Dimethylbutane adsorption and diffusion in MFI zeolite. *Micropor. Mesopor. Mat.* **2008,** 111, (1-3), 24-31.
74. Li, S. G.; Tuan, V. A.; Falconer, J. L.; Noble, R. D., Separation of 1,3-propanediol from glycerol and glucose using a ZSM-5 zeolite membrane. *J. Membrane Sci.* **2001,** 191, (1-2), 53-59.

75. Sjoman, E.; Manttari, M.; Nystrom, M.; Koivikko, H.; Heikkila, H., Separation of xylose from glucose by nanofiltration from concentrated monosaccharide solutions. *J. Membrane Sci.* **2007,** 292, (1-2), 106-115.
76. Bouchoux, A.; Roux-de Balmann, H.; Lutin, F., Nanofiltration of glucose and sodium lactate solutions - Variations of retention between single- and mixed-solute solutions. *J. Membrane Sci.* **2005,** 258, (1-2), 123-132.
77. Shetti, V. N.; Kim, J.; Srivastava, R.; Choi, M.; Ryoo, R., Assessment of the mesopore wall catalytic activities of MFI zeolite with mesoporous/microporous hierarchical structures. *Journal of Catalysis* **2008,** 254, (2), 296-303.
78. Srivastava, R.; Choi, M.; Ryoo, R., Mesoporous materials with zeolite framework: remarkable effect of the hierarchical structure for retardation of catalyst deactivation. *Chem. Commun.* **2006**, (43), 4489-4491.
79. Li, L.; Stroobants, C.; Lin, K. F.; Jacobs, P. A.; Sels, B. F.; Pescarmona, P. P., Selective conversion of trioses to lactates over Lewis acid heterogeneous catalysts. *Green Chemistry* **2011,** 13, (5), 1175-1181.
80. Fukuda, H.; Kondo, A.; Noda, H., Biodiesel fuel production by transesterification of oils. *Journal of Bioscience and Bioengineering* **2001,** 92, (5), 405-416.
81. Palkovits, R.; Tajvidi, K.; Procelewska, J.; Rinaldi, R.; Ruppert, A., Hydrogenolysis of cellulose combining mineral acids and hydrogenation catalysts. *Green Chem.* **2010,** 12, (6), 972-978.
82. Tsukahara, K.; Sawayama, S., Liquid fuel production using microalgae. *J. Jpn. Petrol. Inst.* **2005,** 48, (5), 251-259.
83. Pagliaro, M.; Ciriminna, R.; Kimura, H.; Rossi, M.; Della Pina, C., From glycerol to value-added products. *Angew. Chem. Int. Ed.* **2007,** 46, (24), 4434-4440.
84. Katryniok, B.; Kimura, H.; Skrzynska, E.; Girardon, J. S.; Fongarland, P.; Capron, M.; Ducoulombier, R.; Mimura, N.; Paul, S.; Dumeignil, F., Selective catalytic oxidation of glycerol: perspectives for high value chemicals. *Green Chem.* **2011,** 13, (8), 1960-1979.
85. Bozell, J. J.; Petersen, G. R., Technology development for the production of biobased products from biorefinery carbohydrates-the US Department of Energy's "Top 10" revisited. *Green Chem.* **2010,** 12, (4), 539-554.
86. Garlotta, D., A literature review of poly(lactic acid). *J. Polym. Environ.* **2001,** 9, (2), 63-84.
87. Fukushima, K.; Kimura, Y., Stereocomplexed polylactides (Neo-PLA) as high-performance bio-based polymers: their formation, properties, and application. *Polym. Int.* **2006,** 55, (6), 626-642.
88. Dusselier, M.; Van Wouwe, P.; Dewaele, A.; Makshina, E.; Sels, B. F., Lactic acid as a platform chemical in the biobased economy: the role of chemocatalysis. *Energ. Environ. Sci.* **2013,** 6, (5), 1415-1442.
89. Mäki-Arvela, P.; Simakova, I. L.; Salmi, T.; Murzin, D. Y., Production of Lactic Acid/Lactates from Biomass and Their Catalytic Transformations to Commodities. *Chem. Rev.* **2013,** 114, (3), 1909-1971.

90. Kishida, H.; Jin, F. M.; Zhou, Z. Y.; Moriya, T.; Enomoto, H., Conversion of glycerin into lactic acid by alkaline hydrothermal reaction. *Chem. Lett.* **2005,** 34, (11), 1560-1561.
91. Maris, E. P.; Davis, R. J., Hydrogenolysis of glycerol over carbon-supported Ru and Pt catalysts. *J. Catal.* **2007,** 249, (2), 328-337.
92. Maris, E. P.; Ketchie, W. C.; Murayama, M.; Davis, R. J., Glycerol hydrogenolysis on carbon-supported PtRu and AuRu bimetallic catalysts. *J. Catal.* **2007,** 251, (2), 281-294.
93. Shen, Y. H.; Zhang, S. H.; Li, H. J.; Ren, Y.; Liu, H. C., Efficient Synthesis of Lactic Acid by Aerobic Oxidation of Glycerol on Au-Pt/TiO2 Catalysts. *Chem.-Eur. J.* **2010,** 16, (25), 7368-7371.
94. Lakshmanan, P.; Upare, P. P.; Le, N.-T.; Hwang, Y. K.; Hwang, D. W.; Lee, U. H.; Kim, H. R.; Chang, J.-S., Facile synthesis of CeO2-supported gold nanoparticle catalysts for selective oxidation of glycerol into lactic acid. *Appl. Catal. A* **2013,** 468, (0), 260-268.
95. Purushothaman, R. K. P.; van Haveren, J.; van Es, D. S.; Melian-Cabrera, I.; Meeldijk, J. D.; Heeres, H. J., An efficient one pot conversion of glycerol to lactic acid using bimetallic gold-platinum catalysts on a nanocrystalline CeO2 support. *Appl. Catal. B* **2014,** 147, 92-100.
96. Zope, B. N.; Hibbitts, D. D.; Neurock, M.; Davis, R. J., Reactivity of the Gold/Water Interface During Selective Oxidation Catalysis. *Science* **2010,** 330, (6000), 74-78.
97. Liang, D.; Gao, J.; Sun, H.; Chen, P.; Hou, Z.; Zheng, X., Selective oxidation of glycerol with oxygen in a base-free aqueous solution over MWNTs supported Pt catalysts. *Appl. Catal. B* **2011,** 106, (3–4), 423-432.
98. Xu, J. L.; Zhang, H. Y.; Zhao, Y. F.; Yu, B.; Chen, S.; Li, Y. B.; Hao, L. D.; Liu, Z. M., Selective oxidation of glycerol to lactic acid under acidic conditions using AuPd/TiO2 catalyst. *Green Chem.* **2013,** 15, (6), 1520-1525.
99. Mal, N. K.; Ramaswamy, V.; Rajamohanan, P. R.; Ramaswamy, A. V., Sn-MFI molecular sieves: synthesis methods, Si-29 liquid and solid MAS-NMR, Sn-119 static and MAS NMR studies. *Microporous Materials* **1997,** 12, (4-6), 331-340.
100. Watanabe, R.; Yokoi, T.; Tatsumi, T., Synthesis and application of colloidal nanocrystals of the MFI-type zeolites. *J. Colloid Interf. Sci.* **2011,** 356, (2), 434-441.
101. Chang, C. C.; Wang, Z. P.; Dornath, P.; Cho, H. J.; Fan, W., Rapid synthesis of Sn-Beta for the isomerization of cellulosic sugars. *Rsc Advances* **2012,** 2, (28), 10475-10477.
102. Cho, H. J.; Chang, C. C.; Fan, W., Base free, one-pot synthesis of lactic acid from glycerol using a bifunctional Pt/Sn-MFI catalyst. *Green Chemistry* **2014,** 16, (7), 3428-3433.
103. Punyawudho, K.; Blom, D. A.; Van Zee, J. W.; Monnier, J. R., Comparison of different methods for determination of Pt surface site concentrations for supported Pt electrocatalysts. *Electrochim. Acta* **2010,** 55, (19), 5349-5356.
104. Tongsakul, D.; Nishimura, S.; Ebitani, K., Platinum/Gold Alloy Nanoparticles-Supported Hydrotalcite Catalyst for Selective Aerobic Oxidation of Polyols in Base-Free Aqueous Solution at Room Temperature. *ACS Catal.* **2013,** 3, (10), 2199-2207.

105. Rodrigues, E. G.; Delgado, J. J.; Chen, X.; Pereira, M. F. R.; Orfao, J. J. M., Selective Oxidation of Glycerol Catalyzed by Gold Supported on Multiwalled Carbon Nanotubes with Different Surface Chemistries. *Ind. Eng. Chem. Res.* **2012,** 51, (49), 15884-15894.
106. Gounder, R.; Davis, M. E., Beyond shape selective catalysis with zeolites: Hydrophobic void spaces in zeolites enable catalysis in liquid water. *AIChE J.* **2013,** 59, (9), 3349-3358.
107. Bermejo-Deval, R.; Assary, R. S.; Nikolla, E.; Moliner, M.; Roman-Leshkov, Y.; Hwang, S. J.; Palsdottir, A.; Silverman, D.; Lobo, R. F.; Curtiss, L. A.; Davis, M. E., Metalloenzyme-like catalyzed isomerizations of sugars by Lewis acid zeolites. *P. Natl. Acad. Sci. USA* **2012,** 109, (25), 9727-9732.
108. Concepcion, P.; Perez, Y.; Hernandez-Garrido, J. C.; Fajardo, M.; Calvino, J. J.; Corma, A., The promotional effect of Sn-beta zeolites on platinum for the selective hydrogenation of alpha,beta-unsaturated aldehydes. *Phys. Chem. Chem. Phys.* **2013,** 15, (29), 12048-12055.
109. Assary, R. S.; Curtiss, L. A., Theoretical Study of 1,2-Hydride Shift Associated with the Isomerization of Glyceraldehyde to Dihydroxy Acetone by Lewis Acid Active Site Models. *J. Phys. Chem. A* **2011,** 115, (31), 8754-8760.
110. Rasrendra, C. B.; Fachri, B. A.; Makertihartha, I. G. B. N.; Adisasmito, S.; Heeres, H. J., Catalytic Conversion of Dihydroxyacetone to Lactic Acid Using Metal Salts in Water. *Chemsuschem* **2011,** 4, (6), 768-777.
111. Martra, G., Lewis acid and base sites at the surface of microcrystalline TiO2 anatase: relationships between surface morphology and chemical behaviour. *Appl. Catal. A* **2000,** 200, (1-2), 275-285.
112. de Clippel, F.; Dusselier, M.; Van Rompaey, R.; Vanelderen, P.; Dijkmans, J.; Makshina, E.; Giebeler, L.; Oswald, S.; Baron, G. V.; Denayer, J. F. M.; Pescarmona, P. P.; Jacobs, P. A.; Sels, B. F., Fast and Selective Sugar Conversion to Alkyl Lactate and Lactic Acid with Bifunctional Carbon-Silica Catalysts. *J. Am. Chem. Soc.* **2012,** 134, (24), 10089-10101.
113. Shen, Y. H.; Zhang, S. H.; Li, H. J.; Ren, Y.; Liu, H. C., Efficient Synthesis of Lactic Acid by Aerobic Oxidation of Glycerol on Au-Pt/TiO2 Catalysts. *Chemistry-a European Journal* **2010,** 16, (25), 7368-7371.
114. Tang, B.; Dai, W. L.; Wu, G. J.; Guan, N. J.; Li, L. D.; Hunger, M., Improved Postsynthesis Strategy to Sn-Beta Zeolites as Lewis Acid Catalysts for the Ring-Opening Hydration of Epoxides. *ACS Catal.* **2014,** 4, (8), 2801-2810.
115. Pacheco, J. J.; Davis, M. E., Synthesis of terephthalic acid via Diels-Alder reactions with ethylene and oxidized variants of 5-hydroxymethylfurfural. *Proc. Natl. Acad. Sci. U.S.A.* **2014,** 111, (23), 8363-8367.
116. Pacheco, J. J.; Labinger, J. A.; Sessions, A. L.; Davis, M. E., Route to Renewable PET: Reaction Pathways and Energetics of Diels-Alder and Dehydrative Aromatization Reactions Between Ethylene and Biomass-Derived Furans Catalyzed by Lewis Acid Molecular Sieves. *ACS Catal.* **2015,** 5, (10), 5904-5913.

117. Williams, C. L.; Chang, C. C.; Do, P.; Nikbin, N.; Caratzoulas, S.; Vlachos, D. G.; Lobo, R. F.; Fan, W.; Dauenhauer, P. J., Cycloaddition of Biomass-Derived Furans for Catalytic Production of Renewable p-Xylene. *ACS Catal.* **2012,** 2, (6), 935-939.
118. Yu, J.; Zhu, S.; Dauenhauer, P. J.; Cho, H. J.; Fan, W.; Gorte, R. J., Adsorption and reaction properties of SnBEA, ZrBEA and H-BEA for the formation of p-xylene from DMF and ethylene. *Catal. Sci. & Tech.* **2016,** 6, (14), 5729-5736.
119. Cho, H. J.; Ren, L.; Vattipalli, V.; Yeo, Y.-H.; Gould, N.; Xu, B.; Gorte, R. J.; Lobo, R.; Dauenhauer, P. J.; Tsapatsis, M.; Fan, W., Renewable p-Xylene from 2,5-Dimethylfuran and Ethylene Using Phosphorus-containing Zeolite Catalysts. *Chemcatchem* **2016**.
120. Cho, H. J.; Chang, C. C.; Fan, W., Base free, one-pot synthesis of lactic acid from glycerol using a bifunctional Pt/Sn-MFI catalyst. *Green Chem.* **2014,** 16, (7), 3428-3433.
121. Cho, H. J.; Dornath, P.; Fan, W., Synthesis of Hierarchical Sn-MFI as Lewis Acid Catalysts for Isomerization of Cellulosic Sugars. *Acs Catalysis* **2014,** 4, (6), 2029-2037.
122. Rajabbeigi, N.; Torres, A. I.; Lew, C. M.; Elyassi, B.; Ren, L. M.; Wang, Z. P.; Cho, H. J.; Fan, W.; Daoutidis, P.; Tsapatsis, M., On the kinetics of the isomerization of glucose to fructose using Sn-Beta. *Chem. Eng. Sci.* **2014,** 116, 235-242.
123. Cundy, C. S.; Cox, P. A., The hydrothermal synthesis of zeolites: Precursors, intermediates and reaction mechanism. *Micropor. Mesopor. Mat.* **2005,** 82, (1-2), 1-78.
124. Tolborg, S.; Katerinopoulou, A.; Falcone, D. D.; Sadaba, I.; Osmundsen, C. M.; Davis, R. J.; Taarning, E.; Fristrup, P.; Holm, M. S., Incorporation of tin affects crystallization, morphology, and crystal composition of Sn-Beta. *J. Mater. Chem. A* **2014,** 2, (47), 20252-20262.
125. Chang, C. C.; Cho, H. J.; Wang, Z. P.; Wang, X. T.; Fan, W., Fluoride-free synthesis of a Sn-BEA catalyst by dry gel conversion. *Green Chem.* **2015,** 17, (5), 2943-2951.
126. Dijkmans, J.; Demol, J.; Houthoofd, K.; Huang, S. G.; Pontikes, Y.; Sels, B., Post-synthesis Sn beta: An exploration of synthesis parameters and catalysis. *J. Catal.* **2015,** 330, 545-557.
127. Hammond, C.; Conrad, S.; Hermans, I., Simple and Scalable Preparation of Highly Active Lewis Acidic Sn-beta. *Angew. Chem. Int. Ed.* **2012,** 51, (47), 11736-11739.
128. Hammond, C.; Padovan, D.; Al-Nayili, A.; Wells, P. P.; Gibson, E. K.; Dimitratos, N., Identification of Active and Spectator Sn Sites in Sn-beta Following Solid-State Stannation, and Consequences for Lewis Acid Catalysis. *Chemcatchem* **2015,** 7, (20), 3322-3331.
129. Li, P.; Liu, G. Q.; Wu, H. H.; Liu, Y. M.; Jiang, J. G.; Wu, P., Postsynthesis and Selective Oxidation Properties of Nanosized Sn-Beta Zeolite. *J. Phys. Chem. C* **2011,** 115, (9), 3663-3670.
130. Dijkmans, J.; Dusselier, M.; Janssens, W.; Trekels, M.; Vantomme, A.; Breynaert, E.; Kirschhock, C.; Sels, B. F., An Inner-/Outer-Sphere Stabilized Sn Active Site in beta-Zeolite: Spectroscopic Evidence and Kinetic Consequences. *ACS Catal.* **2016,** 6, (1), 31-46.

131. Dijkmans, J.; Gabriels, D.; Dusselier, M.; de Clippel, F.; Vanelderen, P.; Houthoofd, K.; Malfliet, A.; Pontikes, Y.; Sels, B. F., Productive sugar isomerization with highly active Sn in dealuminated beta zeolites. *Green Chem.* **2013,** 15, (10), 2777-2785.
132. Gounder, R.; Davis, M. E., Monosaccharide and disaccharide isomerization over Lewis acid sites in hydrophobic and hydrophilic molecular sieves. *J. Catal.* **2013,** 308, 176-188.
133. Qiao, Y. Y.; Yang, M.; Gao, B. B.; Wang, L. Y.; Tian, P.; Xu, S. T.; Liu, Z. M., Creation of hollow SAPO-34 single crystals via alkaline or acid etching. *Chem. Commun.* **2016,** 52, (33), 5718-5721.
134. Dai, C. Y.; Zhang, A. F.; Li, L. L.; Hou, K. K.; Ding, F. S.; Li, J.; Mu, D. Y.; Song, C. S.; Liu, M.; Guo, X. W., Synthesis of Hollow Nanocubes and Macroporous Monoliths of Silicalite-1 by Alkaline Treatment. *Chem. Mater.* **2013,** 25, (21), 4197-4205.
135. Li, S. W.; Tuel, A.; Laprune, D.; Meunier, F.; Farrusseng, D., Transition-Metal Nanoparticles in Hollow Zeolite Single Crystals as Bifunctional and Size-Selective Hydrogenation Catalysts. *Chem. Mater.* **2015,** 27, (1), 276-282.
136. Wang, Y. R.; Lin, M.; Tuel, A., Hollow TS-1 crystals formed via a dissolution-recrystallization process. *Micropor. Mesopor. Mat.* **2007,** 102, (1-3), 80-85.
137. Wang, Y. R.; Tuel, A., Nanoporous zeolite single crystals: ZSM-5 nanoboxes with uniform intracrystalline hollow structures. *Micropor. Mesopor. Mat.* **2008,** 113, (1-3), 286-295.
138. Dai, C. Y.; Zhang, A. F.; Liu, M.; Guo, X. W.; Song, C. S., Hollow ZSM-5 with Silicon-Rich Surface, Double Shells, and Functionalized Interior with Metallic Nanoparticles and Carbon Nanotubes. *Adv. Funct. Mater.* **2015,** 25, (48), 7479-7487.
139. Verboekend, D.; Milina, M.; Mitchell, S.; Perez-Ramirez, J., Hierarchical Zeolites by Desilication: Occurrence and Catalytic Impact of Recrystallization and Restructuring. *Cryst. Growth Des.* **2013,** 13, (11), 5025-5035.
140. Yoo, W. C.; Zhang, X. Y.; Tsapatsis, M.; Stein, A., Synthesis of mesoporous ZSM-5 zeolites through desilication and re-assembly processes. *Micropor. Mesopor. Mat.* **2012,** 149, (1), 147-157.
141. Gamliel, D. P.; Cho, H. J.; Fan, W.; Valla, J. A., On the effectiveness of tailored mesoporous MFI zeolites for biomass catalytic fast pyrolysis. *Appl. Catal. A* **2016,** 522, 109-119.
142. Abello, S.; Bonilla, A.; Perez-Ramirez, J., Mesoporous ZSM-5 zeolite catalysts prepared by desilication with organic hydroxides and comparison with NaOH leaching. *Appl. Catal. A* **2009,** 364, (1-2), 191-198.
143. Ivanova, I. I.; Knyazeva, E. E., Micro-mesoporous materials obtained by zeolite recrystallization: synthesis, characterization and catalytic applications. *Chem. Soc. Rev.* **2013,** 42, (9), 3671-3688.
144. Mintova, S.; Valtchev, V.; Onfroy, T.; Marichal, C.; Knozinger, H.; Bein, T., Variation of the Si/Al ratio in nanosized zeolite Beta crystals. *Micropor. Mesopor. Mat.* **2006,** 90, (1-3), 237-245.

145. Harris, J. W.; Cordon, M. J.; Di Iorio, J. R.; Vega-Vila, J. C.; Ribeiro, F. H.; Gounder, R., Titration and quantification of open and closed Lewis acid sites in Sn-Beta zeolites that catalyze glucose isomerization. *J. Catal.* **2016,** 335, 141-154.
146. Al-Nayili, A.; Yakabi, K.; Hammond, C., Hierarchically porous BEA stannosilicates as unique catalysts for bulky ketone conversion and continuous operation. *J. Mater. Chem. A* **2016,** 4, (4), 1373-1382.
147. Boronat, M.; Corma, A.; Renz, M.; Sastre, G.; Viruela, P. M., A multisite molecular mechanism for Baeyer-Villiger oxidations on solid catalysts using environmentally friendly H2O2 as oxidant. *Chem-Eur. J.* **2005,** 11, (23), 6905-6915.
148. Bermejo-Deval, R.; Gounder, R.; Davis, M. E., Framework and Extraframework Tin Sites in Zeolite Beta React Glucose Differently. *ACS Catal.* **2012,** 2, (12), 2705-2713.
149. Bermejo-Deval, R.; Orazov, M.; Gounder, R.; Hwang, S. J.; Davis, M. E., Active Sites in Sn-Beta for Glucose Isomerization to Fructose and Epimerization to Mannose. *ACS Catal.* **2014,** 4, (7), 2288-2297.
150. Lewis, J. D.; Van de Vyver, S.; Crisci, A. J.; Gunther, W. R.; Michaelis, V. K.; Griffin, R. G.; Roman-Leshkov, Y., A Continuous Flow Strategy for the Coupled Transfer Hydrogenation and Etherification of 5-(Hydroxymethyl)furfural using Lewis Acid Zeolites. *Chemsuschem* **2014,** 7, (8), 2255-2265.
151. Gounder, R., Hydrophobic microporous and mesoporous oxides as Bronsted and Lewis acid catalysts for biomass conversion in liquid water. *Catal. Sci. Technol.* **2014,** 4, (9), 2877-2886.
152. Ng, E. P.; Mintova, S., Nanoporous materials with enhanced hydrophilicity and high water sorption capacity. *Micropor. Mesopor. Mat.* **2008,** 114, (1-3), 1-26.
153. Zhang, K.; Lively, R. P.; Noel, J. D.; Dose, M. E.; McCool, B. A.; Chance, R. R.; Koros, W. J., Adsorption of Water and Ethanol in MFI-Type Zeolites. *Langmuir* **2012,** 28, (23), 8664-8673.
154. Courtney, T. D.; Chang, C. C.; Gorte, R. J.; Lobo, R. F.; Fan, W.; Nikolakis, V., Effect of water treatment on Sn-BEA zeolite: Origin of 960 cm(-1) FTIR peak. *Micropor. Mesopor. Mat.* **2015,** 210, 69-76.
155. Lange, K. R., Characterization of Molecular Water on Silica Surfaces. *J. Coll. Sci.* **1965,** 20, (3), 231-&.
156. Naono, H.; Fujiwara, R.; Yagi, M., Determination of Physisorbed and Chemisorbed Waters on Silica-Gel and Porous Silica Glass by Means of Desorption Isotherms of Water-Vapor. *J. Colloid Interf. Sci.* **1980,** 76, (1), 74-82.
157. Saliba, S.; Ruch, P.; Volksen, W.; Magbitang, T. P.; Dubois, G.; Michel, B., Combined influence of pore size distribution and surface hydrophilicity on the water adsorption characteristics of micro- and mesoporous silica. *Micropor. Mesopor. Mat.* **2016,** 226, 221-228.
158. Saravanamurugan, S.; Paniagua, M.; Melero, J. A.; Riisager, A., Efficient Isomerization of Glucose to Fructose over Zeolites in Consecutive Reactions in Alcohol and Aqueous Media. *J. Am. Chem. Soc.* **2013,** 135, (14), 5246-5249.
159. Akerlof, G., Dielectric constants of some organic solvent-water mixtures at various temperatures. *J. Am. Chem. Soc.* **1932,** 54, 4125-4139.

160. Sneh, O.; George, S. M., Thermal-Stability of Hydroxyl-Groups on a Well-Defined Silica Surface. *J. Phys. Chem.* **1995,** 99, (13), 4639-4647.
161. Pelmenschikov, A. G.; Morosi, G.; Gamba, A., Quantum Chemical Molecular-Models of Oxides .2. Methanol Adsorption on Silica and Zeolites. *J. Phys. Chem.* **1992,** 96, (5), 2241-2246.
162. Seki, N.; Saito, H., Lactose as a source for lactulose and other functional lactose derivatives. *Int. Dairy J.* **2012,** 22, (2), 110-115.
163. Aider, M.; de Halleux, D., Isomerization of lactose and lactulose production: review. *Trends Food Sci. Tech.* **2007,** 18, (7), 356-364.
164. Wantanachaisaeng, P.; O' Neil, K., Capturing Opportunities for Para-xylene Production. *UOP LLC* **2007**.
165. Agency, I. E., Technology Roadmap Energy and GHG Reductions in the Chemical Industry via Catalytic Processes. In 2013; pp 1-60.
166. Wang, D.; Osmundsen, C. M.; Taarning, E.; Dumesic, J. A., Selective Production of Aromatics from Alkylfurans over Solid Acid Catalysts. *ChemCatChem* **2013,** 5, (7), 2044-2050.
167. Kim, T. W.; Kim, S. Y.; Kim, J. C.; Kim, Y.; Ryoo, R.; Kim, C. U., Selective p-xylene production from biomass-derived dimethylfuran and ethylene over zeolite beta nanosponge catalysts. *Appl. Catal. B* **2016,** 185, 100-109.
168. Lyons, T. W.; Guironnet, D.; Findlater, M.; Brookhart, M., Synthesis of p-Xylene from Ethylene. *J. Am. Chem. Soc.* **2012,** 134, (38), 15708-15711.
169. Shiramizu, M.; Toste, F. D., On the Diels-Alder Approach to Solely Biomass-Derived Polyethylene Terephthalate (PET): Conversion of 2,5-Dimethylfuran and Acrolein into p-Xylene. *Chem.-Eur. J.* **2011,** 17, (44), 12452-12457.
170. Virent, Virent BioFormPX® Paraxylene Used for World's First PET Plastic Bottle Made Entirely From Plant-Based Material. *http://www.virent.com/news/virent-bioformpx-paraxylene-used-for-worlds-first-pet-plastic-bottle-made-entirely-from-plant-based-material/* **2015**.
171. Bruijnincx, P. C. A.; Weckhuysen, B. M., Shale Gas Revolution: An Opportunity for the Production of Biobased Chemicals? *Angew. Chem. Int. Ed.* **2013,** 52, (46), 11980-11987.
172. Lin, Z. J.; Nikolakis, V.; Ierapetritou, M., Alternative Approaches for p-Xylene Production from Starch: Techno-Economic Analysis. *Ind. Eng. Chem. Res.* **2014,** 53, (26), 10688-10699.
173. Kang, S. M.; Yu, J., A gasoline-grade biofuel formed from renewable polyhydroxybutyrate on solid phosphoric acid. *Fuel* **2015,** 160, 282-290.
174. Wang, R.; Wan, J. B.; Li, Y. H.; Sun, H. W., An improvement of MCM-41 supported phosphoric acid catalyst for alkylation desulfurization of fluid catalytic cracking gasoline. *Fuel* **2015,** 143, 504-511.
175. Camblor, M. A.; Corma, A.; Valencia, S., Spontaneous nucleation and growth of pure silica zeolite-beta free of connectivity defects. *Chem. Commun.* **1996**, (20), 2365-2366.

176. Emeis, C. A., Determination of Integrated Molar Extinction Coefficients for Infrared-Absorption Bands of Pyridine Adsorbed on Solid Acid Catalysts. *J. Catal.* **1993,** 141, (2), 347-354.
177. Coetzee, J. H.; Mashapa, T. N.; Prinsloo, N. M.; Rademan, J. D., An improved solid phosphoric acid catalyst for alkene oligomerization in a Fischer-Tropsch refinery. *Appl. Catal. A* **2006,** 308, 204-209.
178. Das, S. K.; Bhunia, M. K.; Chakraborty, D.; Khuda-Bukhsh, A. R.; Bhaumik, A., Hollow spherical mesoporous phosphosilicate nanoparticles as a delivery vehicle for an antibiotic drug. *Chem. Commun.* **2012,** 48, (23), 2891-2893.
179. Garcia, A.; Colilla, M.; Izquierdo-Barba, I.; Vallet-Regi, M., Incorporation of Phosphorus into Mesostructured Silicas: A Novel Approach to Reduce the SiO2 Leaching in Water. *Chem. Mater.* **2009,** 21, (18), 4135-4145.
180. Matsuda, A.; Kanzaki, T.; Kotani, Y.; Talsumisago, M.; Minami, T., Proton conductivity and structure of phosphosilicate gels derived from tetraethoxysilane and phosphoric acid or triethylphosphate. *Solid State Ionics* **2001,** 139, (1-2), 113-119.
181. Zeng, D. L.; Zhang, Q.; Chen, S. Y.; Liu, S. L.; Chen, Y.; Wang, G. H., A novel solid phosphoric acid from rice hull ash for olefinic alkylation of thiophenic sulfur in gasoline. *Mater. Res. Bull.* **2015,** 72, 276-279.
182. Gorte, R. J., What do we know about the acidity of solid acids ? *Catal. Lett.* **1999,** 62, (1), 1-13.
183. Davis, S. E.; Ide, M. S.; Davis, R. J., Selective oxidation of alcohols and aldehydes over supported metal nanoparticles. *Green Chem.* **2013,** 15, (1), 17-45.
184. Farneth, W. E.; Gorte, R. J., Methods for Characterizing Zeolite Acidity. *Chem. Rev.* **1995,** 95, (3), 615-635.